Systematic Uncertainties in Cosmic Ray Energies Measured by the Auger Fluorescence Detectors

Vanessa Catherine Holmes

Thesis submitted for the degree of

Doctor of Philosophy

The University of Adelaide

School of Chemistry and Physics

September 2011

Contents

Abstract

This work investigates the processes used to reconstruct extensive air showers induced in the atmosphere by ultra high energy cosmic rays. It contributes to the efforts of the Pierre Auger Collaboration, whose members are working to solve many mysteries behind the phenomenon of these particles. Specifically my work has focused on the use of the Pierre Auger Observatory's fluorescence detectors to determine cosmic ray energies. I have investigated ways to reduce the systematic uncertainties involved in the reconstruction process.

To accurately reconstruct an extensive air shower in order to determine properties of the primary cosmic ray, we need to be able to model how the atmosphere will affect its production and propagation. A precise knowledge of how to interpret the signals received at our detectors is also needed. Inaccurate models or incorrect assumptions may lead to large errors in the shape and magnitude of the true energy spectrum of the cosmic rays which we observe at Earth. We wish to use the information that we gather from this experiment about the energy spectrum, anisotropy and composition of cosmic rays to help locate and study sources, and the acceleration mechanisms that produce their incredible energies. If we are inaccurately reconstructing these extensive air showers then this could lead to incorrect theories being developed. The systematic uncertainties that I have investigated and are presented in my thesis are:

- An unexplained halo of light around the shower track at the fluorescence detector which led me to develop a parameterisation for singly scattered Cherenkov light that we receive at the fluorescence detectors. This parameterisation is a function of

shower evolution, distance to the shower, scattering probability and angular distance from the tracks centre.

- Uncertainty in the nitrogen fluorescence yield due to the humidity dependence of collisional quenching. To take this dependence into account I constructed monthly vapour pressure profiles using data acquired from radiosonde launches conducted above the Pierre Auger Observatory. As the fluorescence detectors are unable to detect air showers on overcast days, launches conducted in overcast conditions were identified and excluded, using infra-red cloud camera data and sky temperature measurements. Methods to reduce the uncertainty on the vapour pressure profiles uncertainties were also investigated.

- Uncertainty in the methods used to interpret the light seen by the fluorescence detectors. When comparing two methods, I found that they differed in their approach to take into account the lateral shower width at large shower ages. This was because the initial parameterisation was only constructed up to shower ages of 1.2. I used the simulation package CORSIKA to check whether the original parameterisation was still valid at ages up to 1.5, and to check its validity down to primary particle energies of 10^{17}eV.

In addressing these systematic uncertainties, we now have a better understanding of the light that we receive at the Fluorescence Detectors, and of how to collect this light for use in reconstructing extensive air showers to determine the cosmic ray energy spectrum, cosmic ray composition and their arrival directions.

Statement of Originality

I, Vanessa Catherine Holmes certify that this work contains no material which has been accepted for the award of any other degree or diploma in any university or other tertiary institution and, to the best of my knowledge and belief, contains no material previously published or written by another person, except where due reference has been made in the text. I give consent to this copy of my thesis, when deposited in the University Library, being made available for loan and photocopying, subject to thee provisions of the Copyright Act 1968. I also give permission for the digital version of my thesis to be made available on the web, via the University's digital research repository, the Library catalogue and also through web search engines, unless permission has been granted by the University to restrict access for a period of time.

Signature :

Student : Vanessa Catherine Holmes

Date : 27/09/2011

Acknowledgements

I would like to thank my Supervisors for their guidance and patience, my friends for their ongoing support, my family for their unwavering belief in my abilities, and the Pierre Auger Collaboration for giving me the chance to be a part of such an amazing experiment. But most of all, I wish to thank my husband-to-be Brad for absolutely everything.

List of Figures

List of Tables

1. Introduction

The cosmic rays that we receive at Earth, have energies ranging from 10^9 eV to 10^{20} eV. Their composition varies over this large energy range, and is made up of heavy and light nuclei, protons, electrons/positrons and photons [1]. The energy and composition of cosmic rays can be measured directly below 10^{14} eV using balloon-borne detectors. Above this energy, the flux is too low to be measured directly. Instead the properties of cosmic rays must be inferred from their particle interactions in the atmosphere. The type of detector used to observe these interactions, as well as the interpretation of these observations has a large effect on the calculated cosmic ray energy and composition. Also, at the highest end of the energy range, the flux falls to roughly 1 particle per square kilometre, per century, and therefore a large collecting area is required to acquire large enough statistics to study these, the highest energy cosmic rays. The Pierre Auger Observatory (PAO) has been specifically designed to face these two problems. It is a hybrid detector, capable of observing a given shower simultaneously using two of the main detection techniques. It consists of a ground array of water Cherenkov detectors, to measure particle densities at the ground, which is overlooked by fluorescence telescopes used to observe the energy deposited by the shower in the atmosphere. It also boasts a large collecting area of 3000 km^2 which, assuming 100% detector efficiency, should result in 30 events with $\mathrm{E} \geq 6 \times 10^{19}$ eV per year.

When high energy cosmic rays enter the atmosphere they interact and produce large particle cascades called extensive air showers (EAS). The fluorescence detectors provide a calorimetric measure of a shower's energy, and view the cascade development directly. As the reconstruction of these data is largely independent of hadronic interaction mo-

dels, it provides an energy by which to calibrate the surface detectors. There are many components to the complex procedure of collecting, interpreting and analysing the information collected by the fluorescence detectors. The work presented here attempts to better understand, and to reduce, the systematic uncertainties associated with the fluorescence technique. Measurements of the energy spectrum to high accuracy and precision are important for both composition and anisotropy studies, as well as understanding the acceleration mechanisms present in possible cosmic ray sources.

This thesis is structured as follows: Chapter 2 provides an overview of cosmic rays and Chapter 3 discusses the physics of extensive air showers as well as detection techniques. Chapter 4 outlines the Pierre Auger Observatory and the specifics of the fluorescence detectors as well as the surface array and Chapter 5 details the latest results from the Pierre Auger Collaboration. The remainder of the thesis focuses on my investigations of various systematic uncertainties associated with the fluorescence detector's interpretation of the signals that it receives from extensive air showers.

Chapter 6 looks at the effect of humidity and temperature on the fluorescence yield, and the importance of accurate vapour pressure profiles for the atmosphere above the array. I have also looked at ways of scaling the monthly vapour pressure models using weather station readings taken at the times of events. Chapter 7 investigates the light collection method at the fluorescence detectors and the calculation of Cherenkov contamination. Lastly, Chapter 8 looks at the dependence of the lateral width of extensive air showers on it's stage of evolution through the atmosphere.

2. Cosmic Rays

Cosmic rays (CR) were discovered by Victor Hess [2] in 1912 through a series of balloon flights. He found that, after an initial reduction, the ionisation in the atmosphere increased with distance above the ground, which contradicted the idea at the time that the ionisation in the atmosphere was due to radiation from the Earth's surface. Hess concluded that the source of radiation must be from above. This began the search for potential sources of this ionising radiation. It was theorised that charged particles produced outside of the Earth were responsible for ionising the atmosphere. These particles were given the name of cosmic rays. In the 1920s, trajectory analyses of cosmic rays in the Earth's magnetic field indicated particle energies of up to 20 GeV (1GeV = 10^9eV). In 1939 Pierre Auger, using an array of ground detectors, identified the first extensive air showers [3] with energies beyond 10^{15} eV. The estimates of the energy of the primary particles were made with the understanding of electromagnetic cascades at the time, and these estimates were most likely conservative. Below these energies, the cosmic rays could still be detected directly using emulsion chambers at high altitudes, but above this energy, the flux becomes too low for this to be done efficiently. So we need to study these particles by viewing the interactions which they undergo in the atmosphere, through the detection of extensive air showers. The first large array of detectors was at Volcano Ranch in New Mexico, which in 1962 was the first to measure an EAS induced by a primary cosmic ray energy of 10^{20} eV [4]. Since then there have been many experiments that have studied these EAS, either by detecting the shower particles that reach the ground, or by observing the photons from the interactions of these shower particles with the molecular atmosphere. In this chapter I will briefly discuss the energy spectrum, composition and arrival directions

of cosmic rays at the highest energies.

2.1. Energy Spectrum

The cosmic ray energy spectrum that we detect at the Earth extends over 11 decades, beginning with solar cosmic rays with energies of a few GeV, to cosmic rays of extragalactic origin with energies greater than 10^{20} eV. Over this energy range the flux decreases by 30 orders of magnitude, as illustrated in figure 2.1. It follows a power law, $E^{-\alpha}$, and the index, α, changes only slightly over the entire observed spectrum.

The energy spectrum is a single power law, with the exception of an observed downwards bend at 3×10^{15} eV and an upwards bend at 5×10^{18} eV, giving it the shape of a leg. The features are therefore aptly named the knee and the ankle respectively. These features can be interpreted as being due to a change in the source acceleration mechanisms, or as an energy dependent propagation effect.

Figure 2.2 illustrates the differential energy spectrum. The features of the spectrum are much clearer when the flux is multiplied by $E^{2.7}$. This flattens the spectrum as the slope of the flux is $\alpha = 2.7$ below the knee and above the ankle. There is still a downward slope between the knee and ankle where $\alpha = 3.1$. The knee and the ankle have been observed by many CR experiments, which used varied techniques. This ensures that they are not due to artefact's of detection. While there is now fair agreement on the features which have been observed, the same cannot be said about the causes of those features.

The knee at 3×10^{15} eV [7], marks the energy at which the spectrum becomes steeper, with the index (α) changing from 2.7 to 3.1. Below this energy it is believed that cosmic rays are of galactic origin, accelerated through diffusive shock acceleration in supernova remnants [8] (this is discussed in detail in section 2.3.1). The cosmic ray primary mass also increases with energy up to the knee, which is consistent with galactic cosmic ray accelerators reaching their maximum energy, which is larger for larger Z. Figure 2.3 shows the cosmic ray spectrum for five groups of elements. The reconstruction was performed using two different hadronic interaction models, QGSJET01 and SIBYLL2.1. It shows that the knee is located at different energies for energy spectra of various compositions.

A further steepening to $\alpha = 3.3$ has been noted at roughly $5 \times 10^{17}\,\mathrm{eV}$ and is called the second knee. Then, at the ankle at $5\,\mathrm{EeV}$ ($1\,\mathrm{EeV} = 10^{18}\,\mathrm{eV}$), the spectrum flattens back to $\alpha = 2.7$. Finally we observe a suppression of the cosmic ray flux above $6 \times 10^{19}\,\mathrm{eV}$.

Most cosmic rays are believed to be of galactic origin, with the ankle believed to be located at the energy above which the extragalactic component becomes dominant. This is interestingly the same energy at which galactic magnetic fields no longer confine galactic protons, as their gyro−radius becomes comparable to the thickness of the galactic disk. The exact energy expected for the cutoff of the galactic component is highly dependent on models of source acceleration mechanisms and galactic magnetic field models. Experimental data with high statistics at these energies is required to determine the exact energy at which the ankle occurs. Assuming that galactic cosmic rays are accelerated in supernova remnants (SNR), the maximum achievable energy is dependent on the charge of the particle (noted above and discussed in section 2.3.1). This would mean that heavy nuclei such as iron would be dominant towards the end of the galactic spectrum, with an expected cutoff energy of $5 \times 10^{16}\,\mathrm{eV}$. Now, if the interpretation of the ankle is that the extragalactic component only begins to dominate at ankle energies, then there is a section of the spectrum between the knee and the ankle which is unaccounted for.

The cosmic rays which we receive from different locations and sources will have different energy spectra, and this affects the total spectrum which we observe. The galactic component will be unaffected by the cosmic microwave background radiation (CMBR). Solar modulation can be neglected for cosmic rays above a few hundred MeV per nucleon [10], which would be about 10 GeV for iron nuclei. As the energies of interest in the Auger project are much higher than this, solar effects can be neglected. The energy spectrum of extragalactic protons should exhibit a suppression of flux at energies above $6 \times 10^{19}\,\mathrm{eV}$. This is a theoretical limit, proposed by Greisen, Zatespin and Kuzmin, known as the GZK cut-off [11, 12], above which the flux of cosmic rays should decrease sharply. Often referred to as a cut-off, it is due to the presence of the 2.7 K cosmic microwave background, which causes protons to lose energy by photo-pion production until they fall under $E_{GZK} = 6 \times 10^{19}\,\mathrm{eV}$. Past experiments such as AGASA and HiRes have low statistics of such events and claim a 30 % systematic energy uncertainty. Therefore, until recently, data on events with $\mathrm{E} > 10^{20}\,\mathrm{eV}$ were unable to demonstrate the existence or lack thereof of the GZK cut-off. The results from the two experiments are within each others

errors below E_{GZK} and are within $2\,\sigma$ of each other above [13]. The term "cut-off" may be misleading, as the presence of the GZK feature would then imply a sharp drop in the cosmic ray flux above this energy. Cosmic rays with energies above the cut-off are observed, which would imply that they originate from relatively nearby. In figure 2.4 the results from HiRes and AGASA are displayed, with HiRes observing a suppression at energies above E_{GZK}, and AGASA seeing a continuation in the spectrum. The suppression was observed with a $5\,\sigma$ significance, observing 13 events above the cut-off compared to the 43.2 events that would be expected if the spectrum continued [14]. As one project used the fluorescence technique, and the other a ground array that measured particle densities, it has been difficult to understand how their contradicting results at the highest energies occurred. An approach to this problem would be to use both methods in a complementary way.

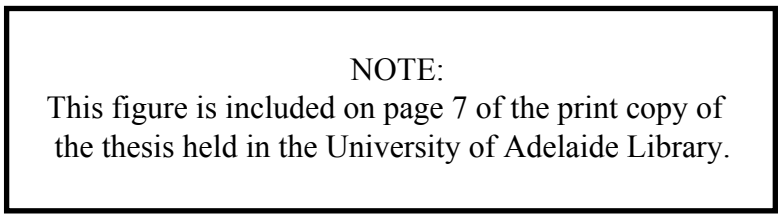

Figure 2.1.: Observed energy spectrum of primary cosmic rays, measured by many different experiments as listed in the legend [5].

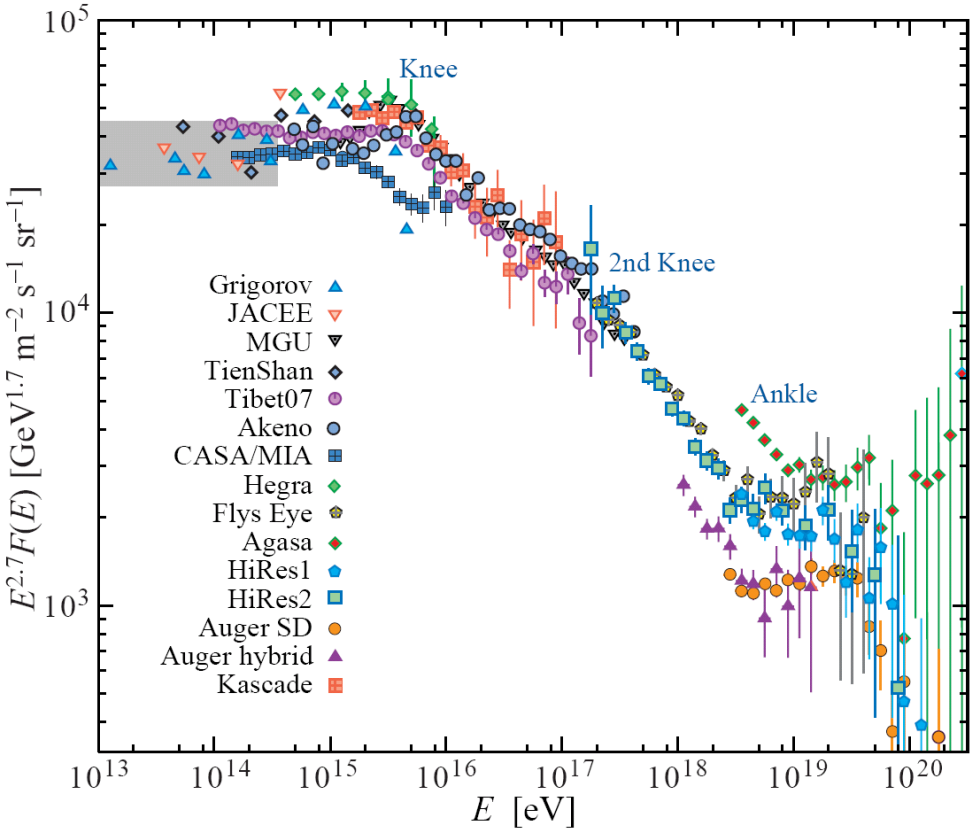

Figure 2.2.: Cosmic ray spectrum [6]. The cosmic ray flux is scaled with $E^{2.7}$ to emphasise the characteristic features. The knee at about 3×10^{15} eV and the ankle around 5×10^{18} eV can be observed. Furthermore a suppression in the flux around 10^{20} eV is visible in the spectra of HiRes and Auger.

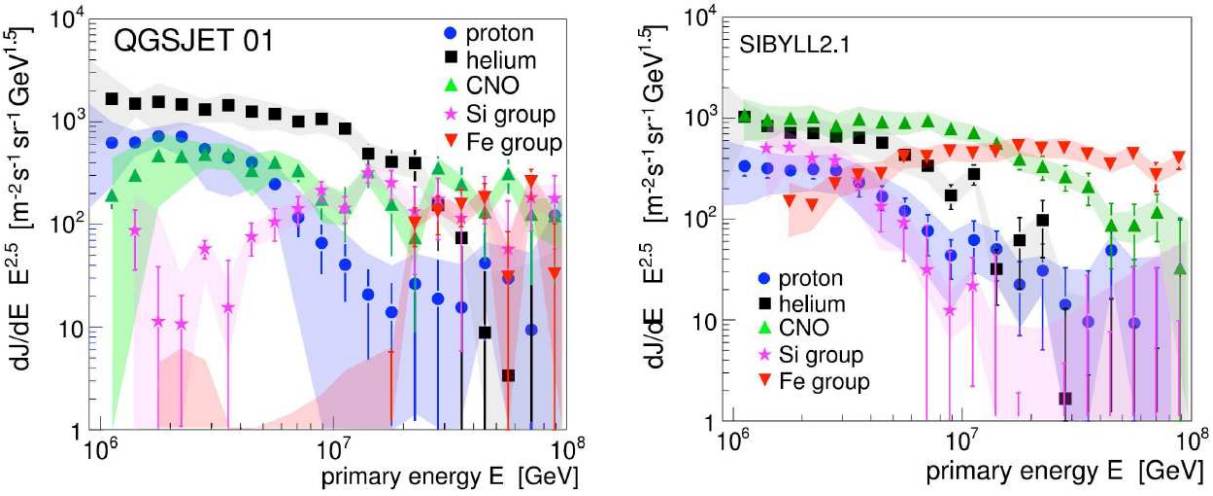

Figure 2.3.: Cosmic-ray energy spectrum for five groups of elements as reconstructed by the KASCADE experiment using the hadronic interaction models: Right: QGSJET 01, and Left: SIBYLL 2.1 to interpret the measured data[9]

NOTE:
This figure is included on page 9 of the print copy of the thesis held in the University of Adelaide Library.

Figure 2.4.: Here we have the energy spectra from HiRes1 and HiRes2 monocular, and from AGASA. The solid line represents a best fit to the HiRes data. Not only is the AGASA data systematically higher, it doesn't indicate a suppression in flux at the highest energies. Figure from [14].

2.2. Composition

The composition of cosmic rays can yield important information about sources and propagation effects. There are many theories of cosmic ray origin, with each proposing a different cosmic ray composition. 'Bottom-up' models hypothesise high energy cosmic rays being produced in active galactic nuclei, gamma-ray bursts and radio galaxy hot-spots, in which low energy cosmic rays are accelerated up to extremely high energies. 'Top-down' models are based on decays of exotic particles such as topological defects or super-heavy dark matter particles. These latter models predict a significant gamma ray component and no heavy nuclei. So, by measuring the cosmic ray composition, it could be possible to discriminate between the two.

Figure 2.5.: Compilation of data on depth of maximum as a function of energy from different experiments compared with predictions for different models [15].

At low energies (E$\leqslant 10^{14}$ eV) it is possible to measure the composition of cosmic rays directly using balloon experiments. We see an excess over the universal composition of light nuclei such as lithium, beryllium and boron, which result from spallation of heavier nuclei like carbon, oxygen and iron, as they propagate through the galaxy.

Above 10^{14} eV we can only observe the particle cascade (EAS) induced by the cosmic ray as it interacts in the atmosphere. Light nuclei penetrate deeper into the atmosphere before undergoing their first interaction. This indicates that the extensive air showers that they induce will reach their maximum size deeper in the atmosphere on average than an EAS induced by a heavy nucleus. However, in the first interaction in the atmosphere, a heavy nucleus breaks up into many protons and neutrons of lower energy that create sub-showers. As the hadrons initiating these sub-showers have a smaller energy, their sub-showers will maximise earlier in the atmosphere than if all of that energy had been carried by one proton. These two factors affect the depth of shower maximum. By measuring the longitudinal profile of a shower, we can now obtain good measurements of the depth of shower maximum X_{max} for individual showers. Using simulations we can calculate the average value of X_{max} that we would expect for a given composition and energy but, due to large shower to shower fluctuations, we cannot determine whether an individual CR was a proton or an iron nucleus. We can only determine the average composition at a given energy, which is based on the assumption that our interaction models, extrapolated from accelerators, are correct.

The average value of X_{max} , $< X_{max} >$, is related to the mean logarithmic mass $< ln\, A >$as [42]

$$< ln\, A >= \frac{X_{max} - X_{max}^{Fe}}{X_{max}^{p} - X_{max}^{Fe}}. \tag{2.1}$$

Here, X_{max} is the observed depth of shower maximum, and X_{max}^{Fe} and X_{max}^{p} are the depths of shower maximum for iron and proton induced showers respectively.

Another composition sensitive quantity is the natural spread of X_{max} at a given energy. Proton induced showers have larger fluctuations in the depth of shower maximum than iron induced showers. The mean values of X_{max} and the RMS are displayed in figure 2.6 for

several compositions calculated using hadronic interaction models SIBYLL2.1, QGSJET II and QSJET01 [16]. These show that different interaction models predict different values for X_{max} given a fixed composition.

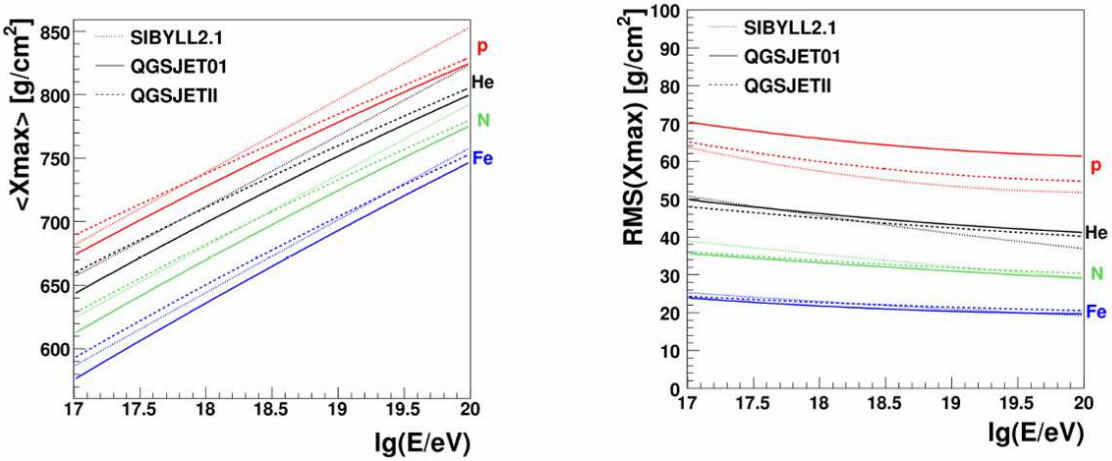

Figure 2.6.: The mean values of X_{max} and the RMS of X_{max} for proton, He, N and Fe calculated using hadronic interaction models SIBYLL2.1, QGJET II and QSJET01. Figure from [17].

Another method for studying composition is to compare the energy spectrum that we observe with different calculated source spectra, and see if there is a particular composition that best explains the features in the spectrum. Figures 2.7, 2.8 and 2.9 show the spectra measured by Akeno/AGASA (ground array experiments) and HiRes (fluorescence detectors) and compare them with either a pure proton composition or a mixed composition and take into account energy losses. The inferred galactic component in these plots comes from the subtraction of the modelled extragalactic component from the experimental data.

This way of approaching the composition relies on an understanding of the mechanisms accelerating the cosmic rays, plus high statistics to pin down the exact energy of the GZK suppression.

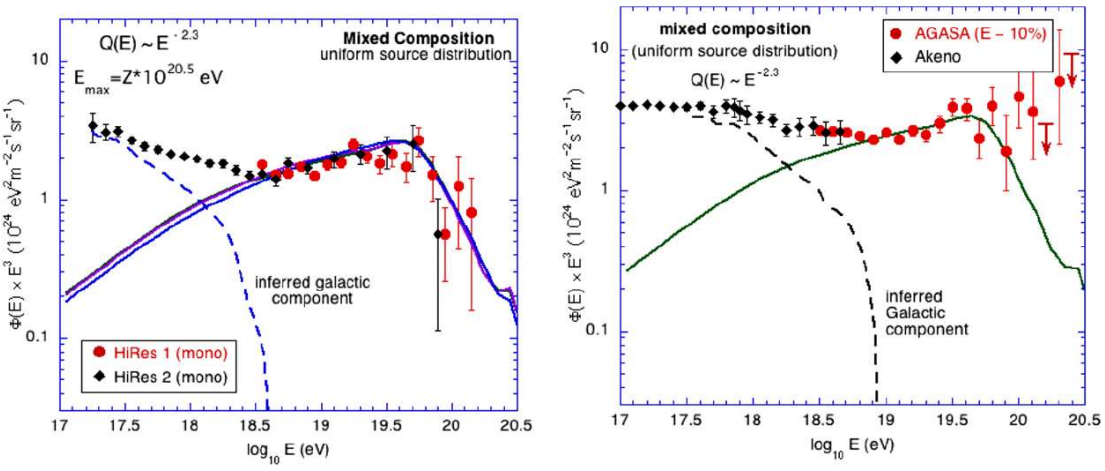

Figure 2.7.: Propagated spectra, $\Phi(E)\,E^3$, for a mixed extragalactic cosmic ray source composition, compared with the HiRes monocular data and the Akeno/AGASA data. In both cases the source spectrum has a power law index of $\alpha = 2.3$, and the ankle corresponds to the transition from the galactic to the extragalactic component [17].

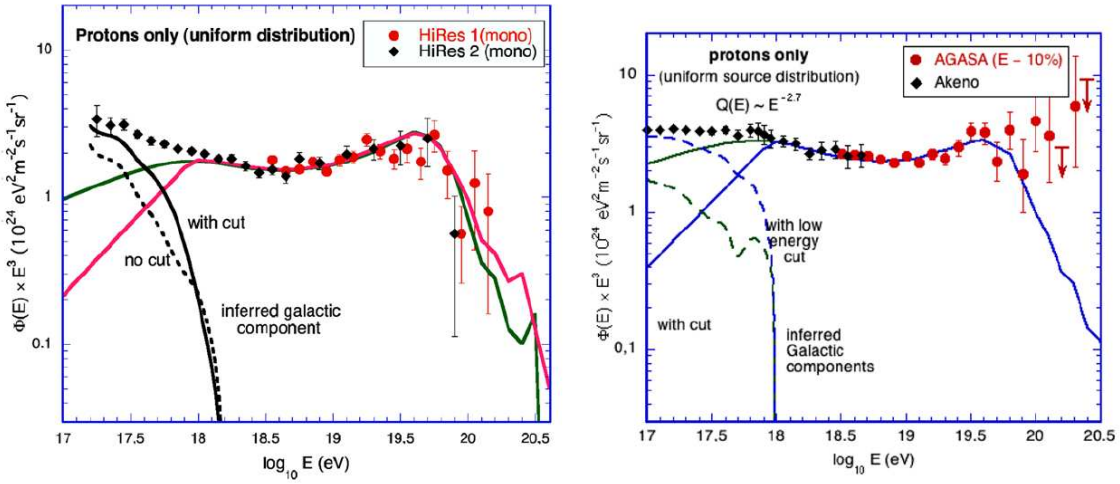

Figure 2.8.: Same as Figure 2.7, for a pure proton extra galactic cosmic ray source. The injection spectral index is $\alpha = 2.6$ for the HiRes data (left) and $\alpha = 2.7$ for the Akeno AGASA data (right). Two different propagated spectra and the corresponding inferred galactic cosmic ray component are shown, for an injection spectrum either with or without a low energy cut [17].

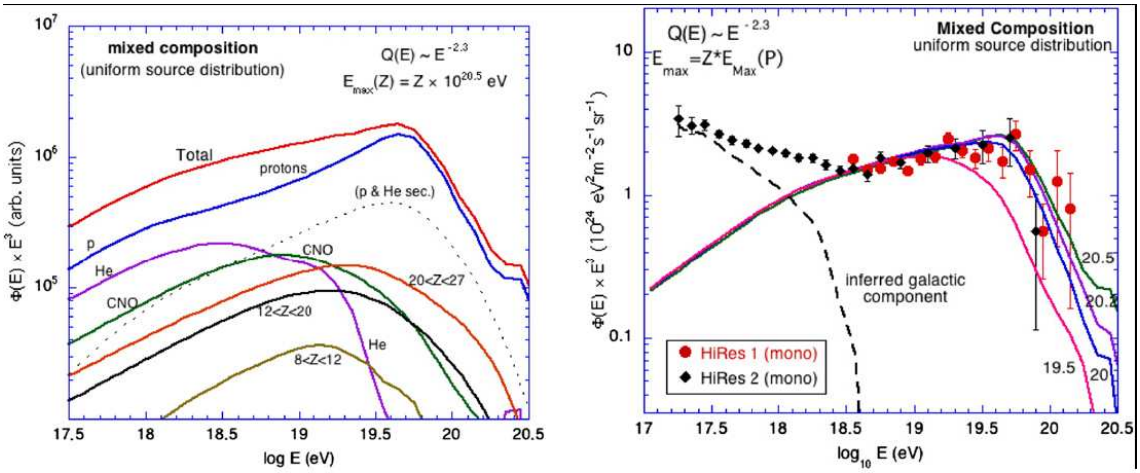

Figure 2.9.: Left: Contribution of different elements to the propagated mixed composition spectrum. The GZK suppression can be seen at 10^{19} eV for He and 2×10^{19} eV for the CNO group. The dotted line shows the contribution of the secondary low mass nuclei (protons and He) resulting from the photo-dissociation of heavier nuclei. That contribution is responsible for the bump in the spectrum at 5×10^{19} eV. Right: Propagated spectra are shown for different values of the maximum proton energy, $E_{max}(p) = 10^a$ eV, with $a = 19.5$, 20.0, 20.2 and 20.5 [17].

2.3. Origin of UHECR

2.3.1. Fermi Acceleration

In 1949 Fermi proposed a mechanism that would be capable of accelerating relativistic particles to high energies. The mechanism involves the interaction of the particles with moving magnetised gas clouds [18]. This theory can be extended to account for even higher energies by considering shock acceleration. Figure 2.10 shows two acceleration processes based on Fermi's theory.

Figure 2.10.: Left: second order Fermi acceleration mechanism occurring in a moving magnetised cloud. Right: first order Fermi acceleration occurring in strong plane shocks [19]

Beginning with the figure on the left, we have a particle of initial energy E_1 entering a gas cloud at angle θ_1 with respect to the velocity of the cloud. The particle upon entering the cloud then scatters on irregularities in the cloud's magnetic field. The gain in energy of the particle can be determined from the application of Lorentz transformations between the laboratory frame and the primed frame of the cloud. The particle scatters collision-less on the magnetic field of the cloud. The particle's energy in the cloud frame is:

$$E_1' = \gamma E_1(1 - \beta cos\theta_1) \tag{2.2}$$

where $\beta = {}^{v}/_{c}$ and $\gamma = {}^{1}/\sqrt{1-\beta^2}$ are that of the cloud. After the particle has left the cloud, its energy in the laboratory frame is:

$$E_2 = \gamma E_2'(1 + \beta cos\theta_2') \tag{2.3}$$

where θ_2' is the angle at which the particle leaves the cloud with respect to the cloud's velocity. As in the cloud's frame there is no change in energy of the particle, $E_1' = E_2'$, and we can combine 2.2 and 2.3 to give us the relative change in energy of the particle in the lab frame:

$$\frac{\Delta E}{E} = \frac{E_2 - E_1}{E_1} = \frac{1 - \beta cos\theta_1 + \beta cos\theta_2' - \beta^2 cos\theta_1 cos\theta_2'}{1 - \beta^2} - 1 \tag{2.4}$$

This can be simplified to:

$$\frac{\Delta E}{E} = \frac{1 + \frac{1}{3}\beta^2}{1 - \beta^2} - 1 \simeq \frac{4}{3}\beta^2 \tag{2.5}$$

by setting $cos\theta_2' = 0$ on average due to the random nature of the scatters. Also by saying that as the collision probability depends on the relative velocity of the particle with respect to the cloud and as $\beta \ll 1$, we can take an average over the solid angle, and set $cos\theta_1 = -\frac{\beta}{3}$. The result on average is an increase in the particles energy. As $\beta \ll 1$ and $\frac{\Delta E}{E} \propto \beta^2$, the acceleration of the particle is small.

Illustrated on the right in figure 2.10 is a more efficient mechanism for the acceleration of charged particles. The acceleration takes place at the location of strong shocks, such as in supernovae (SN) or active galactic nuclei (AGN) relativistic jets. Let us use a SN as our example. During a SN, many solar masses of material are ejected at speeds of the order $V_p \sim 10^4\,\mathrm{km\,s^{-1}}$. The result is a shock wave that then propagates into the interstellar medium (ISM). The velocity of the shock V_s is related to V_p by the relationship:

$$V_s = \frac{R}{(R-1)V_p} \tag{2.6}$$

where R is the compression ratio.

Particles can either cross the shock from downstream to upstream $\left(cos\theta'_2 = \frac{2}{3}\right)$ or from upstream to downstream $\left(cos\theta_1 = -\frac{2}{3}\right)$. By substituting these values back into Eq.2.3 we obtain:

$$\frac{\Delta E}{E} = \frac{1 + \frac{4}{3}\beta + \frac{4}{9}\beta^2}{1-\beta^2} - 1 \simeq \frac{4}{3}\beta \tag{2.7}$$

This is then first order Fermi acceleration, also known as diffusive shock acceleration. We now have to calculate the probability that the particles will be lost downstream and the probability that they will cross the shock.

The probability that a particle will be lost downstream is $P_{lost} = \rho_{cr} V_s/R$ where V_s/R is the velocity of particles flowing away downstream in the rest frame of the shock, and ρ_{cr} is the cosmic ray density. The probability of a particle moving at speed v crossing the shock is:

$$P_{cross} = \rho_{cr}\,\frac{1}{2}\int_{-V_s/v}^{1} (V_s + v\,cos\theta)\,d(cos\theta) \simeq \rho_{cr}\,\frac{v}{4}. \tag{2.8}$$

The probability that the particle will escape the region is obtained by dividing Eq.2.7 by Eq.2.8. giving $P_{esc} \approx 4V_s/Rv$. Therefore the number of particles still in the accelerating region after (n) cycles is $(1 - P_{esc})^n$, and the energy attained after n collisions is:

$$E = E_0(1+\xi)^n, \tag{2.9}$$

where ξ is the relative energy gain $\Delta E/E$. Rearranging equation 2.9 we obtain the number of cycles n required to reach an energy E

$$n = \frac{ln(E/E_0)}{ln(1+\xi)} \tag{2.10}$$

It can be shown that using equation 2.10, we can solve for an integral energy spectrum in the form of a power law.

$$ln\, N(\geq E) = A + \frac{ln(E/E_0)}{ln(1+\xi)}\, ln(1 - P_{esc}) = B - (\alpha - 1)\, ln\, E, \tag{2.11}$$

where

$$\alpha = 1 - \frac{ln(1 - P_{esc})}{ln(1+\xi)} \approx \frac{R+2}{R-1}, \tag{2.12}$$

and A and B are constants.

Thus the differential power law index, $-\alpha$, depends only on the compression ratio of the shock, and the maximum energy that can be achieved depends on the time the particle spends in the region.

2.3.2. Astrophysical Sources

There are limits on the characteristics of candidate sources, based on the properties of the cosmic ray spectrum that we observe. For a source to be capable of accelerating particles to energies of $E > 10^{20}$ eV the size of its accelerating region must be comparable to the Larmor radius of the particle in the accelerator's magnetic field. There are also limits on the strength of the accelerator's magnetic field, such that synchrotron losses are less than the energy gained by the particle. The total magnetic energy available in a source with magnetic field strength B, and an accelerating region of size L is:

$$W = \left(\frac{B^2}{4\pi}\right)\left(\frac{4}{3}\pi L^3\right). \tag{2.13}$$

For example, for a particle to leave the region with $E = 10^{20}$ eV, the energy in the magnetic field, W, must be greater than 10^{57} ergs [1] [20]. An example of such a source could be a radio galaxy. The above constraints do not impose any limitations on the acceleration process

[1] Assuming $B < 0.1$ G so that synchrotron losses do not dominate.

itself. It has been shown that diffusive shock acceleration is adequate for explaining particle energies up to 10^{15} eV (eg. supernovae), but it is not yet well understood what mechanism could explain higher energies. It has been argued that particles could be accelerated to energies of 10^{18} eV through interactions with multiple supernovae as they propagate through the ISM. In this scenario the particles most likely to reach the highest energies would be heavy nuclei such as iron.

It has been show that the maximum energy a particle can attain through diffusive shock acceleration is [21]:

$$E \propto Ze\,B\,L\,\beta\,c \tag{2.14}$$

where Ze is the charge of the nucleus and βc is the shock speed. If we set β to a fixed value then for a given particle energy we can obtain plots of B vs. L. This then allows us to see if known astrophysical sources satisfy the conditions required to accelerate particles to a specific energy [22]. These plots are known as Hillas plots.

From Figure 2.11 we can see that there are many candidate sources, but there is still much debate over which values of β, B and L to assign to various sources [20].

2.3.3. Propagation

There are two aspects of the propagation of UHECR that we need to address: propagation through the galaxy and propagation through intergalactic space. Within a galaxy, UHECR are deflected by the galactic magnetic fields, with the deflection angle $\alpha \sim d \times r_L$, where d is the distance travelled by the particle through the magnetic field and r_L is the Larmor radius. The Larmor radius is given by

$$r_L = 1.08\,\frac{E_{15}}{Z\,B_{\mu G}} pc, \tag{2.15}$$

where E_{15} is the energy in units of 10^{15} eV and Z is the atomic number of the particle. Above 10^{18} eV the Larmor radius is roughly the width of our galactic disk [2]. This means

[2] B$\sim$ 3 μG, $r_L \sim$ 300 pc for protons.

that at these energies the particles escape, and we would expect anisotropy. Even with the presence of a turbulent magnetic halo along with a combination of turbulent and regular magnetic fields in the disk, we should observe strong anisotropy above 10^{19} eV for galactic sources.

2.3.4. Energy losses and GZK processes

At the highest energies, energy losses via interactions with the microwave, infrared and radio radiation becomes important[20].

After the discovery of the cosmic microwave background (CMB) [24], it was predicted by Greisen [11], Zatsepin and Kuzmin [12] in 1966 that above 6×10^{19} eV, photo-pion production on the microwave background would cause a strong suppression (GZK cut-off) of the spectrum.

$$p + \gamma_{2.7K} \longrightarrow n + \pi^+,\ p + \gamma_{2.7K} \longrightarrow p + \pi^\circ \tag{2.16}$$

$$p + \gamma_{2.7K} \longrightarrow p + e^+ + e^- \tag{2.17}$$

The CMB photons have an energy of 6×10^{-4} eV and the density is $400\,\mathrm{cm}^{-3}$. For pair production, Eq 2.17, the threshold energy is approximately 10^{18} eV, the mean free path of the interaction is 1Mpc, and the energy loss per interaction is only 0.1 %. For photo-pion production (Eq.2.6) the threshold energy is 6×10^{19} eV and the mean free path is 6 Mpc, but the energy loss per interaction is 20 %.

Many calculations have been made to determine the shape of the resulting cosmic ray spectrum from particles propagating through the CMB with both Monte Carlo methods and analytical methods and all are within good agreement with each other. Some of these are shown in figure 2.12.

For heavy nuclei with mass number A, photo-disintegration [31] and pair production [32] are important energy loss processes to consider. The energy loss due to interactions with infrared photons is significant below 5×10^{19} eV and above 2×10^{20} eV for the CMB.

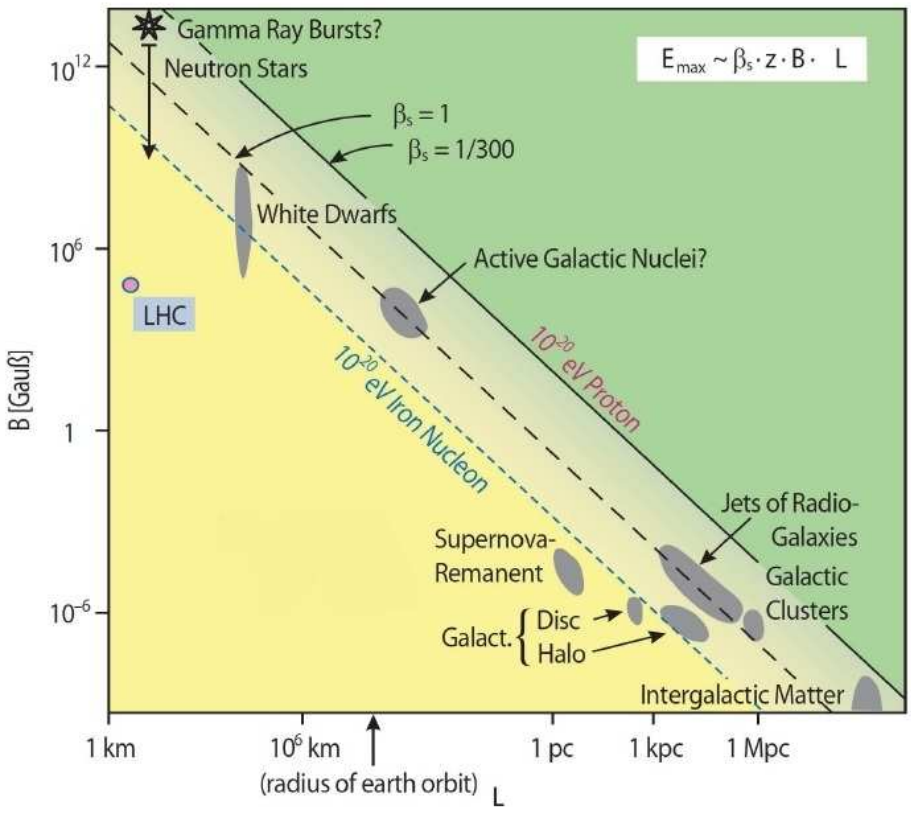

Figure 2.11.: Hillas plot showing the size (radius L) and magnetic field strength (B) of possible UHECR sources. Lines indicating the minimum values of L and B required to accelerate protons and iron to 10^{20} eV are indicated in the figure. Any objects below these lines are not capable of accelerating these particles to ultra-high energies [23] .

Figure 2.12.: The attenuation length of proton, iron, and gamma-ray primaries in the microwave, infrared, and radio background radiations as a function of energy. Proton 1 is from Yoshida and Teshima [25] and proton 2 from Protheroe and Johnson [26]. Results from Rachen and Biermann[27] and Berezinsky and Grigoreva[28] lie between protons 1 and 2. That of iron is from Stecker and Salamon[29]. That of gamma rays in the total low-energy photon background down to kHz frequencies is shown by the dot-dashed curve from Bhattacharjee and Sigl[30]. Figure comes from [20].

2.4. Anisotropy

Below 10^{17} eV the flux of cosmic rays appears to be isotropic. This is to be expected due to the large deflections that charged particles at these energies incur due to the galactic magnetic fields. There have been claims by the AGASA collaboration that a $4.5\,\sigma$ excess of cosmic rays in the energy range $10^{18} - 10^{18.4}$ exists 10° from the our galactic centre [33], as shown in figure 2.13. Many other experiments have searched for a similar excess in their data, with some observing an excess, and some not. What is needed is large statistics with low uncertainty on the reconstructed energies, to solve such debates.

At the highest energies, we hope to be able to identify point sources of cosmic rays, utilising the fact that, for proton primaries, the deflection angles are of the order of a few degrees. From the energy loss processes discussed earlier, we can calculate that 50 % of the cosmic rays that we observe with $E > 10^{20}$ eV have come from within 20 Mpc. Upper limits to the extragalactic magnetic field have been derived from measurements of Faraday rotation of emission from powerful radio galaxies ($B \sim 10^{-9}$ G [34]). It is possible that through the study of UHECR we may be able to measure the extragalactic magnetic field strength. This may be done by measuring the deflection angle, $\theta(E)$, of cosmic rays from a source as a function of their measured energy.

$$\theta(E) = 0.025^{\circ} \left(\frac{d}{\lambda}\right)^{\frac{1}{2}} \left(\frac{\lambda}{10Mpc}\right) \left(\frac{B}{10^{-11}G}\right) \left(\frac{E}{10^{20}eV}\right)^{-1} \tag{2.18}$$

Here, d is the distance to the source in Mpc, and λ is the interaction length in Mpc.

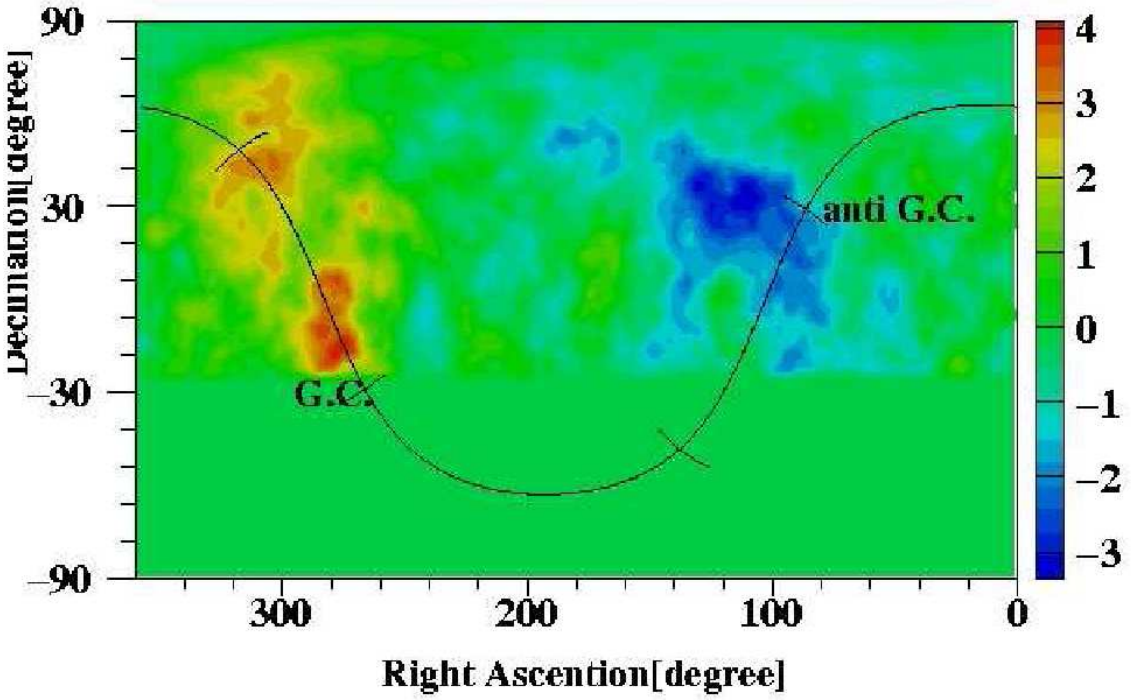

Figure 2.13.: Significance map showing 4 σ excess (see σ scale on right hand side of figure) near the direction of the Galactic Centre. Near the direction of the anti-Galactic centre, a 3.7σ deficit is seen by AGASA [35].

3. Physics of Extensive Air Showers

When high energy cosmic rays enter the atmosphere they produce large cascades of secondary particles and photons through interactions with the molecular atmosphere. These cascades are referred to as extensive air showers (EAS).

An extensive air shower has many components. These include a hadronic core, a muonic component, an electromagnetic component, as well as fluorescence and Cherenkov photons. Here I will present the components of EAS and some models that describe their development in the atmosphere.

3.1. Heitler Model

Using a simple model proposed by Heitler [36] for electromagnetic showers we can describe some of the main features of EAS development. If we take the primary cosmic ray to be a high energy photon, with energy E_i, then the result is an electromagnetic cascade. Here we will assume that energy is divided equally among secondary particles and that each interaction (both Bremsstrahlung and pair production) occurs after a fixed atmospheric depth (λ) has been traversed. The primary photon undergoes pair production, and then each of the secondary particles undergoes Bremsstrahlung, producing more photons. The cascade continues to grow, with the number of particles doubling after each interaction length λ. At an atmospheric slant depth X the number of particles in the shower is given by

$$N(X) = 2^{X/\lambda} \tag{3.1}$$

The doubling continues until the particle energy falls below some critical energy E_c. Then energy losses due to Compton scattering, ionisation and the photoelectric effect become dominant, and the shower attenuates. The shower reaches its maximum size when the particle energy is equal to E_c. Therefore the number of particles at the depth of shower maximum X_{max} is:

$$N\left(X_{max}\right) = E_i/E_c \tag{3.2}$$

By setting $X = X_{max}$ in Eq.3.1 and equating it with Eq.3.2 we find an expression for X_{max} in terms of the interaction length λ, the primary energy and the critical energy.

$$X_{max} = \lambda \, \frac{lnE_i/E_c}{ln2} \tag{3.3}$$

While this relationship was found using an electromagnetic cascade, to a first approximation, we can still say correctly that $X_{max} \propto ln(E_i)$ for hadron induced showers, as they are largely superpositions of electromagnetic sub-showers [37].

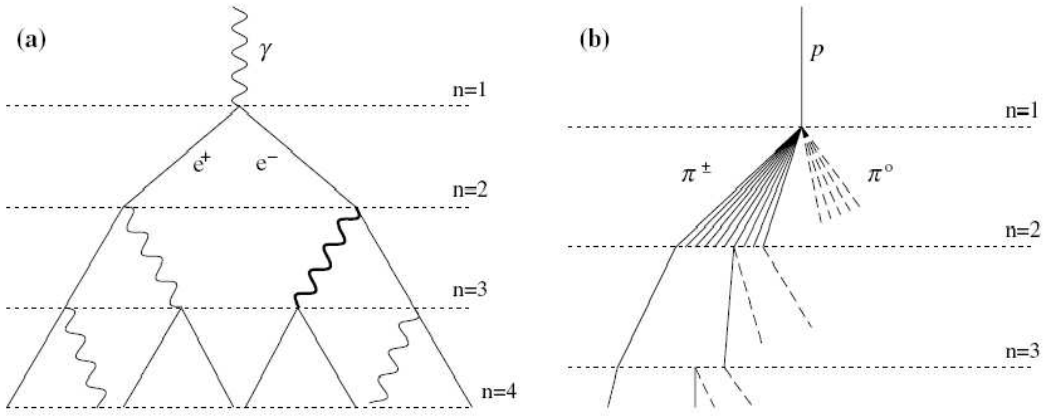

Figure 3.1.: (a) shows an electromagnetic cascade, and (b) shows a hadronic induced shower (not to scale) [38].

3.2. Hadronic component

The extensive air showers detected at the Pierre Auger Observatory are predominately initiated by nuclei. Taking the primary cosmic ray to be a proton, its first atmospheric interaction with a nucleus N is of the form

$$p + N \longrightarrow p' + N' + \pi^-, \pi^+, \pi^0. \tag{3.4}$$

In this first interaction, the proton typically gives up half of its energy. After the interaction, the proton p' will go on to produce more hadronic reactions. Alternatively, the proton could break the nucleus into its hadronic components, producing even more protons and neutrons which also interact with other nuclei. The production angles are small so the hadrons form the core of the shower. Pions are produced as secondary particles and these feed the electromagnetic and muonic components until the hadronic core is depleted. This occurs when the mean hadron energy falls below the energy required for pion production.

3.3. Electromagnetic component

The electromagnetic component is generated by the neutral pions π^0 produced in hadronic interactions. These decay immediately ($t_{\frac{1}{2}} = 7.6 \times 10^{-17}\,\mathrm{s}$) after production.

$$\pi^0 \longrightarrow \gamma + \gamma \tag{3.5}$$

As in the Heitler model, pair production, $\gamma \longrightarrow e^+ + e^-$, and Bremsstrahlung processes, $e^- \longrightarrow e^{-\prime} + \gamma$, continue to produce more photons and electrons. Each photon produced in the shower then generates its own electromagnetic cascade, and the result is an electromagnetic component that is the superposition of many cascades initiated at different heights. From electromagnetic cascade theory, we have the number of electrons/positrons N_e in a photon-initiated shower given by [37]:

$$N_e(E_i, t) \simeq \frac{0.31}{\sqrt{t_{max}}}\, exp\left[t\left(1 - \frac{3}{2}ln(s)\right)\right], \tag{3.6}$$

where

$$t \equiv X/X_0 \tag{3.7}$$

$$t_{max} = ln(E_i/E_c) \tag{3.8}$$

The atmospheric depth is denoted by X [$\mathrm{g\,cm^{-2}}$], and X_0 is the radiation length (the average distance after which an interaction will occur). Here E_i is the energy of the primary particle, and E_c is the critical energy below which a shower stops growing and begins to attenuate.

In equation 3.6, the shower age (s) is a measure of shower evolution, and has a value of 1.0 at shower maximum ($t = t_{max}$).

$$s \equiv \frac{3t}{t + 2t_{max}} \tag{3.9}$$

The angular spread of the electromagnetic component is largely due to multiple Coulomb scattering of low energy electrons. Their lateral spread, as a function of distance from the shower axis r and the atmospheric depth X, can be described by the Nishimura Kamata-Greisen (NKG) formula [39]:

$$\rho_N(X, r) = \frac{N_e(X)}{r_M^2} \left(\frac{r}{r_M}\right)^{s-2} \left(1 + \frac{r}{r_M}\right)^{s-4.5} \frac{\Gamma(4.5 - s)}{2\pi\Gamma(s)\Gamma(4.5 - 2s)} \tag{3.10}$$

The parameter r_M is the Molière radius given by;

$$r_M = E_s \frac{X_l}{\epsilon_0} \tag{3.11}$$

where $E_s = 21\,\mathrm{MeV}$ is the scale energy, $\epsilon_0 = 81\,\mathrm{MeV}$ is the critical energy and $X_l = 37\,\mathrm{g\,cm^{-2}}$.

The Molière radius is a natural transverse scale set by multiple scattering and determines the lateral spread of the shower. Since the electron radiation length (cascade unit) in air is dependent on the atmospheric temperature and pressure, the Molière radius varies along the shower path. The distribution of particles in the shower at a given depth then depends on the history of the changes in r_M along the shower path, rather than the local r_M value at that depth. To take this into account, for a given atmospheric depth, the r_M value at two cascade units above this depth may be used [40].

The NKG formula isn't sufficient to describe the lateral distribution of hadron induced showers. This is better described by [41]

$$\rho(r) = C \left(\frac{r}{r_M}\right)^{-1.2} \left(1 + \frac{r}{r_M}\right)^{-(\eta-1.2)} \left(1 + \left(\frac{r}{1000}\right)^2\right)^{-\delta}; \tag{3.12}$$

where C and δ are constants, and η is dependent on the zenith angle of the shower. Various experiments have determined C, $\delta$and η by fitting the function to their ground array data or through simulation.

3.4. Muon component

Charged pions produced in the hadronic interactions create the muon component of the shower and also produce neutrinos.

$$\pi^- \longrightarrow \mu^- + \bar{\nu}_\mu \tag{3.13}$$

$$\pi^+ \longrightarrow \mu^+ + \nu_\mu \tag{3.14}$$

Most muons have a lifetime that is long enough due to relativistic effects to allow them to reach sea level. They lose energy through ionisation, Bremsstrahlung and pair production. For muon Bremsstrahlung the mean free path is $10^5\,\mathrm{g\,cm^{-2}}$ at 1 GeV, and it slowly decreases with increasing energy. The Bremsstrahlung mean free path is over an order of magnitude greater than the total depth of the atmosphere ($1030\,\mathrm{g\,cm^{-2}}$ at sea level), and

therefore it has a negligible effect. Pair production can occur in the field of a nucleus. This has a similar mean free path at 1 GeV as for Bremsstrahlung, but it falls sharply with increasing energy to $100\,\mathrm{g\,cm^{-2}}$ at 1 TeV. This is the dominant energy loss for muons with $\mathrm{E} > 1\,\mathrm{TeV}$.

Ionisation energy loss is a continuous process, and in air is approximately $2.2\,\mathrm{MeV\,g^{-1}\,cm^2}$. It is independent of the mass of the particle causing the ionisation and is the dominant energy loss mechanism for $\mathrm{E} < 1\mathrm{TeV}$, but the relative rate of energy loss is slow. So, at any stage of the shower development, the number of muons in the shower is roughly the sum of all muons produced. They are no longer readily produced as the hadronic component decays, so their number remains approximately constant from the depth of shower maximum to the ground.

As the muon attenuation is slow, the total muon number can be used as an energy estimator. This can be problematic, as if the shower has not reached maximum before it reaches the ground the shower energy is underestimated. Also there is a difference in the number of muons produced by proton and iron nucleus primaries, so the energy of iron showers would be underestimated.

Muons undergo minimal Coulomb scattering and hence their lateral spread results from their production angles. This was first parametrised by Greisen [42] as

$$\rho_\mu(r) = N_\mu \left(\frac{C_\mu}{R_0^2}\right)\left(\frac{r}{R_0}\right)^{-\alpha}\left(1+\frac{r}{R_0}\right)^{-\beta} \tag{3.15}$$

where $C_\mu$is a normalisation constant, R_0 is a zenith angle dependent scale factor and $\rho_\mu(r)$ is the number of muons per square meter at core distance r. This function has been modified by various groups to fit their specific array arrangements.

3.5. Longitudinal Profile

The longitudinal profile is defined as the number of ionising particles as a function of atmospheric depth, $N(X)$. This development is largely dependent on the proton-air and

pion-air cross-sections, inelasticity and multiplicity. The proton-air cross-section will determine the depth of the first interaction, and hence the depth of shower maximum. High inelasticity means that more energy is given to secondary particles, and high multiplicity means that that energy is distributed amongst more particles. This leads to a faster shower development. Conversely if the inelasticity and multiplicity are low then the shower develops more slowly and shower maximum is reached much deeper in the atmosphere.

To describe the longitudinal profile of an EAS, including all components, we have to resort to a empirical parametrisation. The one most commonly used is that developed by Gaisser and Hillas [43]:

$$N(X) = N_{max} \left(\frac{X - X_0}{X_{max} - X_0} \right)^{\frac{X_{max} - X_0}{\lambda}} exp \left[\frac{X_{max} - X}{\lambda} \right] \tag{3.16}$$

where N_{max} is the shower size at shower maximum, λ is dependent on the proton-air cross-section, and X_0 is a free parameter.

An example of a longitudinal profile measured by the Fly's Eye experiment is shown in figure 3.2. This was the highest energy event recorded by the fluorescence detector, with a reconstructed energy of 3×10^{20} eV and $N_{max} \approx 2 \times 10^{11}$ [44]. The energy estimate comes from integrating the longitudinal profile to determine the total number of electrons in the shower, and multiplying by the mean electron energy.

3.6. Fluorescence Light

Extensive air showers are made up of many charged particles, mainly electrons and positrons as discussed in the above sections. Their particles deposit energy in the atmosphere by ionising and exciting the atmospheric molecules. The induced excited states are short lived, and the molecules de-excite producing fluorescence light [1]. The wavelengths produced are characteristic of the energy levels within the individual molecules.

[1] Molecules can also de-excite by collisions with other molecules, which happens to be a larger effect than fluorescence production.

Figure 3.2.: Longitudinal profile of the highest energy shower detected by the Fly's Eye experiment. The reconstructed energy was 3×10^{20} eV [44].

3.6.1. Electron excitation and radiative de-excitation

Within molecular nitrogen, the electrons exist in specific electronic states. Each electronic state is split into vibrational levels, and furthermore each vibrational level is split into rotational levels. The fine structure of the rotational spectra are not able to be resolved by most experiments. Instead we observe the vibrational structure and the corresponding molecular bands have their spectral width and shape determined by the rotational structure. The majority of the nitrogen fluorescence spectrum comes from the 2^{nd} positive system (2P), $C^3\Pi_u \rightarrow B^3\Pi_g$, and the first negative system (1N), $B^2\Sigma_u^+ \rightarrow X^2\Sigma_g^+$. The 2P system comes from the excitation of molecular nitrogen, and the 1N system is the result of transitions within the singly ionised nitrogen molecule. This is illustrated in figure 3.3. The wavelengths corresponding to transitions are shown in figure 3.4. Also shown in

figure 3.3 are the wavelengths corresponding to weak bands from a system known as the Gaydon-Herman (GH) system [45, 46].

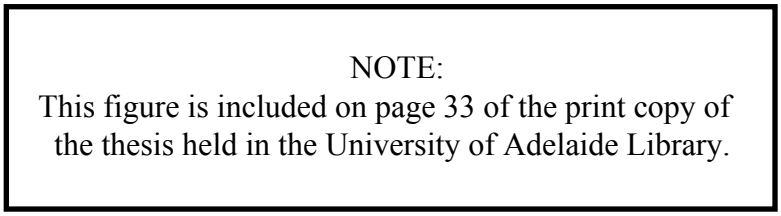

Figure 3.3.: Molecular levels of N_2 and N_2^+. The broad arrows represent the main transitions (1N and 2P systems) [47].

The cross-section for excitation as a function of energy is shown in figure 3.5. The 2P system has a sharp maximum at 15 eV and then, due to the optically forbidden nature of the transitions, the cross section falls off as E^{-2}. The 1N system has a softer maximum at 100 eV, and then a $(logE)/E$ decrease at higher energies [50, 49]. The fluorescence induced by electrons with $E >$ keV actually arises from the secondary electrons produced by the primary electron. As the number of low energy electrons arising from each high energy electron as it traverses a given volume is proportional to the energy deposited within that volume, it then follows that the fluorescence emission will also be proportional to the

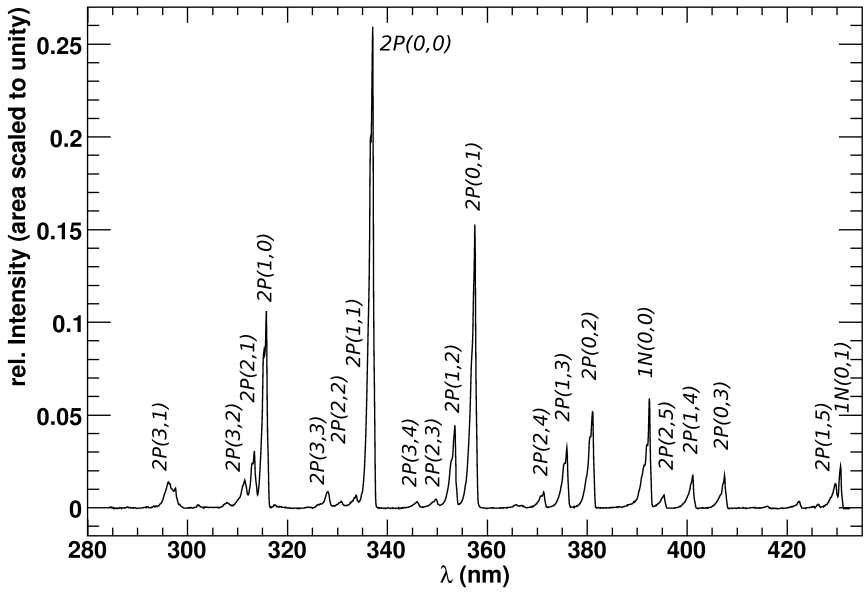

Figure 3.4.: Air fluorescence spectrum resulting from excitation of air molecules by 3 MeV electrons at 800 hPa, as measured by the AIRFLY Collaboration [48].

energy deposited.

As the shower particles have a large range of energies, the proportionality of the fluorescence yield to the energy deposited in the atmosphere by those particles needs to be verified over the entire energy range. The AIRFLY Collaboration have tested this using electrons with energies between 6-30 keV, 0.5-15 MeV and 50-420 MeV, using a range of accelerators [51]. They found that the deviations from proportionality were 3 % and 5 % in the MeV and keV ranges respectively (at the 95 % confidence level)

For a given electronic state, the cross-section for the excitation to a vibrational level ν is proportional to the Frank-Condon factor $q_{\nu\to\nu'}$, where $q_{\nu\to\nu'}$ is equal to the overlap integral between the vibrational wave functions of the lower and upper levels of the excitation process. The probability of the emission of a fluorescence photon from the transition $\nu \to \nu'$ is proportional to the optical cross-section defined as:

$$\sigma_{\nu\nu'} = \sigma_\nu \frac{A_{\nu\nu'}}{\Sigma_{\nu\to\nu'} A_{\nu\nu'}} = \sigma_\nu B^{\nu\nu'} \tag{3.17}$$

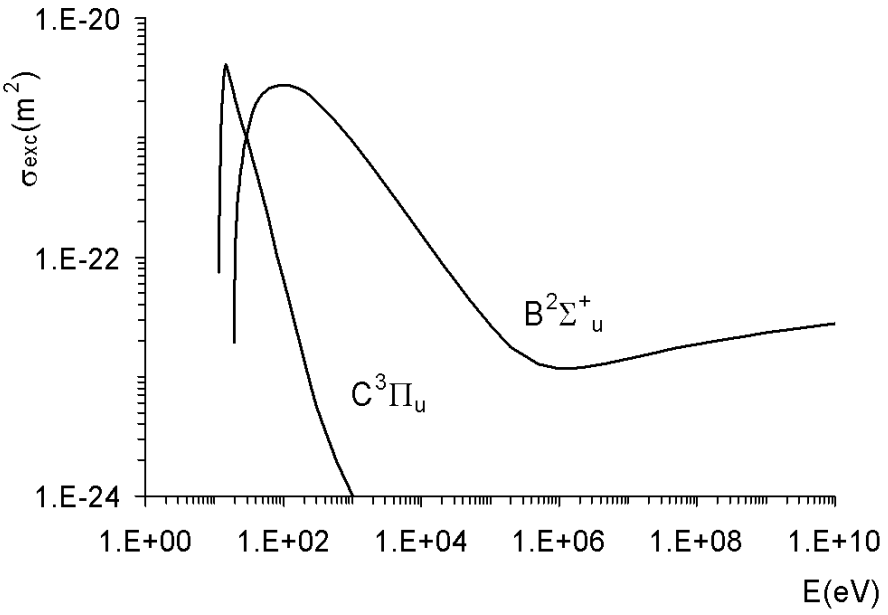

Figure 3.5.: Total cross sections for the excitation of the electronic states $C^3\Pi_u$ and $B^2\Sigma_u^+$ versus electron energy [49].

$A_{\nu\nu'}$ is called the Einstein coefficient, and it is defined as the probability per unit time of radiative de-excitation from state ν to state ν'. From this we can define the relative intensity of any molecular band with respect to a reference transition.

$$\frac{I^0_{\nu\nu'}}{I^0_{00}} = \frac{\sigma_{\nu\nu'}}{\sigma_{00}} = \frac{q_{X\to\nu}}{q_{X\to 0}} \frac{B^{\nu\nu'}}{B^{00}} \tag{3.18}$$

The transition probabilities determine the radiative lifetime τ^r of the excited level, with:

$$\frac{1}{\tau^r} = A_\nu = \Sigma_{\nu'} A_{\nu\nu'} \tag{3.19}$$

The lifetimes and thus the relative intensities are affected by collisional quenching, and this needs to be taken into account when calculating the fluorescence yield. This will be addressed in Chapter 6.

The fluorescence light produced during an EAS can be calculated using:

$$\frac{d^2N_\gamma}{dld\Omega} \simeq \frac{n_{\gamma,0}\,N_e}{4\pi}\left[\frac{photons}{sr\;m}\right], \tag{3.20}$$

where $n_{\gamma,0}$ is the fluorescence yield. The number of particles, N_e comes from the Gaisser Hillas function, and also by integrating the density of particles $\rho_N(X,r)$ around the shower axis , $N_e = \int \rho_N(X,r)\,2\pi r\,dr$.

3.7. Cherenkov Light

When charged particles propagate through a dielectric medium, their local electromagnetic field polarises the atoms in the medium. Once the charged particle has passed the electrons return to their equilibrium state releasing the energy as radiation [52]. For most particle velocities this light destructively interferes. But, if the particle's velocity exceeds some threshold velocity, then the radiation constructively interferes and the radiation forms a shock front, illustrated in figure 3.6. The threshold velocity v_t is equal to the speed of light in a vacuum c, divided by the refractive index n of the medium through which it is propagating.

$$v > v_t = \frac{c}{n} \tag{3.21}$$

This implies a minimum particle energy required to cause a medium to produce Cherenkov radiation. This energy is given by

$$E_{min} = \frac{m_{particle}c^2}{\sqrt{2\,(n-1)}} \tag{3.22}$$

For electrons $m_{particle}\,c^2 = 0.511\,\mathrm{MeV}$ the minimum energy required in air is 21 MeV at sea level. This value is much larger for muons, which require $4.4\,\mathrm{GeV}$[2] [53].

[2]Using n=1.00029 at STP

Unlike fluorescence emission, Cherenkov radiation is not emitted isotropically and is directed about the shower axis. The angle of maximum emission with respect to particle's direction is

$$\theta_{max} = \arccos\left(\frac{1}{\beta n}\right), \tag{3.23}$$

and as $\beta \simeq n \simeq 1$, $\theta \simeq 0°$.

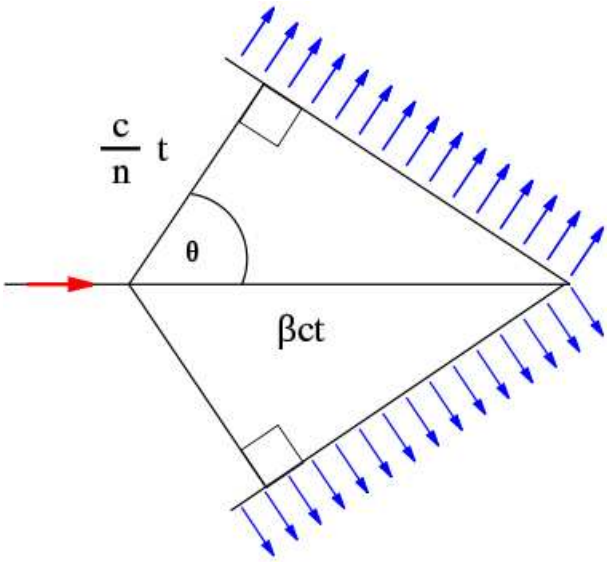

Figure 3.6.: Illustration of the production of Cherenkov light about the particles axis

The reason that Cherenkov light is so intense is that many of the electrons in the shower will have $E > E_{min}$ [54]. The refractive index varies with altitude, so the opening angle of the Cherenkov cone and the yield will also vary with height. Coulomb scattering of electrons broadens the Cherenkov ring. The Cherenkov yield is given by Eq.3.24, in which the number of photons dN_γ, emitted over a length of atmosphere dL, is found by integrating over all sensitive wavelengths.

$$\frac{dN_\gamma}{dL} = 2\pi\alpha\left(1 - \frac{1}{n^2\beta^2}\right)\int \frac{d\lambda}{\lambda^2} \tag{3.24}$$

where N_γ = no. of photons, L = length of traversed atmosphere [m], and α = fine structure constant $\left(\frac{1}{137}\right)$.

The yield's inverse dependence on wavelength means that there is more Cherenkov light

produced in the UV range than the visible range. This is a problem for the analysis of EAS fluorescence light, as the nitrogen fluorescence spectrum also lies in the UV range, and Cherenkov contamination needs to be taken into account during shower reconstruction.

3.8. Detection Techniques

As the flux of cosmic rays around 10^{20}eV is approximately 1 per km^{-2}century^{-1}, extremely large detectors are required that are able to operate over a large number of years. The three dominant techniques that have been used to study cosmic rays at the highest energies are; Surface detectors (SD), Fluorescence detectors (FD) and Cherenkov light detectors. More recently radio antenna arrays are being used.

3.8.1. Surface Array Detectors

The simplest way to study EAS is to build large arrays of particle detectors, to detect the shower particles that reach the ground level. Obtaining the distribution of particles at the ground provides information about the shower at this one depth. To be able to obtain a primary particle energy from this, an absolute energy scale is required. Most ground array based projects are then reliant on air shower simulations to draw conclusions based on their observations. This introduces systematic uncertainties due to the fact that we have to extrapolate from lower energy hadronic interactions in order to simulate showers. Depending on which interaction models are used, the results can be substantially different. Ground arrays have the advantage of a 100 % duty cycle, and thus are capable of high counting statistics at the highest energies.

3.8.2. Fluorescence Detectors

An alternative to using ground arrays is to observe the fluorescence light produced during the propagation of an EAS, as this provides a calorimetric measure of the energy deposited in the atmosphere, which is proportional to the primary energy. This method does still

depend on simulations but not to the extent that ground arrays do. The largest uncertainty associated with this method comes from the fluorescence yield of electrons in air. Unlike the uncertainty involved with the ground array experiments, the fluorescence yield can be measured in laboratories using accelerators. As the critical energy of electrons in air is $\sim$ 84 MeV, these energies are easily obtained. Showers do not deposit all of their energy in the atmosphere as some secondary particles reach the ground level, and some energy is carried away by particles that do not interact in the atmosphere such as neutrinos. The latter is referred to as the invisible energy and is taken into account in the reconstruction process. These corrections are small and are largely independent of hadronic models.

Fluorescence light is emitted isotropically so we can observe showers from many geometries. The number of fluorescence photons dN_γ generated in a layer of atmosphere with thickness dX observed by a fluorescence detector is

$$\frac{dN_\gamma}{dX} = \int \frac{d^2N_\gamma^0}{dX\,d\lambda}\,\tau_{atm}(\lambda, X)\,\varepsilon_{FD}\,d\lambda, \tag{3.25}$$

where $\tau_{atm}(\lambda, X)$ is the transmission losses due to optical absorption and Rayleigh and aerosol scattering by the atmosphere, and ε_{FD} is the efficiency of the fluorescence detector.

3.8.3. Initial Experiments

The first experiment to test the possibility of detecting EAS using fluorescence was built under the direction of K. Greisen in the 1960's, called the "Cornell Wide Angle System". It had three detectors, and each consisted of 5 photomultiplier tubes (PMTs) in a hexagonal arrangement. Four PMTs were positioned with 90° azimuthal separation from each other on a 30° inclination, and the fifth was directed straight up. Due to the poor resolution of the detector it was not possible to successfully detect EAS and it was only operational for 1000 hrs [47]. This was tried again in 1967, this time with 500 PMTs each with a 0.01 sr field of view (fov). Unfortunately, once again the detector was not sensitive enough and was unable to detect an EAS despite running for several years.

It was in 1969 that the first confirmed fluorescence light from an EAS was detected by the INS-Tokyo experiment, with a shower energy greater than 5×10^{18} eV [55].

3.8.3.1. The Fly's Eye experiment

The next stage in the development of Fluorescence Detectors was located at Volcano Ranch near Albuquerque, New Mexico, in 1976. This began with three prototype detectors, each with a 1.8 m diameter mirror and a camera made up of 14 PMTs. It was successful in the detection of fluorescence light [56].

The Fly's Eye experiment which followed had two detector stations 3.3 km apart, called Fly's Eye 1 and Fly's Eye 2. Fly's Eye 1 had 67 spherical mirrors, each with a diameter of 157 cm, that focused light onto cameras made up of 12 to 14 PMTs, making a total of 880 PMTs. Each eye (PMT) observed a different part of the sky. Fly's Eye 2 was smaller with 120 PMT's that spanned 90° in the azimuth and $2° - 38°$ elevation. The two detectors allowed stereoscopic viewing of EAS. The Fly's Eye experiment operated from 1981 to 1993.

3.8.3.2. The HiRes experiment

The HiRes experiment took over where Fly's Eye left off, with HiRes standing for High Resolution Fly's Eye. Once again there were two detector stations, this time they were spaced 12.6 km apart. Each detector had a full 360° azimuthal field of view, and the elevation field of view was $3° - 17°$ for HiRes 1 and $3° - 31°$ for HiRes 2. Their 10 MHz flash ADC allowed them to record pulse height and timing of event triggers in the cameras. The project ran from 1997 to 2007 [57].

3.8.3.3. Telescope Array

This current project is located in the desert in Utah, USA, 140 miles from Salt Lake City [58]. It consists of a 760 km^2 array of 576, 3 m^2 scintillation counters and 3 air fluorescence sites on the perimeter of the array. Each site has 12−14 telescopes, $3° - 33°$ field of view in elevation and 108° in azimuthal. Data taking began in the spring of 2007 [59], and the primary purpose of the project is to measure the cosmic ray spectrum at GZK energies. Its features include; hybrid measurements of EAS down to $10^{17.5}$ eV, calibration

of the fluorescence detectors using an electron linac, and the hadronic interaction model calibrated by the Large Hadron Collider (LHC).

3.8.3.4. ASHRA

ASHRA stands for All-sky Survey High Resolution Air Shower telescope. It is a proposed project to be located in Hawaii, consisting of two detectors set $30-40\,\mathrm{km}$ apart, that simultaneously detect fluorescence and Cherenkov light. The detectors will each have 12 telescopes that will view the whole sky with 1 arcmin resolution [60].

3.8.3.5. JEM-EUSO

The Extreme Universe Space Observatory, accommodated on the Japanese Experiment Module of the International Space Station, JEM-EUSO will detect extreme energy cosmic rays (EECR) [61]. It will do this by observing the fluorescence and Cherenkov photons produced by cosmic ray interactions with the atmosphere. Orbiting the Earth at a height of roughly $400\,\mathrm{km}$ every 90 minutes, it will have a field of view of 60° corresponding to an observation area on the Earth's surface greater than $1.9\times10^5\,\mathrm{km}^2$. It's main objectives are to detect particles with energies greater than $10^{20}\,\mathrm{eV}$, to identify sources by high-statistics arrival direction analysis, and to measure the energy spectra from individual sources to constrain acceleration or emission mechanisms. It's large exposure area will allow it to collect much larger statistics at the highest energies than any of the past or present experiments. The expected cumulative exposure of JEM-EUSO with other experiments for comparison is shown if figure 3.7.

The JEM-EUSO instrument consists of a near-UV range telescope, atmospheric monitoring device and a calibration system. It is hoped to be operational in mid 2010s.

3.8.4. Radio Detectors

Radio waves are emitted during the propagation of the electromagnetic component of EAS in the magnetic field of the Earth. This method becomes effective above $E > 10^{16}\,\mathrm{eV}$. The

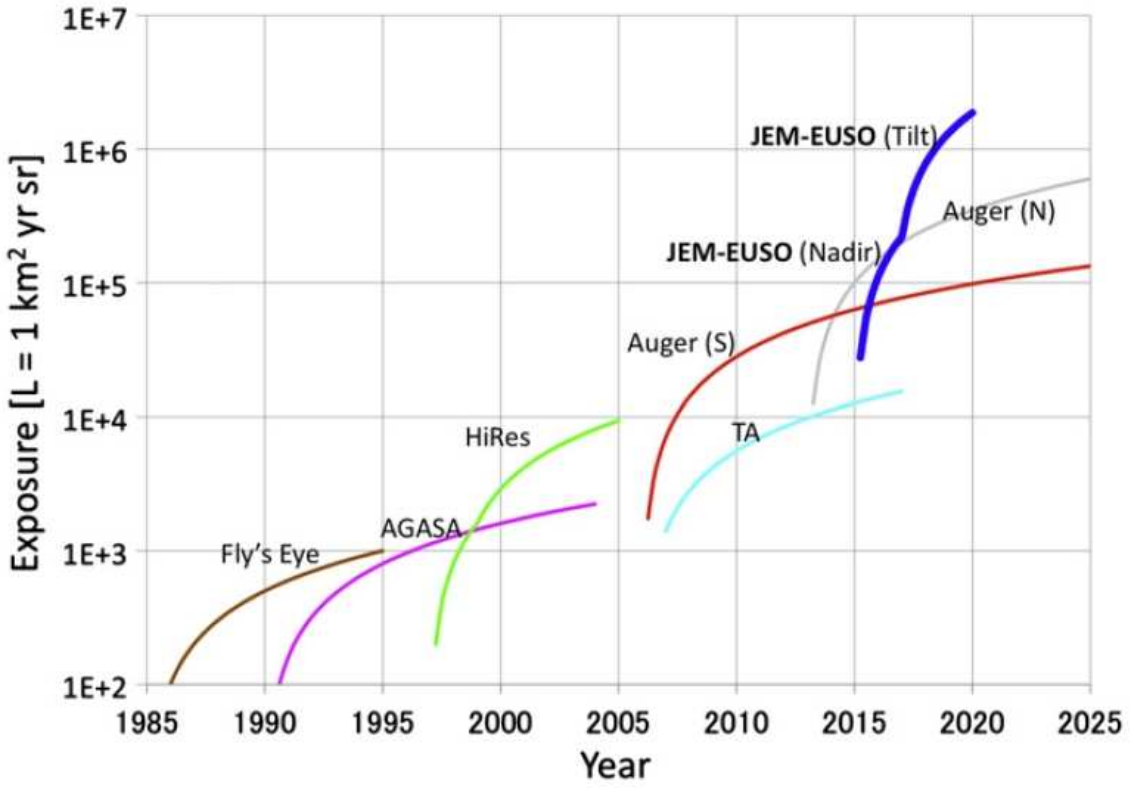

Figure 3.7.: Expected cumulative exposure of JEM-EUSO in Linsley units (1 Linsley= 1 km^2 sr yr). Evolution of exposure by other retired and running EECR observatories are also shown for comparison. Figure from [61]

technique was first proposed in 1965, when radio signals at 44 MHz were observed [62]. Recently with advancements in analogue to digital converters and computers, routine radio detection of EAS is now possible.

4. Pierre Auger Observatory

The Pierre Auger Observatory is located at the foot of the Andes in Argentina (at 1400 m above sea level), near the town of Malargue. It is a hybrid detector of extensive air showers, able to simultaneously detect EAS using a surface detector array and fluorescence detectors. This allows a more accurate and precise geometric and energy reconstruction than ever before, reducing the uncertainty in determining energy spectra, mass composition and arrival directions of cosmic rays at the highest energies. The SD is comprised of over 1600 water Cherenkov tanks covering an area of 3000 km^2 which allows for large statistics, and the FD system is comprised of 4 detector sites bordering the SD array. On-site atmospheric monitoring is performed using several instruments to aid in the reconstruction of the EAS. Additions have been made to the observatory to lower the energy threshold of the fluorescence detection and to study the muon content of showers. This chapter will discuss the SD and FD as well as the recent upgrades, and the atmospheric monitoring system.

4.1. Surface Detector System

Over 1600 water-filled Cherenkov tanks comprise the surface detector array of the observatory. Figure 4.1 shows the positions of the detectors, which are located on a triangular grid with spacing of 1500 m. The black dots contained within the green shading are the operational tanks. There are only a few small gaps in the array due to large amounts

Figure 4.1.: A map of the Pierre Auger Observatory in Argentina. Each water Cherenkov tank is represented by a black dot. The array is surrounded by the four fluorescence stations as shown. The fields of view of the 24 telescopes are indicated by the blue lines.

of surface water or land owner disputes. The spacing of the tanks was chosen as a compromise between cost and energy threshold, as the spacing had to be small enough such that the energy threshold overlapped with existing data. Each surface detector unit is a cylindrical tank that operates as an autonomous detector and is equipped with a solar panel and battery for power, a GPS unit for position and timing information, and a radio transceiver for communication. The detectors each have a surface area of $10\,\mathrm{m}^2$ and are $1.55\,\mathrm{m}$ in height (water height is $1.2\,\mathrm{m}$), containing 12000 litres of ultra-pure water with a high resistivity of approximately $15\,\mathrm{M\Omega\,m}$. The height of the water in the tanks was chosen to obtain a clear muon signal in the tank and optimise the separation between muon and electromagnetic signal components [63]. The $1.2\,\mathrm{m}$ depth of the water is sufficient to

absorb 85 % of shower energy carried by the electromagnetic component that is incident on the tanks at distances greater than 100 m from the core. The purity of the water is very important as its condition needs to remain constant over time for accurate analysis of the Cherenkov radiation produced in the water. With the current protection from contamination, the water is predicted to retain its purity over a twenty year period [64]. Tanks are opaque to all visible and UV light due to a 1 % carbon black pigmentation, but have an outer layer of beige pigment to reduce heating of the tanks on high temperature days. The tanks must be capable of surviving a range of environmental conditions such as; -15° to 50°C temperatures, winds of up to 160 $\mathrm{km\,h^{-1}}$, hail, snow, dust, rain and flooding. They must also be placed on level ground to prevent deformation of the tanks.

When the charged particles from the EAS pass through the water, Cherenkov light is produced. The inner lining of the tanks is highly reflective of this Cherenkov light. Three photomultiplier tubes view the water in the tank from above through two types of windows in the top liner, hard polycarbonate or soft (clear) polyethylene. Each PMT collects greater than 90 photo−electrons for each vertical equivalent muon (VEM) [64]. Data collected in the tanks are transferred automatically via wireless communication. The surface detectors boast a 100 % duty cycle as they can be operated both day and night, and independently of atmospheric conditions.

4.1.1. Surface Detector Energy Calibration

Surface detector event reconstruction is based on the time sequence and signal levels in tanks that are part of T1, T2 or T3 triggers [65]. T1 and T2 triggers involve triggers within individual tanks, whereas T3 triggers relate signals from several neighbouring tanks. A plane front is fitted to the trigger timing information from the tanks, and this plane defines the zenith and azimuth angles of the shower. Once the position of the shower core is found, a LDF can be fitted to the signals from the tanks. This function describes the shower particle density as a function of distance to the shower core at the ground level. However, deducing a primary energy from the density map is highly model dependent. In practice what is done is that the signal at 1000 m from the location of the reconstructed shower core is used as an indicator of shower energy. Figure 4.3 shows the signal in VEM recorded in several tanks plotted against their distance from the shower core. This is then fitted with

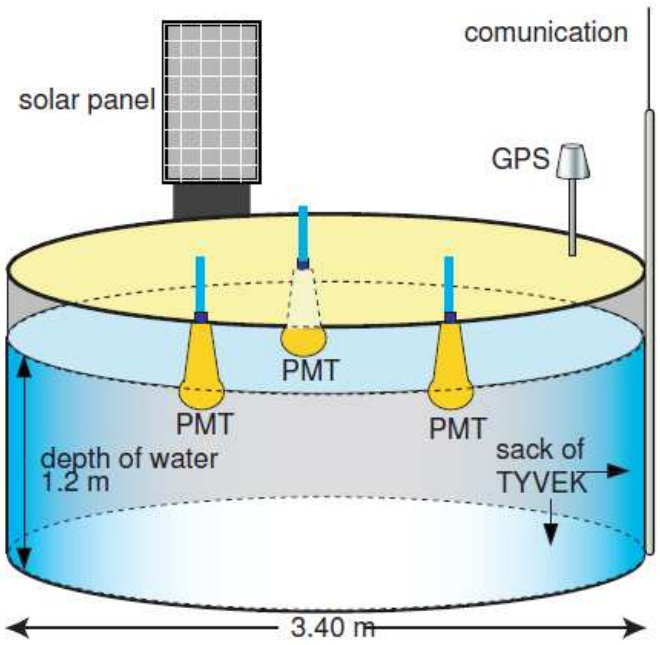

Figure 4.2.: Schematic view of a surface detector unit. The tank is equipped with a solar panel, battery, GPS unit and a radio transceiver.

the LDF, from which the signal at 1000 m from the shower core, denoted as S(1000), can be determined. Any uncertainty in the location of the shower core adds to the uncertainty in the value of S(1000), but does not introduce any systematic shifts. Studies have shown that S(1000) is insensitive to primary composition for zenith angles less than 60°[66]. The independence of the shower signal to primary composition extends to distances than larger than 1000 m from the core, but the relative statistical uncertainty increases as the signals get smaller.

Shower to shower fluctuations can account for up to 10 % of the energy uncertainty, and the choice of lateral distribution function (LDF) can contribute approximately 4 %. The value of S(1000) is dependent on the zenith angle for a given shower energy, as it will be affected by the shower's attenuation in the atmosphere, due to the fact that inclined showers traverse a larger atmospheric mass than vertical showers. Above 3×10^{18} eV the Auger detection efficiency is 100 % for zenith angles less than 60° [66]. This means that above this energy, we can say that the differences in S(1000) at different zenith angles is

Figure 4.3.: Lateral distribution: filled circles represent recorded signals. The fitted value S(1000) is marked with a cross. Figure from [67].

due solely to attenuation. This allows us to use a method called the constant intensity cut (CIC) which is used to evaluate the effect of attenuation. The zenith angle dependent attenuation is fitted with the curve $A(\theta) = 1 + ax + bx^2$ where $x = cos^2\theta - cos^2 38°$. The parameter x involves the zenith angle of $\theta = 38°$ as this is the median of the zenith angle distribution of events [65]. Using $A(\theta)$, we can calculate the value $S_{38°} = S(1000)/A(\theta)$, for showers with energy above 3×10^{18} eV and $\theta < 60°$. This gives us an energy estimate from the ground array that has been corrected for attenuation. To determine the absolute energy scale, we can utilise the hybrid nature of the Auger detectors, and use energy measurements based on the fluorescence technique.

The fluorescence detectors obtain a nearly calorimetric measurement of a shower's energy. The recorded signals can be converted to the energy deposited in the atmosphere per unit depth by using information about the fluorescence yield and the fraction of invisible energy, as well as the detector's calibration. The invisible energy fraction is the fraction of the primary energy that is not deposited in the atmosphere, and hence not observed by the fluorescence detector. It is determined from hadronic interaction models, and hence

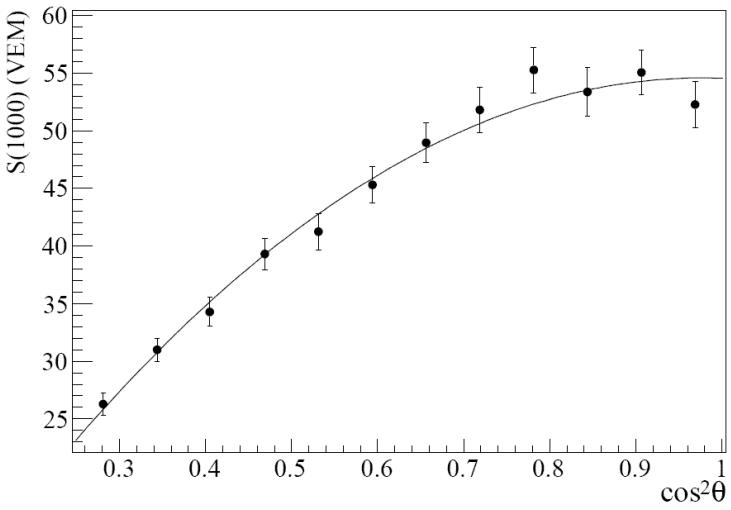

Figure 4.4.: Derived attenuation curve, CIC(θ), fitted with a quadratic function.

introduces a systematic uncertainty to the energy reconstruction. This is estimated to be less than 5 %. The largest uncertainty in the energy reconstruction is the uncertainty in the absolute fluorescence yield, roughly 14 %, compared to the total systematic uncertainty of 22 %. A complete list of systematic uncertainties is presented in section 5.1.4. Using data from events that were detected by both the SD and the FD (hybrid events), we can calibrate the SD's measurement of S_{38° with the FD energy.

A subset of high quality hybrid events from the time period January 2004 to December 2008 was used to calibrate the SD in the latest calibration study, as presented at the 2009 International Cosmic Ray Conference (ICRC). All six nearest neighbours of the SD station that recorded the highest signal were required to be active to ensure that the core was within the array, and the station with the highest signal was required to be within 750 m of the reconstructed shower core. Also the vertical aerosol optical depth, VAOD (h), was required to have been measured using laser shots observed by the FD within the same hour as the event was observed. Other quality conditions that the events were required to meet are:

- χ^2 of Gaisser Hillas (GH) fit to the longitudinal profile attained with the FD < 2.5.
- χ^2 of linear fit $> 4\chi^2$ of GH fit.

- X_{max} is within the field of view.
- Relative uncertainty of energy reconstruction $< 20\,\%$.
- Uncertainty in $X_{max} < 20\,\mathrm{g\,cm^{-2}}$.
- Cherenkov contamination $< 50\,\%$.

The 795 hybrid events which satisfied the criteria listed above and the pairs of energy measurements from the FD (E_{FD}) and the corresponding value of S_{38} measured by the SD are presented on a log-log plot in figure 4.5. The data are fitted with a power law $log(E_{FD}) = a\, log(S_{38})^b$, with fit parameters $a = 1.51 \pm 0.06\,(stat) \pm 0.12\,(syst)$ and $b = 1.07 \pm 0.01\,(stat) \pm 0.04\,(syst)$. The reduced chi-squared of the fit is 1.01. This shows us that S_{38} grows approximately linearly with energy, and the root mean square deviation is $17\,\%$, as shown on the right in figure 4.5. Due to a lack of events at the highest energies the calibration range is limited. The most energetic event used to calibrate the SD has an energy of $E = 6 \times 10^{19}\,\mathrm{eV}$.

NOTE:
This figure is included on page 49 of the print copy of the thesis held in the University of Adelaide Library.

Figure 4.5.: Left: Correlation between $\lg(S_{38})$ and $\lg(E_{FD})$ for the 795 hybrid events used in the fit. The line represents the best fit. Right: Fractional difference between the calorimetric energy, E_{FD}, and the energy estimate of the surface detector, E, obtained by the calibration curve, for the 795 selected events. The results are a mean of 0.02 ± 0.01 and a RMS of 0.17 ± 0.01 [67].

4.2. Fluorescence Detector System

The details provided here can be found in a recent paper published by the Auger Collaboration [68].

The SD array is surrounded by four stations of fluorescence telescopes, referred to as eyes, and they are named Los Leones, Coihueco, Los Morados and Loma Amarilla. Each of the four eyes contains six telescopes each of which has a field of view of 30° in azimuth and 28.6° in elevation, giving each eye a total azimuthal field of view of 180°. The telescopes are based on Schmidt optics, and they are enclosed in buildings to protect them from the environment. The elements that compose the optical system are: a filter at the entrance window, aperture, corrector ring, mirror and camera. The filter is a window made of Schott MUG−6 glass [69]. The spectral characteristics of the glass make it optimal for transmitting nitrogen fluorescence in the wavelength range 290−410 nm, in which the majority of the emission lies, while blocking out a significant amount of the night sky background light. It also acts to protect the telescope from outside temperature variations, as these can affect the gain of the camera.

The aperture, corrector ring, mirror and the camera comprise the Schmidt camera. The corrector ring assures that the spot size due to spherical aberration is less than 15 mm in diameter, corresponding to 0.5°. The spot refers to the image of the point source at infinity on the focal surface of the optical system, which is more commonly called the point spread function. The aberration due to achromatism is negligible at 0.65 mm. The mirrors are 3.6 m × 3.6 m and have a radius of curvature of 3.4 m. They are built in 60 hexagonal segments at eyes Coihueco and Loma Amarilla, and 36 square segments at Los Leones and Los Morados. The hexagonal segments are made of glass, and are covered by a aluminium reflecting layer and a SiO_2 coating, and the square segments are aluminium with an anodised reflective surface.

Each camera is an array of 440 hexagonal photomultiplier tubes, model XP3062 manufactured by Photonis [70], in a 22×20 pixel configuration located at the focal surface of the mirror. Each pixel has a field of view of 1.5° in diameter. In the spaces between the PMTs, reflectors covered with aluminised mylar, called Mercedes stars, are used to reflect photons into the PMTs that would have otherwise gone undetected.

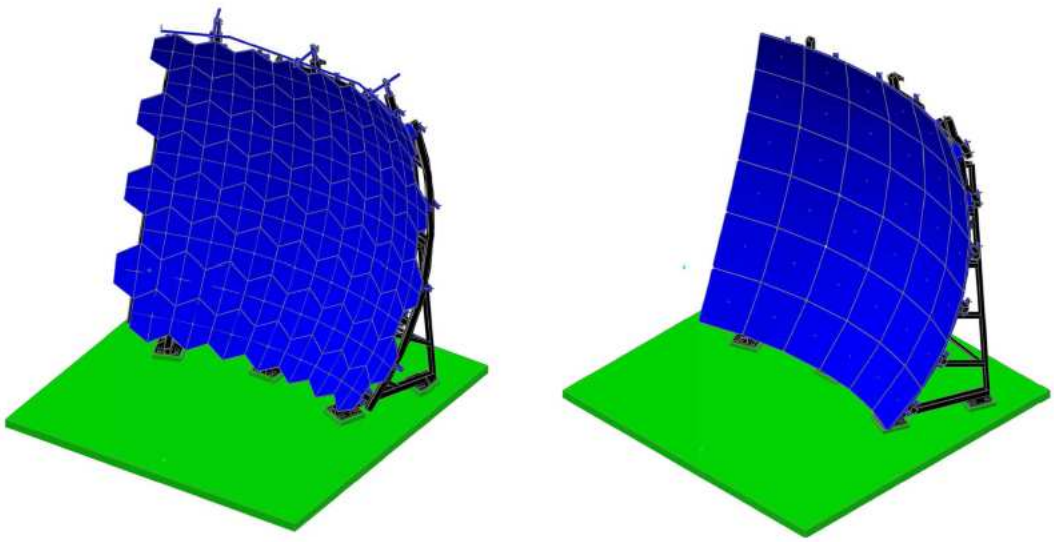

Figure 4.6.: The two segmentation configurations of the FD mirrors. Left: 60 hexagonal glass mirror segments. Right: 36 rectangular mirror segments [68].

The electronics system has a large dynamic range of 15 bits and a 10 MHz ADC sampling rate. It provides good quality pulse timing and amplitude information, adequate for recording the air shower's development. Each pixel has a readout channel with a specific gain, that is called the normal channel. Additionally, each group of 11 pixels forming a column in the camera, is read out by a second virtual channel with a lower gain, enlarging the camera's total dynamic range. The fluorescence detectors can only operate on clear nights in the absence of a full moon. This results in a duty cycle of roughly 12 %. Within this time the Pierre Auger Observatory is operated in hybrid mode, simultaneously recording EAS with the FDs and the SD.

4.2.1. Fluorescence Detector Calibration

Calibration of the fluorescence detectors is required to determine a measurement of shower energy. A relative calibration is done on a nightly basis, before each night's run is begun, and an absolute calibration is also performed on a less frequent basis with a light source of known intensity and wavelength.

4.2.1.1. Absolute Calibration

The purpose of the absolute calibration is to provide a conversion between the digitised signal recorded and the photon flux that is incident on the telescope aperture. It is intended to be done a few times each year for each of the 24 telescopes. This is also referred to as the drum calibration, as a light source is placed inside a cylindrical drum of diameter 2.5 m and a depth of 1.4 m which reflects the light from the source and creates an even and isotropic illumination of the entire telescope aperture. The cylinder is made of a laminated honeycomb core covered with aluminium. Inside it is lined with Tyvek, diffusely reflecting in the UV, and its aperture is covered by a thin Teflon sheet. Initially the light source used was a pair of high powered LEDs with $\lambda = 375 \pm 12$ nm. These were later replaced by a xenon flasher mounted on the back of the drum. With the xenon flasher it is possible to calibrate at 320, 337, 355, 380 and 405 nm wavelengths.

As the drum is mounted outside the filter, an end-to-end calibration is obtained. This includes the cumulative effect of optical filter transmittance, reflection at optical surfaces, mirror reflectivity, pixel light collection efficiency, pixel light collection area, cathode quantum efficiency, PMT gain, pre-amp and amplifier gains and digital conversion. The total systematic uncertainty in the calibration constants is 9.5 %.

4.2.1.2. Relative Calibration

For the relative calibration three xenon flash lamps are used. They are connected to optical fibres that direct the light to three different positions at the telescope allowing for three different relative calibration modes. The optical fibre for calibration mode A ends in the middle of the mirror in a gap between the mirror segments, directly illuminating the camera. For calibration mode B two fibres are attached to the vertical edges of the camera, directed to the mirror. All these fibres are terminated with a 1 mm Teflon diffuser to provide a diffuse light output. The light for calibration mode C is directed to two reflective Tyvek targets mounted at the telescope shutters outside the aperture and reflected from there back into the telescope. Relative calibration runs are performed before and after each night on which measurements are taken, monitoring the time variation of the calibration. Presently, the results of calibration A are used to correct the absolute

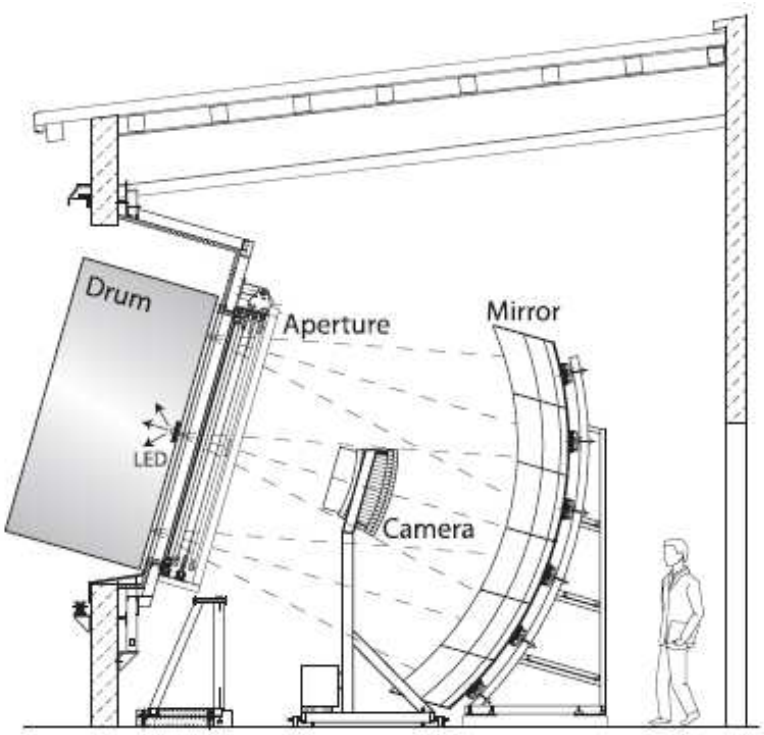

Figure 4.7.: Schematic of the Fluorescence Detector with the drum attached to the aperture [68].

calibration constants for seasonal and night-to-night fluctuations. Consequently, there is a calibration constant for each pixel each night that can be used in the data analysis

4.3. Auger South Enhancements

The southern observatory is being upgraded to lower the energy threshold of one of the fluorescence detectors and the ground array in front of that FD. The enhancements include three high elevation telescopes, and a nested surface detector array with buried muon detectors. Figure 4.8 shows the energy range that the enhancements will cover. The current energy threshold of the surface detector is 3×10^{18} eV. The enhancements will allow for the evolution of the energy spectrum to be studied over the second knee through to the ankle (see section 5.1). The extensions will allow an overlap between Auger and

KASCADE Grande [71], which will help to validate any results.

The second knee, located at approximately 4×10^{17} eV, has been observed by Akeno, Fly's Eye stereo, Yakutsk, and HiRes, but the interpretation of this feature is still uncertain. The current dominant theories are that it is either the end of the Galactic component, or the result of proton interactions with the CMBR as described in Chapter 2. The ankle has been detected by Fly's Eye and Haverah Park, and they agree that the ankle exists at approximately 3×10^{18} eV. This has also been confirmed by Yakutsk, HiRes and Auger's hybrid spectrum. AGASA also observed a similar feature in the energy spectrum although it located it at 10^{19} eV. There are several interpretations of the ankle, that will depend on the interpretation of the second knee. These are the transition point between the galactic and extra−galactic components, or from the result of pair creation by protons in the CMBR [72].

As shown in chapter 2, power law spectra from cosmic ray sources with different composition can have spectra at the highest energies that are very similar, but can be distinguished around the ankle region [72]. For a purely proton composition, the ankle will be due solely to photo−pion production of electron / positron pairs through interactions with the CMBR. This would then attribute the second knee to the galactic / extra-galactic transition. On the other hand, if the source composition is heavy, then the ankle would be the energy of the galactic/extra-galactic transition, and the composition would be a strong function of energy in this interval [72].

4.3.1. HEAT

HEAT is an acronym for High Elevation Auger Telescopes [73]. These are three fluorescence telescopes that have been added to the fluorescence detector site at Coiheuco, and they have a field of view covering 30° to 60° elevation. The idea is to use these High Elevation Auger Telescopes in combination with the current telescopes at the FD site, in hybrid mode with the shower particle data from AMIGA, the infill array located in front of Coihueco. The strength of the fluorescence signal is proportional to shower energy, and thus at large distances low energy showers cannot be observed and they need to be close to the detectors to trigger them. The closer a shower lands to a detector, the lower the

Figure 4.8.: The cosmic ray energy spectrum as measured by a range of experiments. The energy ranges covered by the Auger South baseline (BL) design, and the added enhancements AMIGA and HEAT are shown [72].

maximum height observed within the field of view will be, illustrated in figure 4.9. This is a problem when viewing low energy showers, as on average they maximise higher in the atmosphere than high energy showers.

4.3.2. AMIGA

The Auger Muons and Infill for the Ground Array, AMIGA, will be made up of 85 pairs of water Cherenkov detectors and muon scintillation counters buried 3 metres underground. The spacing of the pairs will be 433 m and 750 m, compared to the standard array spacing of 1500 m. The infills will cover areas of 5.9 km^2 and 23.5 km^2 respectively, and they will be overlooked by HEAT, shown in figure 4.10. One of the main uncertainties in the surface

Figure 4.9.: Illustration showing detector bias to showers coming towards the detector[73].

detector reconstruction process is the uncertainty in the air shower muon component of simulated showers. Large muon detectors will aid in reducing this error by directly measuring the muon content of extensive air showers.

4.3.3. AERA

The Auger Engineering Radio Array (AERA) adds a third detection technique to the hybrid detector. Radio emission from every stage of an EAS can be detected by the array at the ground level, giving another method of studying the evolution of EAS. The array will cover an area of 20 km^2 with up to 150 stations and, like the ground array, it boasts a 100 % duty cycle.

4.4. Auger North

The Pierre Auger Collaboration is committed to conducting a full sky study of cosmic rays at the highest energies. The southern hemisphere site was completed in June 2008, and now work has begun on designing a prototype of a northern hemisphere observatory

Figure 4.10.: This image shows the layout of the enhancements with respect to the current array. The white radial lines from the FD Coihueco illustrate the current telescope fields of view, and the black lines show the fields of view of the high elevation telescopes. The grey and white dots represent the 433 m and 750 m detector spacings respectively and the black dots are the positions of the current detectors [74].

in Colorado, USA. All images displayed in this section as well as all quoted figures were taken from [75].

4.4.1. Physics Motivation and Potential

The results obtained to date from the data taken with the southern observatory have led to many scientific breakthroughs in the field. One such breakthrough was the detection of anisotropy above 60 EeV. This means that the detection of point sources will be possible with these trans−GZK events (E>60 EeV). The southern site records roughly 25 of these per year with the SD, although only two with their longitudinal profile also observed by

the fluorescence detectors. This is not sufficient for identifying sources and studying high energy interactions.

The goals for the northern observatory are

- Determine which classes of astrophysics produce trans-GZK particles
- Measure the energy spectra of individual sources. Determine the acceleration mechanism capable of producing such a spectrum
- Determine the primary particle types of trans-GZK cosmic rays, and calculate the expected neutrino and photon flux from interactions of the cosmic rays with background radiation fields.
- Measure diffuse neutrino flux at EeV energies and search for emission from identified cosmic ray sources.
- Measure diffuse photon flux at EeV energies and search for emission from identified cosmic ray sources.
- If the cosmic rays are protons: Determine the properties of hadronic interactions in the centre of mass energy range $250-400\,\mathrm{TeV}$. By measuring the cross-sections, constraints can be put on the elasticity and multiplicity.
- If the cosmic rays are heavy nuclei: Probe quark-gluon plasma produced in nucleus-nucleus collisions at centre of mass energies $30-60\,\mathrm{TeV}$.
- Use the deflections of trans-GZK charged particles to study the galactic and intergalactic magnetic fields.

One of the challenges is the fact that all of these goals are strongly interrelated. The Auger north array will be optimised to achieve higher statistics above $60\,\mathrm{EeV}$, compared to the southern array. At these energies, a correlation between the arrival directions and positions of local AGN is strongest for a 3.1° deflection, which suggests a proton composition. But the mean depth of shower maximum, and the average fluctuation in this depth, suggests a heavy composition such as iron. The Auger north detector will extend measurements of X_{max} up to $100\,\mathrm{EeV}$ with good statistics.

4.4.2. Site Configuration

Auger north will utilise the detector components that have been well tested and studied at Auger south. The site is located in the south-east corner of Colorado and covers an area of 20,000 square kilometres that may be extended further east into Kansas. The surface detector array will be made up of 4,400 water Cherenkov tanks, set on a 1 mile rectangular grid. The tanks will be placed on every second corner of this rectangular grid, with 10 % of the array having a tank on every corner which will act as an infill array, as illustrated in figure 4.12. From simulations it has been found that such a surface array reaches 50 % efficiency at 8-10 EeV and 100 % efficiency at 80 EeV, with the infill array being fully efficient at 10 EeV.

Table 4.1.: Comparison of the southern and proposed northern Pierre Auger sites. The energy ranges for the efficiency refer to iron and proton primaries respectively.

	Auger South	Auger North
Location	$35°S$, $69°W$	$38°N$, $30°W$
Altitude	1,300−1,500 m	1,300 m
Number of SD tanks	1600	4000
SD tanks spacing	1500 m	2300 m
PMT sensors per SD	3	1
Communications Network	SD−tower radio	peer−to−peer
SD array 50% efficiency	0.7−1.0 EeV	8−10 EeV
SD array 100% efficiency	3 EeV	80 EeV
FD Stations	4	5
FD telescopes	24 (4x6)	39 ((2x12) + (2x6) + 3)
Began Construction	1999	proposed 2011
End Construction	2008	proposed 2016

Figure 4.11.: Illustration of the proposed Auger North site.

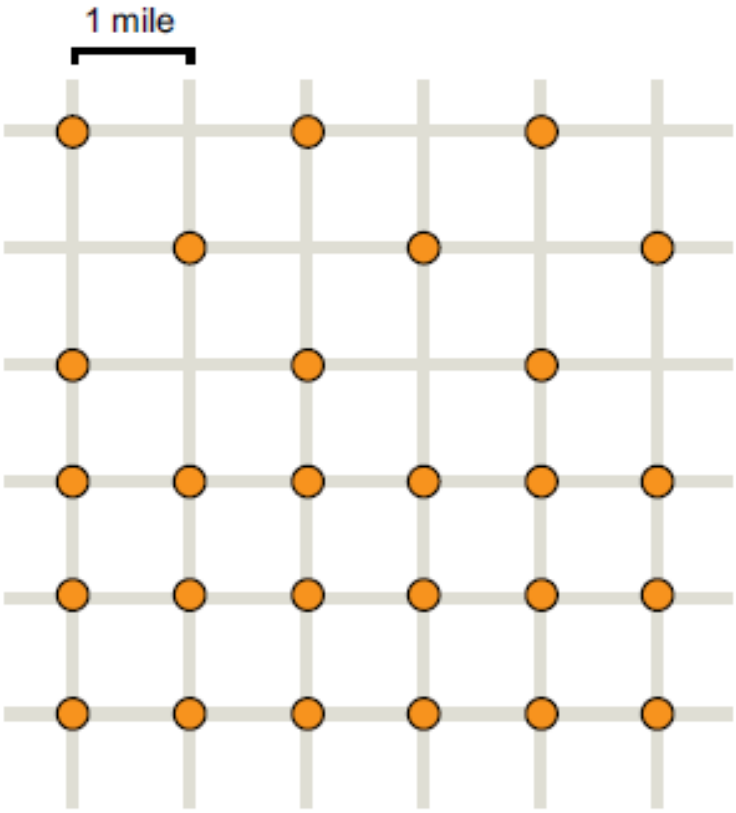

Figure 4.12.: Surface Detector grid configuration for Auger North. The top three rows of tanks show the standard configuration and the bottom three rows illustrate the infill configuration.

5. Results from the Pierre Auger Observatory

In this chapter recent results from the Pierre Auger Collaboration are presented. These were released at the 2009 ICRC. The energy spectra obtained from the surface detector events and from hybrid events are compared. Mass composition including photon and neutrino upper limits are shown, as well as the latest anisotropy results. I conclude by discussing the current systematic uncertainties that exist in the energy reconstruction.

5.1. Energy Spectra

The following results have recently been published in Physics Letters B, and can be found in more detail in [76].

Energy spectra can be created using either events solely from the surface array or from hybrid events. While the SD spectrum has much higher statistics than the hybrid, it doesn't extend down as far as the hybrid spectrum in energy. Here the two spectra are presented along with a combined spectrum which joins the two to cover a wider energy range.

5.1.1. Surface detector spectrum

As the surface detector has a 100 % duty cycle, high statistics can be obtained. This allows features in the energy spectrum to be observed at the highest energies with unprecedented precision. The SD energies come from a calibration with the energy measured by the fluorescence detectors (as discussed in Chapter 4). The energy spectrum obtained with the SD array extends down to 3×10^{18} eV, shown in figure 5.1. The systematic uncertainty in the energy calibration is 7 % at 10^{19} eV and 15 % above 10^{20} eV [67]. The energy resolution of the SD is approximately 20 %. For the data shown here, taken from the time period January 2004 to December 2008, the exposure is 12,790 $\mathrm{km^2 sr\,yr}$. The exposure is determined with an uncertainty of only 3 % [77] by monitoring the status of each tank in the array at each second.

Figure 5.1.: Energy spectrum derived from surface detector data calibrated with fluorescence measurements. Only statistical uncertainties are shown [78].

5.1.2. Hybrid spectrum

The hybrid energy spectrum is shown in figure 5.2. These energy measures are taken independently of the SD spectrum, as they come from the fluorescence detector's measurement of the energy deposited in the atmosphere, and information from the SD array is used in the geometrical reconstruction only. This spectrum extends down to $\sim 10^{18}$ eV as the fluorescence detectors have a lower energy threshold than the SD but, as can be seen by the number of events in each bin, the statistics are much poorer due to the limited duty cycle of the fluorescence detectors. Events are only chosen for determination of the spectrum if they meet specific selection criteria that ensure an energy resolution of better than 6 % over the entire energy range.

The hybrid exposure is calculated using a Monte Carlo simulation that reproduces actual data−taking conditions including their time variability [79]. Detailed data−taking efficiencies are obtained from extensive monitoring of all components of the fluorescence detectors [80]. The simulation also takes atmospheric conditions into account, and only considers times when the light attenuation due to aerosols has been measured, and when there is no cloud cover over the array [81]. The exposure is nearly independent[1] of hadronic interaction models but a systematic uncertainty exists due to the unknown primary mass composition as a function of energy. This uncertainty has a magnitude of 8 % at 10^{18} eV and is negligible above 10^{19} eV. The systematic uncertainty in the hybrid exposure is 10 % at 10^{18} eV and 6 % above 10^{19} eV.

5.1.3. Combined spectrum

A combined spectrum can be made by joining the hybrid and the SD spectrum to make one energy spectrum that covers energies from 10^{18} eV to 10^{20} eV. The benefit of this is that we can combine the high statistics of the SD and the extension to lower energies to measure both the ankle and the flux suppression with unprecedented statistics. They are combined using a maximum likelihood method which takes into account both systematic and statistical uncertainties of both spectra. As the SD data are calibrated using the hybrid events, both spectra have the same systematic uncertainty in their energy assignment.

[1] The dependence of the exposure on the chosen hadronic model was found to be less than 2%.

Figure 5.2.: Energy spectrum derived from hybrid data. Only statistical error bars are shown [78].

The combined energy spectrum is compared to a spectrum of the form $E^{-2.6}$, along with data from HiRes, in figure 5.3. Here we can see an abrupt change in the spectral index at 4 EeV (the ankle), and a gradual suppression beyond 30 EeV. A modest systematic shift in either the HiRes or the Auger spectrum, within the uncertainties of either spectrum, would account for the difference between them. The energy spectrum observed by the Pierre Auger project can be described by a broken power-law of index 3.3 below the ankle (at $\log_{10}(E_{ankle}/eV) = 18.6$). Above the ankle the spectrum is described by a power-law of index 2.6 and a flux suppression of a factor of two at $\log_{10}(E_{1/2}/eV) = 19.6$.

5.1.4. Systematic Uncertainties

As the SD data are calibrated using hybrid events, both spectra have the same systematic uncertainty for the energy assignment of 22 %. The main uncertainties come from the absolute fluorescence yield (14 %), uncertainties associated with the reconstruction method

Figure 5.3.: The fractional difference between the combined energy spectrum of the PAO and a spectrum of the form $E^{-2.6}$. Data from the HiRes instrument [82, 83], are shown for comparison [78].

(10 %), and the absolute calibration of the fluorescence photo-detectors (9.5 %). A more complete list of contributors to the overall uncertainty are listed in table 5.1. This thesis addresses some of these uncertainties, in an attempt to understand them further, and attempts to reduce them.

5.2. Composition Studies

The latest composition studies have recently been published in Physical Review Letters and Astroparticle Physics [84, 85, 86].

As discussed in Chapter 3, the mean value of the depth of shower maximum $\langle X_{max} \rangle$ is

related to the mean logarithmic mass $\langle lnA \rangle$ by

$$\langle lnA \rangle = \frac{X_{max} - X_{max}^{Fe}}{X_{max}^{p} - X_{max}^{Fe}} \tag{5.1}$$

where X_{max} is the measured value and X_{max}^{p} and X_{max}^{Fe} are the values obtained from simulation for pure proton and iron composition respectively. The width of the distribution is also a composition dependent parameter, independent from the mean, with heavy nuclei exhibiting smaller shower-to-shower fluctuations than protons. Both $\langle X_{max} \rangle$ and the measured RMS are plotted as a function of energy in figure 5.4, and they were obtained from Gaisser−Hillas functions being fitted to fluorescence data. Also plotted are the predicted X_{max} values for pure proton and pure iron compositions for different hadronic interaction models. Both the mean and RMS of the depth of shower maximum at the highest energies indicate a heavy composition. It is important to note that this change in composition is based on the best existing models for hadronic interactions at the highest energies. If the physics of hadronic interactions changes a lot at these energies then this conclusion may be incorrect. The mean X_{max} is fitted with two lines, breaking at approximately the energy of the ankle. This break suggests a change in composition, which may be due to the extragalactic component becoming dominant beyond this energy.

Table 5.1.: Systematic uncertainties in the energy measurement of hybrid events.

Source	Magnitude %
Absolute Fluorescence Yield	14
Hybrid Reconstruction Method	10
Absolute Calibration of fluorescence photo-detectors	9.5
Water vapour quenching	5
Invisible energy correction	4
Wavelength dependent response of FD	3
Molecular Optical Depth	1
Multiple Scattering Models	1

Figure 5.4.: Left: Mean depth of shower maximum as a function of shower energy. Right: Mean RMS of depth of shower maximum as a function of energy. Both figures have predicted values for these quantities from a range of different hadronic interaction models [84].

5.2.1. Neutrino and Photon Limits

So far no ultra-high energy neutrinos have been detected, despite many experiments dedicated solely to their detection. In Auger, neutrino candidates are searched for as horizontal air showers to discriminate against the dominating hadronic background. The Pierre Auger Observatory is sensitive only to Earth-skimming tau neutrinos. Tau leptons from tau neutrino interactions emerge from the Earth's crust and decay to produce showers that are largely electromagnetic. Upper limits on the neutrino fraction are presented in figure 5.5. Top-down models for the acceleration of UHE cosmic rays, predict a large flux of neutrinos. The upper limits presented here are only one order of magnitude higher than the flux expected from neutrinos produced in GZK interactions of extragalactic protons on the CMB. For more information on the limits from the other experiments shown in figure 5.5, see [85].

Photon induced showers are almost purely electromagnetic, and the primary photon is able to penetrate deep into the atmosphere before the cascade is initiated. This allows such showers to be identified by their low muon content and by their relatively deep shower maximum. These showers are easily reconstructed as the evolution of electromagnetic cascades in the atmosphere is well understood and they do not suffer large shower to shower fluctuations. They are also free from uncertainties introduced by hadronic interaction models. The upper limits to the photon fraction are shown as a function of energy in figure

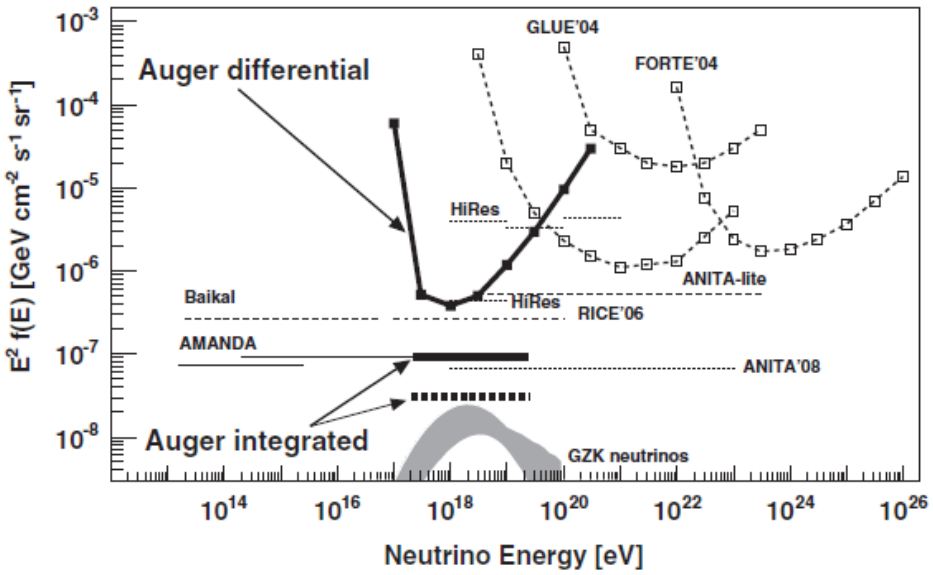

Figure 5.5.: Limits at 90 % CL for each flavor of diffuse UHE neutrino fluxes assuming a proportion of 1:1:1 due to neutrino oscillations. The Auger limits are given using the most pessimistic case of the systematics (solid lines). For the integral, the limit that would be obtained in the most optimistic scenario of systematics is also shown (dashed line). The shaded area corresponds to the allowed region of expected GZK neutrino fluxes computed under different assumptions [87, 88, 89, 90]. The limits from the other experiments shown above are discussed further in [85].

5.6, and they were derived from measurements taken with the Auger surface detectors. They take into account composition sensitive observables such as signal rise-time, curvature of the shower front and reconstructed depth of shower maximum from the FD, as well as its uncertainty. The predicted photon flux from top-down scenarios for the production of cosmic rays are also shown in figure 5.6. These fluxes are relatively high compared to the fluxes predicted by other models, and look unlikely when compared with the latest upper-limits from the Auger detectors. The remaining models that are the closest to the Auger measurements are for photons originating from the GZK effect, indicated by the shaded region.

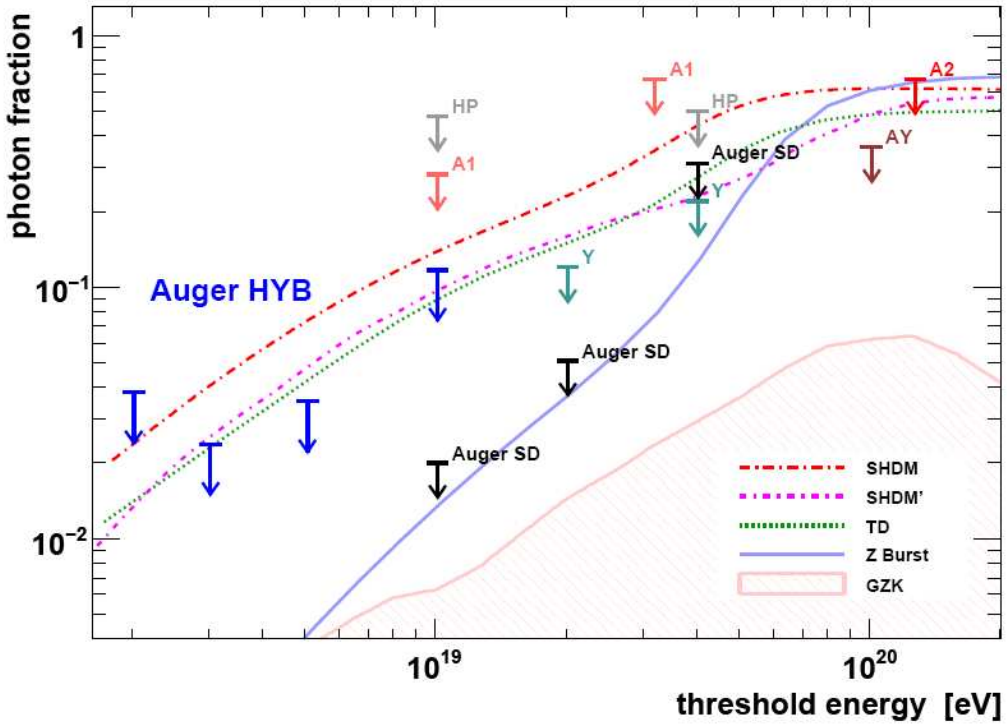

Figure 5.6.: Upper limits on the photon fraction in the integral cosmic-ray flux for different experiments: AGASA (A1, A2) [91, 92], AGASA−Yakutsk (AY) [93], Yakutsk (Y) [94], Haverah Park (HP) [95, 96]. In black are the limits from the Auger surface detector (Auger SD) [97], and in blue are the limits above 2, 3, 5, and 10 EeV (Auger HYB) derived in [98]. The shaded region shows the expected GZK photon fraction as derived in [99]. Lines indicate predictions from top−down models, see [100, 101, 102].

5.3. Anisotropy

In November 2007, the Pierre Auger Collaboration published evidence of anisotropy in the arrival directions of cosmic rays with energies above 57 EeV. Data from the time period 1^{st} January 2004 to the 31^{st} August 2007 were used to set the anisotropy hypothesis. The arrival directions were correlated with the positions of nearby objects from the 12^{th} edition of the Veron-Cetty and Veron (VCV) catalogue of quasars and AGN. This is not an unbiased or complete sample of objects, but it can still be used to demonstrate anisotropy if cosmic rays arrive preferentially close to their directions in the sky. It should be noted that the correlation does not identify individual sources or a particular class of sources, but does provide clues to the extragalactic origin of cosmic rays at the highest energies. Recently, data prior to 31^{st} March 2009 have been added to the earlier data in an attempt to strengthen the argument for anisotropy.

The 27 events included in the 2007 publication had energies above 57 EeV. Using an updated version of the reconstruction procedure, this has now changed to 55 EeV. The arrival directions have only changed by at most 0.1° using this new reconstruction. With the lower energy limit now at 55 EeV, 4 more events are added to the sample and there is now a total of 31 events from this first time period. The angular resolution of these events is better than 0.9° [103]. The integrated exposure for this new data set is nearly double the value for the first data set, with a value of 17040 $\mathrm{km^2\,sr\,yr}$ ($\pm 3\,\%$).

5.3.1. Statistical Significance

An independent data set was used to do an exploratory scan for a correlation of events with energy greater than E_{thres}, with objects in the VCV catalogue with redshifts less than z_{max} within an angular distance ψ. The data were from the time period prior to the 27^{th} May 2006. The scan was designed to find a minimum in the probability P that k or more out of N events from an isotropic flux correlated by chance with objects within the chosen angular scale.

$$P = \Sigma_{j=k}^{N} \left(\begin{array}{c} N \\ j \end{array} \right) p_{iso}^{j} \left(1 - p_{iso}\right)^{N-j} \tag{5.2}$$

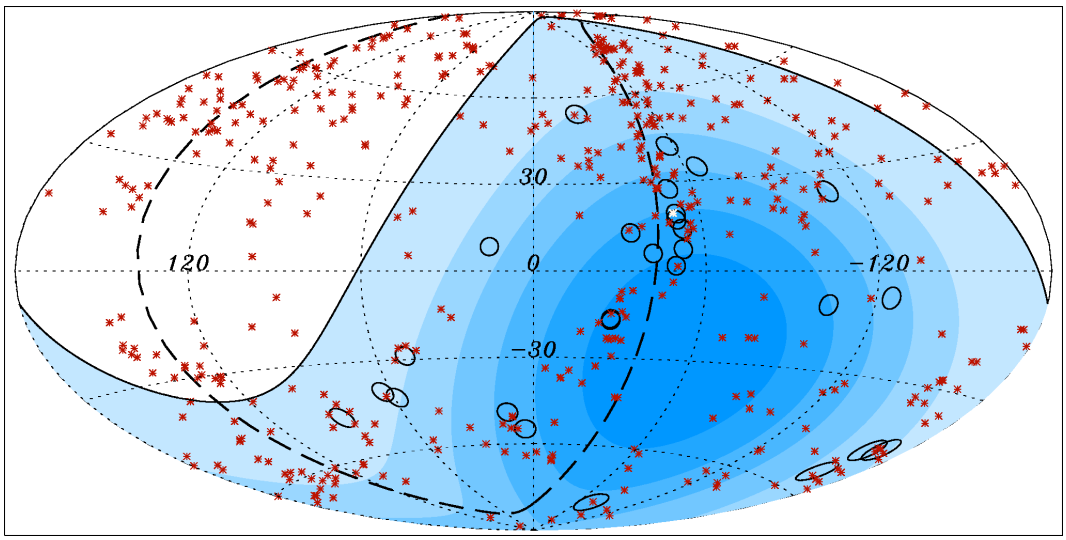

Figure 5.7.: Celestial sphere in galactic coordinates showing arrival directions of the 27 highest energy events detected by Auger with E > 57 EeV. These events are depicted by circles of radius 3.1°. 472 AGN from the VCV catalogue within 75 Mpc are represented by red crosses. The blue region defines the field of view of the Auger southern observatory with deeper blue regions indicating areas of higher exposure. The solid curve marks the boundary of this field of view, defined by a zenith angle of 60°. The location of Centaurus A, the closest AGN, is marked with a white star. Two of the 27 events are within 3° of this marker. The super-galactic plane is indicated by the dashed curve, and it represents a region where a large number of nearby AGN are concentrated.

where p_{iso} is the exposure weighted fraction of the sky accessible to the Pierre Auger Observatory that is within ψ_{max} degrees of potential sources. A minimum value of $P = 0.21$ was found for the parameters $\psi_{max} = 3.1°$, $z_{max} = 0.018$ and $E_{thres} = 55$ EeV (using the new energy reconstruction). This means that the probability that an individual event from an isotropic flux arrives within the fraction of the sky prescribed by these parameters is $p_{iso} = 0.21$. Of the 27 events with energy above this threshold prior to 31^{st} August 2007, 9 of the 13 after the exploratory phase correlated with AGN compared to the 2.7 expected for an isotropic flux. This gave a 99 % significance level for rejecting the hypothesis that the distribution of arrival directions is isotropic. The arrival directions are correlated with the direction of the super-galactic plane, indicated by a dashed line in figure 5.7.

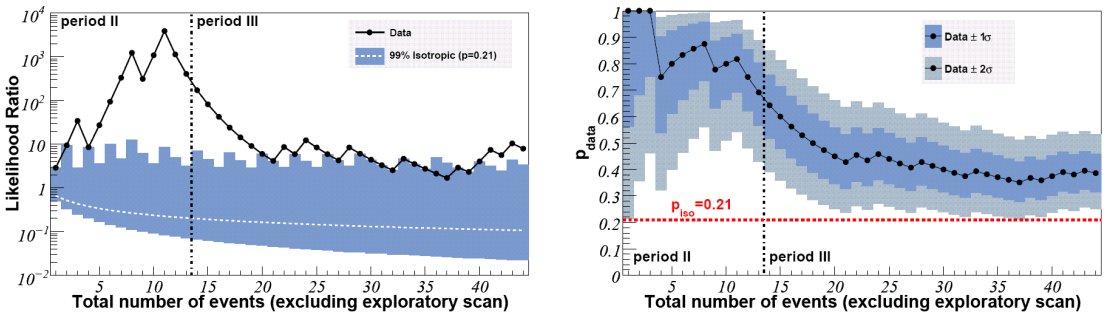

Figure 5.8.: Monitoring the correlation signal. Left: The sequential analysis of cosmic rays with energy greater than 55 EeV arriving after 27 May, 2006. The likelihood ratio log_{10} R for the data is plotted in black circles. Events that arrive within $A_{max} = 3.1°$ of an AGN with maximum redshift $z_{max} = 0.018$ result in an up-tick of this line. Values above the area shaded in blue have less than 1% chance probability to arise from an isotropic distribution ($p_{iso} = 0.21$). Right: The most likely value of the binomial parameter $p_{data} = k/N$ is plotted with black circles as a function of time. The $1\,\sigma$ and $2\,\sigma$ uncertainties in the observed value are shaded. The horizontal dashed line shows the isotropic value $p_{iso} = 0.21$. The current estimate of the signal is 0.38 ± 0.07. In both plots, events to the left of the dashed vertical line correspond to period II of Table I and those to the right, collected after [1], correspond to period III.[104]

$$R = \frac{\int_{p_{iso}}^{1} p^k (1-p)^{N-k} dp}{p_{iso}^k (1-p_{iso})^{N-k+1}} \tag{5.3}$$

The likelihood ratio R, defined by equation 5.3, is the ratio between the binomial probability of correlation and the binomial probability in the isotropic case ($p_{iso} = 0.21$). On the left in figure 5.8 is the likelihood ratio of correlation as a function of the total number of time−ordered events, observed since 27^{th} May 2006, which excludes the data used in the exploratory scan. Period II includes data from this date up until the 2007 publication, and period three is from this publication until March 2009. The recent data neither strengthen or weaken the case for anisotropy. A total of 17 out of 44 events, from periods two and three combined, correlate with the location of known AGN. On the right in figure 5.8, the degree of correlation $p_{data} = k/N$ is plotted as a function of time−ordered events. The one and two sigma uncertainties are plotted also, which are determined such that the area under the posterior distribution function is equal to 68 % and 95 % respectively. For

$k = 17$ and $N = 44$ we have $p_{data} = 0.38$, which is more than two sigma away from the value for isotropy.

5.3.2. Posteriori Analysis

It is also possible to do a posteriori analysis, but no statistical significance can be assigned. This involves analysing all 58 events with $E > 55$ EeV prior to 31^{st} March 2009, including the events used for the exploratory scan. Figure 5.9 shows the angular separation between arrival directions of the events with the closest object in the VCV catalogue with redshifts $z \leq 0.018$, with the cumulative distribution on the left and the differential on the right. Also shown is the average distribution expected for an isotropic flux. There are 13 events with a galactic latitude of $| b | < 12°$, which are shaded in the differential plot. Only one of the thirteen correlates with an AGN with angular separation of less than 3°. This can either be explained by the incompleteness of the VCV catalogue especially at galactic latitudes around zero due to obscuration by the Milky Way, or by larger magnetic bending of the cosmic ray trajectories along the galactic disk.

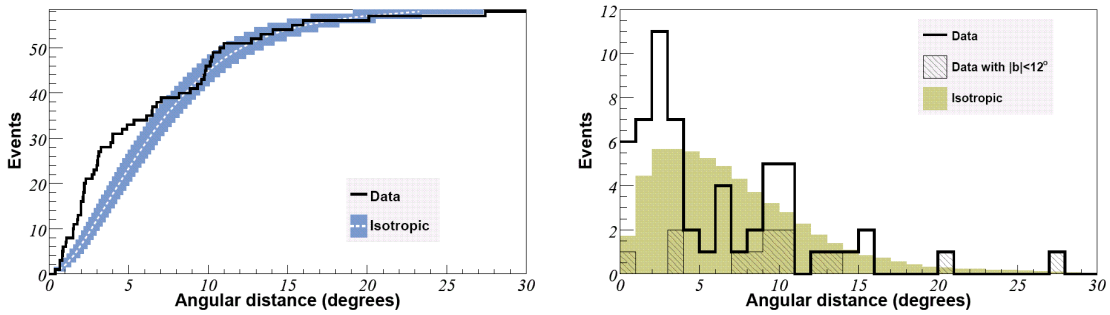

Figure 5.9.: The distribution of angular separations between the 58 events with E > 55 EeV and the closest AGN in the VCV catalogue within 75 Mpc. Left: The cumulative number of events as a function of angular distance. The 68% the confidence intervals for the isotropic expectation is shaded blue. Right: The histogram of events as a function of angular distance. The 13 events with galactic latitudes $| b | < 12°$ are shown with hatching. The average isotropic expectation is shaded brown [104].

An excess of events were observed close to the radio source Centaurus A. [2]. As in figure 5.9,

[2] Centaurus A (l,b) = (−50.5°,19.4°)

figure 5.10 shows the angular separation of the 58 highest energy events from Centaurus A with the cumulative distribution on the left and the differential on the right. The largest deviation from isotropy occurs within an 18° radius on Cen A with 12 events within this angular distance, compared to 2.7 events expected for an isotropic flux.

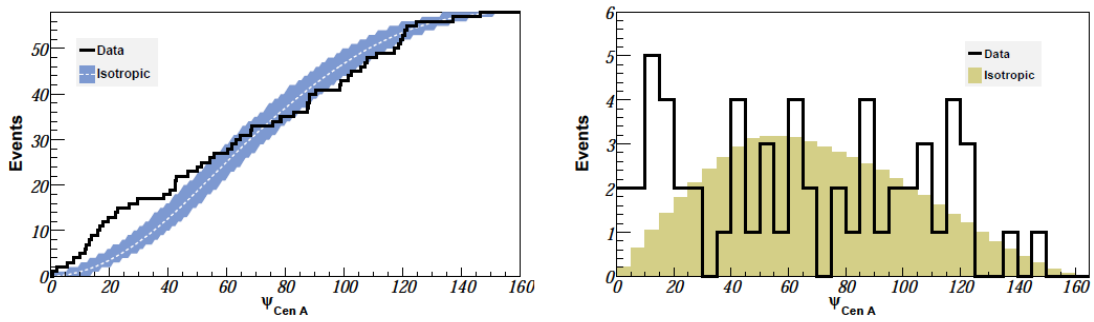

Figure 5.10.: Left: The cumulative number of events with $E > 55\,\mathrm{EeV}$ as a function of angular distance from Cen A. The average isotropic expectation with approximate 68 % confidence intervals is shaded blue. Right: The histogram of events as a function of angular distance from Cen A. The average isotropic expectation is shaded brown [104].

5.4. Astrophysical Models

The combined energy spectrum has been compared to spectral shapes expected from different astrophysical scenarios. Figure 5.11 shows this spectrum along with models that have different injection spectra and compositions, as well as different cosmological evolutions of source luminosity $(z+1)^m$. The best agreement is obtained for a scenario with strong cosmological $m = 5$, and a hard injection spectrum $\propto E^{-2.3}$. Above the ankle a pure iron composition with an $E^{-2.4}$ injection spectrum and a uniformly distributed source distribution with cosmological evolution $m = 0$ scenario provides the best fit.

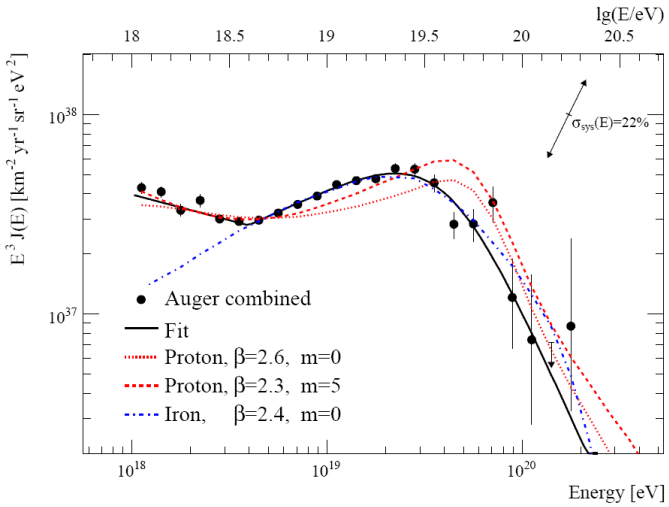

Figure 5.11.: The combined energy spectrum compared with several astrophysical models assuming a pure composition of protons (red lines) or iron (blue line), a power-law injection spectrum following $E^{-\beta}$ and a maximum energy of $E_{max} = 10^{20.5}$ eV. The cosmological evolution of the source luminosity is given by $(z+1)^m$. The black line shows the fit used to determine the spectral features [78].

5.5. Conclusion

Chapter 5 presented results from the 2009 International Cosmic Ray Conference. These included the surface, hybrid and combined energy spectra, results from composition studies and upper limits to the photon and neutrino fluxes, and the results from anisotropy studies. Also discussed were the systematic uncertainties associated with the reconstructed energies. The current uncertainty in the energy assignment is 22 % for both hybrid and surface detector events. The energy uncertainty affects anisotropy studies as well as the determination of the depth of shower maximum which is used in composition studies.

The work presented in the next three chapters, addresses three of the systematic uncertainties listed in table 5.1: the hybrid reconstruction method, water vapour pressure quenching and multiple scattering models. Understanding the uncertainties associated with the hybrid reconstruction process is vital to determining cosmic ray energies, mass composition and arrival directions.

6. Vapour pressure dependence of the Air Fluorescence Yield

Experiments that employ the fluorescence technique for the detection of ultra-high energy cosmic rays, rely strongly on laboratory measurements of the fluorescence yield, to convert the light collected at the telescopes to the energy deposited in the atmosphere by the EAS. Initially the Pierre Auger Collaboration used the assumption that the fluorescence yield was independent of humidity, and that cross-sections for collisional de-excitation were temperature independent. Recently, the AIRFLY Collaboration has shown through laboratory experiments that these two factors must be taken into account to accurately calculate the air fluorescence yield [105]. To do so, the absolute humidity and temperature profiles must be known to sufficiently high accuracy and precision. This can be especially difficult in the case of the absolute humidity, referred to here as vapour pressure, as this is a highly variable quantity. In this chapter, I present work done in creating monthly vapour pressure profiles for the Southern Auger site, using data from radiosonde launches conducted during $2002 - 2008$, and I discuss the impact that these profiles and their uncertainties have on the reconstructed shower energies and depths of shower maximum. This work was done in parallel with Martin Will from Universität Karlsruhe, whose work and conclusions can be found in [106]. I also present the effect of including the temperature dependence of collisional cross-sections into the fluorescence yield calculation. Lastly, I present ideas for possible improvements to the use of monthly vapour pressure models, by utilising real time data from the weather stations and a vertical cloud monitor.

6.1. Air Fluorescence Yield

Knowing the fluorescence yield of a charged particle travelling through the atmosphere is crucial to the reconstruction of EAS data obtained by a fluorescence detector. The uncertainties in the fluorescence yield contribute largely to the uncertainty in the value of the reconstructed energy, and as the FD is used to calibrate the SD, they also propagate through to the SD energy estimates. What makes this difficult, is that the fluorescence yield is dependent on the temperature, pressure and composition of the atmosphere at the site of the excitation. Laboratory measurements of the air fluorescence yield have been made by injecting electrons of known energies into tanks of known composition, pressure and temperature of air, and counting the fluorescence photons using photomultiplier tubes [45]. By holding all but one parameter constant, the dependence of the fluorescence yield on energy, concentration etc. have been measured.

Only a small fraction of the ionisation energy deposited in the atmosphere results in the production of fluorescence light. Through collisions with other molecules, referred to as collisional quenching, the excited molecules can de-excite without the production of fluorescence light. To be able to convert between ionisation energy deposited in the atmosphere and the fluorescence light produced, we need to know the efficiency of fluorescence production. The fluorescence efficiency of the atmosphere is given by

$$\varepsilon\left(p,T\right)=\frac{rate\ of\ de-excitation\ via\ radiation}{total\ rate\ of\ de-excitation}=\frac{\tau_0}{\tau_0+\tau_c} \tag{6.1}$$

where τ_0 is the mean life time of the excited states of N_2. The average time between collisions, τ_c, is inversely proportional to the average speed $\bar{v}$ of the molecules, as expressed in equation 6.2.

$$\bar{v}=\sqrt{\frac{8kT}{\pi M}} \tag{6.2}$$

For collisions between two N_2 molecules, τ_c is given by equation 6.3

$$\tau_c=\left(\sqrt{2}\rho_n\sigma_{NN}\bar{v}\right)^{-1}=\sqrt{\frac{\pi M}{kT}}\left(4\rho_n\sigma_{NN}\right)^{-1} \tag{6.3}$$

Here, ρ_n is the particle number density, σ_{NN} is the collisional cross-section between N_2 and N_2, T is the temperature in Kelvin, M is the molecular mass and k is the Boltzmann constant. From here the fluorescence efficiency is defined as

$$\varepsilon_\lambda(p,T) = \frac{nE_\gamma}{E_{dep}} = \frac{\varepsilon_\lambda(p \to 0)}{1 + (p/p'_\nu(T))}\,, \tag{6.4}$$

with $\varepsilon_\lambda(p \to 0)$ being the fluorescence efficiency at wavelength λ in the absence of quenching, E_{dep} is the deposited energy, n is the number of photons of energy E_γ, and $p/p'_\nu(T)$ is the pressure p of the observed medium divided by a reference pressure $p'_\nu(T)$ equal to $\tau_{o,\nu}/\tau_{c,\nu}$, the mean life-times for excitation level ν.

Assuming air to be a two component gas (molecular nitrogen and oxygen), the ratio $p/p'_\nu(T)$ can be expressed as

$$\frac{p}{p'_\nu(T)} = \tau_{o,\nu}\left(\frac{1}{\tau_{NN,\nu}(\sigma_{NN,\nu})} + \frac{1}{\tau_{NO,\nu}(\sigma_{NO,\nu})}\right) \tag{6.5}$$

The result is a fluorescence yield (in units of photons per metre of particle track), that is dependent on the pressure and temperature of the gas.

$$FY_\lambda = \varepsilon(p,T)\frac{\lambda}{hc}\frac{dE}{dX}\rho_{air}\ [\frac{photons}{m}] \tag{6.6}$$

where $\frac{dE}{dX}$ is the total ionisation energy loss rate.

To be able to use these calculations of the fluorescence yield, we require accurate atmospheric profiles.

6.2. Atmospheric Profiles

The height profiles of atmospheric parameters above the Pierre Auger Observatory are constructed from data obtained by conducting atmospheric soundings at the site [107].

Radiosondes are attached to helium balloons, and take data as they ascend over the array. The data are transmitted back to a radio receiver over distances of up to 250 km. The payloads can continue taking data up to heights of 40 km, but the balloons generally burst at $20 - 25$ km. They take data every 8 seconds and their height and position is determined from GPS. When the launches began in 2002 they were conducted from various locations near Malargue. Since July 2005, all ascents have been launched from an on-site balloon launching station (BLS), located near the Coihueco fluorescence detector. This location is preferable as the wind generally comes from the west, carrying the balloon across the array as it ascends. Prior to this date they were launched from the BLS located on the south-western edge of the array, and the wind generally carried them north-east across the array. They take readings of temperature, pressure, relative humidity, wind speed and direction. The wind speed and its direction are determined by comparing the relative position of the balloon from consecutive readings. As the rate of ascent is not constant, the height between subsequent readings varies. The atmospheric parameters measured by the radiosondes and the accuracy and ranges of the measurements are listed in table 6.1.

Table 6.1.: Atmospheric parameters measured by the radiosondes as well as their accuracy and range [108].

NOTE:
This table is included on page 82 of the print copy of the thesis held in the University of Adelaide Library.

6.3. Atmospheric Monitoring

Along with the balloon-borne atmospheric soundings, atmospheric monitoring is performed at the Pierre Auger Observatory using weather stations and LIght Detection And Ranging (LIDAR) stations, located at each fluorescence detector station and at the centre of the array. Infra-red cloud cameras are located at each fluorescence detector site to monitor the cloud cover in the fields of view of the FDs.

Together, this information is used to calculate the attenuation of the fluorescence light from the shower to the detector, and to calculate the fluorescence yield that is dependent on temperature, pressure and vapour pressure.

6.3.1. Weather Stations

The weather stations measure atmospheric conditions at the ground level every 5 minutes. They are located at each of the fluorescence detector sites and at the centre of the array near the central laser facility (CLF). They each have a capacitive pressure sensor, a combined temperature and relative humidity sensor, and a separate wind speed sensor. The units, accuracy and range of these measurements are listed in table 6.2. By having several weather stations located throughout the array, the lateral homogeneity of the atmospheric properties at ground level can be studied (discussed further in section 6.12.1).

Table 6.2.: Atmospheric parameters measured by the weather stations as well as their accuracy and range [109].

NOTE:
This table is included on page 83 of the print copy of the thesis held in the University of Adelaide Library.

6.3.2. Cloud Cameras

Infra-red cloud cameras are located at the site of each FD, and they take images of the sky over the surface array, in the field of view of the fluorescence detectors [110]. Images of the FD field of view are taken every 5 minutes, and once every 15 minutes the camera takes multiple pictures to create a mosaic of the whole sky. The raw data from these images can be used to determine which pixels on the FD cameras have cloud in their field of view at any given time that may have affected the reconstruction of a shower's longitudinal profile.

This is illustrated in figure 6.1. The 5 images in each of the top two rows correspond to the 5 pictures taken by the infra-red cloud camera that covers the 180°azimuthal by 30° elevation field of view of the fluorescence detector. The top row of images are the raw images from the cloud camera. The middle row is the result from the analysis, and the bottom row is the result of the analysis projected onto the 6 cameras at one of the FD sites. The different shades of grey in the bottom image represent how much of a pixel is obstructed by cloud, with white corresponding to 100 % contamination. The bright band at the bottom of the top image, which is labelled as cloud in the middle image is the horizon. This is not in the field of view of the detectors and as such does not appear in the bottom image.

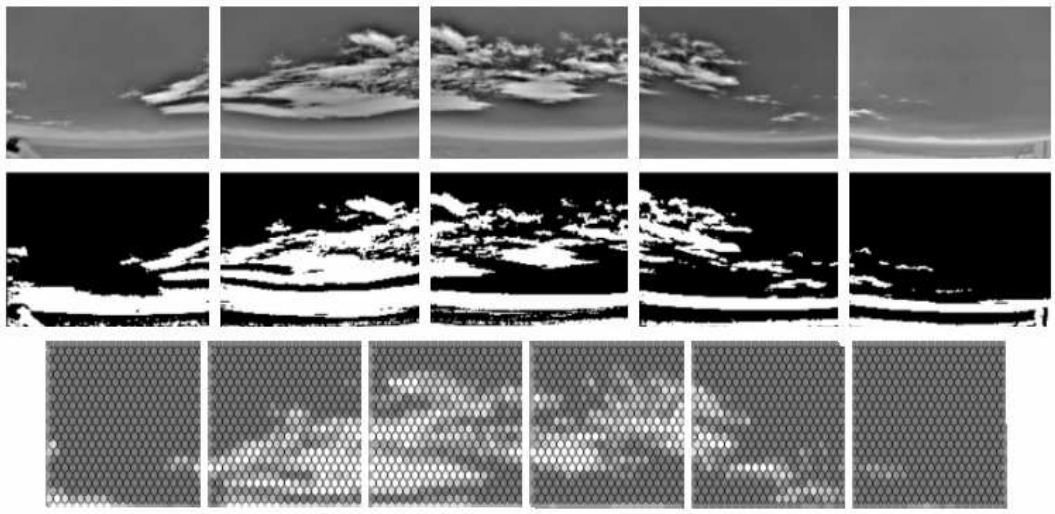

Figure 6.1.: Top: Raw infra-red image of the sky above the ground array in the field of view of one of the FD sites. Middle: Processed image in which each pixel is assigned black (no cloud) or white (cloud). Bottom: Middle image overlayed onto the cameras at the FD, where the shade of grey represents the fraction of the pixel contaminated by cloud.

The raw images are processed using image processing software called PACMan, developed by Michael Winnick for the Auger Collaboration. His work is detailed in [111]. This program determines if the reading from each individual pixel in the image contains cloud. The result is a black and white image, with black corresponding to clear sky, and white for cloud. Two such images are presented in figures 6.2 and 6.3, one that PACMan classified as clear, and the other as overcast.

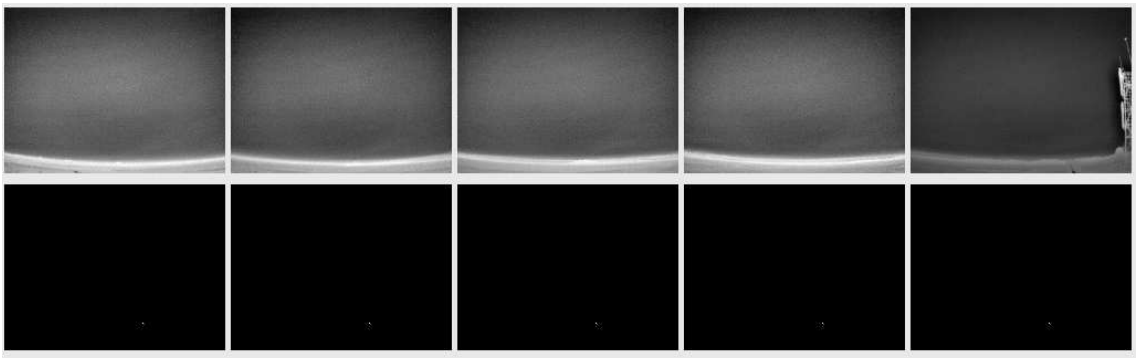

Figure 6.2.: Coihueco infrared cloud camera images at the beginning of a radiosonde launch, local time 21:35 17/08/2006. The entire field of view is shown. The bright band along the bottom of the images in the top row is the horizon. The images on the top row are the raw images, and the bottom row shows the analysis of the images directly above them. This analysis was performed by PACMan, image processing software developed by Michael Winnick for the collaboration, that determines whether a pixel contains cloud. The white corresponds to cloud, and black to clear sky. The sky appears to be completely clear.

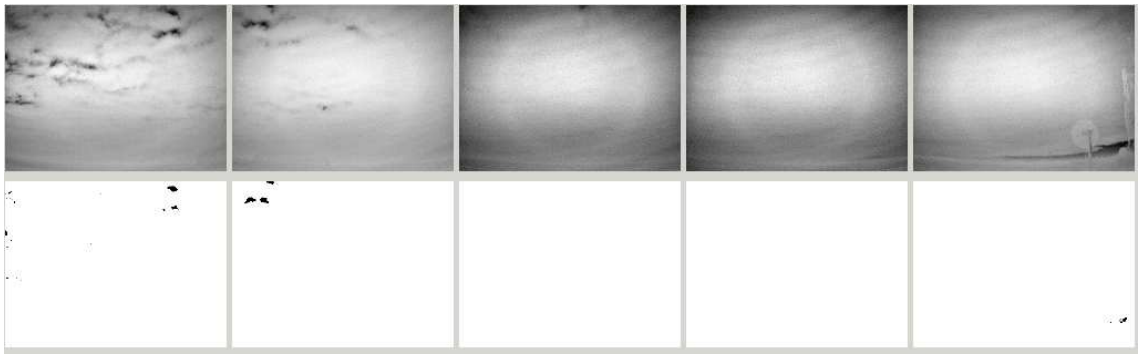

Figure 6.3.: Coihueco infrared cloud camera images near the beginning of a radiosonde launch, local time 06:40 21/04/2007. The sky appears to be completely overcast.

6.3.3. Infra-red Vertical Cloud Monitor

The Vertical Cloud Monitor (VCM) located at the CLF records the temperature of the sky using a single pixel infra-red detector, which has a response centred at $\lambda = 10\,\mu m$ and has a field of view of 3°. By measuring the sky temperature without further calibration with ground temperatures, we obtain the uncompensated sky temperature. If this value is below -20°C then the sky is generally clear, and if the temperature is greater than -10°C then the sky is most likely overcast. This method of detecting clouds is only valid for night time, as the pixel saturates during the day. Data collection began in April 2005, so radiosonde launches conducted before this date cannot be classified by this method.

Figure 6.4 shows the sky temperature readings for 21^{st}April 2007. This is in universal time, so three hours need to be subtracted to obtain the local time. The sky started off clear, as the uncompensated temperature shown in red is below -20°C. This steadily creeps up, until at 0900 hrs UT, when the sky is completely overcast, corresponding to a reading of 0°C. The readings then lose meaning once the sun is high in the sky, as the pixel saturates.

Figure 6.5 presents data from a radiosonde that was launched at 0625 hrs local time, corresponding to 0925 hrs UT, on the 21^{st}April 2007. It can readily been seen that there is a peak in the relative humidity and a temperature inversion at the same height. This was at the same time, and on the same day as the overcast conditions shown by the uncompensated sky temperatures in figure 6.4.

6.3.4. LIDAR

At the site of each fluorescence detector, the vertical optical depth of the atmosphere can be measured using an elastic back-scatter LIDAR station [112]. This is done to determine the attenuation of light due to aerosol scattering. It is monitored up to a height of 20 km and is performed every hour during an observation run, outside of the field of view of the FDs[113]. The LIDAR has a pulsed UV laser with pulse frequency $333\,Hz$ and wavelength 351 nm, which is roughly the average wavelength of the nitrogen fluorescence spectrum. The light is back-scattered by aerosols in the atmosphere to be received by three 80 cm

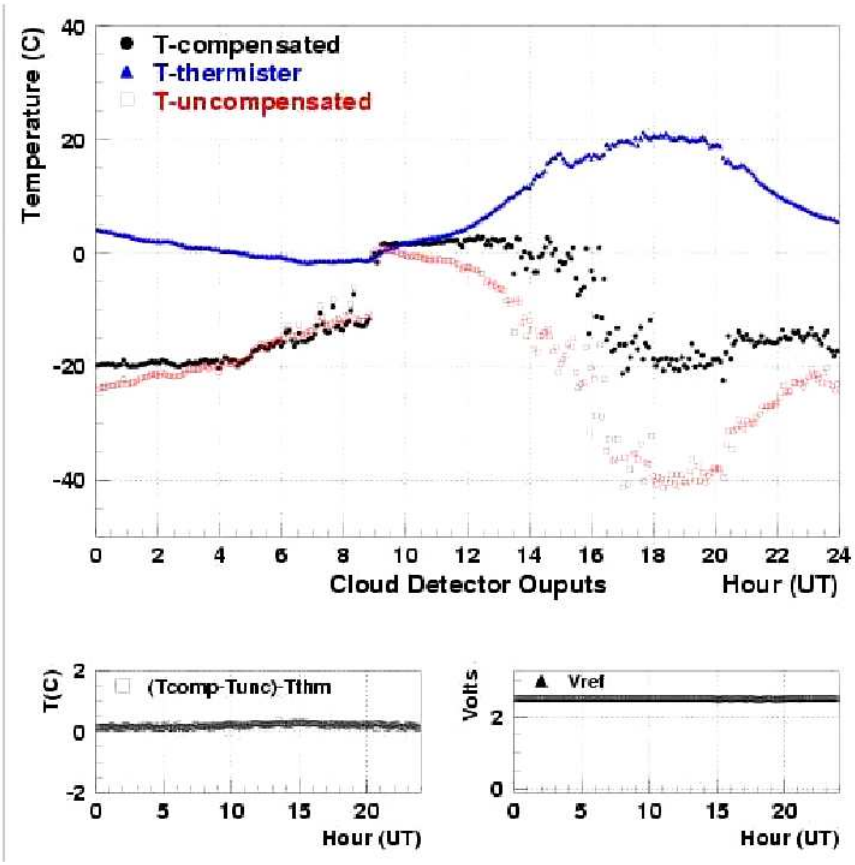

Figure 6.4.: This shows the readings from the vertical cloud monitor. The uncompensated temperature is the one that gives us an indication of the cloud cover above the site. It appears to be clear until 0500 hrs UT, and then by 0900 hrs UT the sky is overcast. The readings lose all meaning after the sun appears overhead as the infra-red pixel saturates. This can be seen from 1200 hrs UT onwards.

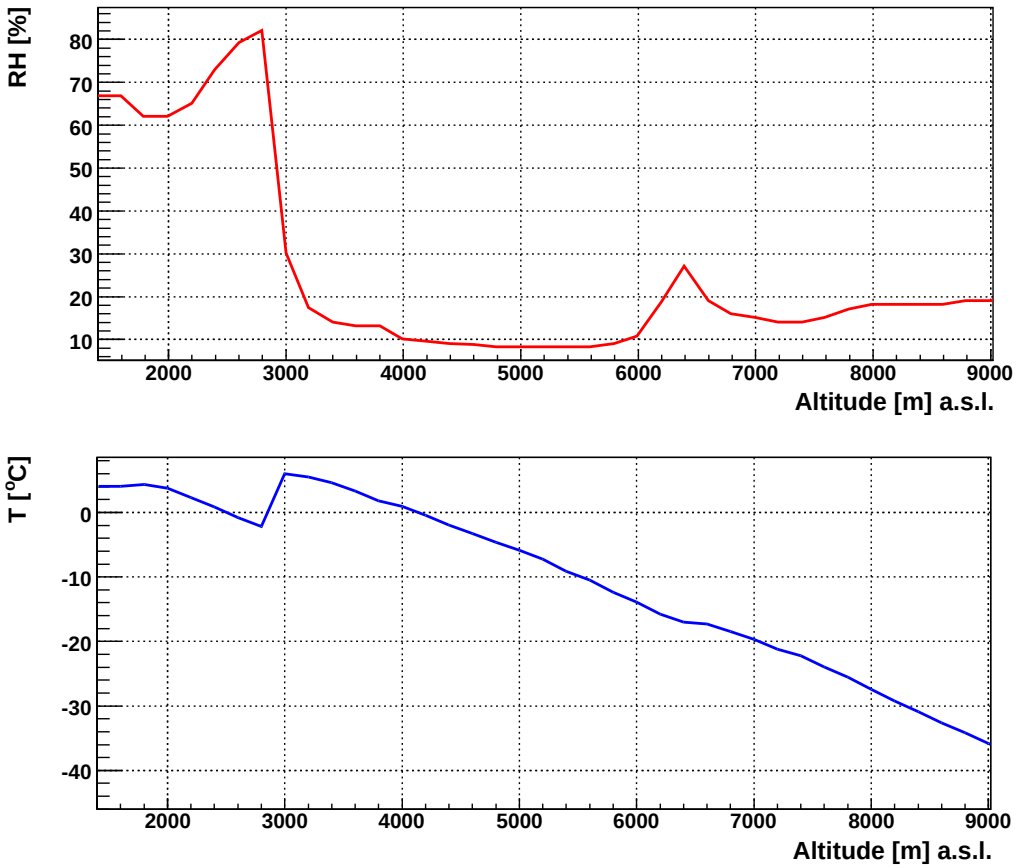

Figure 6.5.: Data from a radiosonde launch conducted on 21/04/2007 at 0625 hrs. Both a peak in the relative humidity and a temperature inversion are observed at the same height.

diameter mirrors that focus the light onto a PMT. The detector is mounted on a steerable frame and can be pointed in any direction within the hemisphere to an accuracy of 0.2°. Scans are conducted every hour, including measuring low lying aerosol concentrations over the array by taking horizontal measurements. A LIDAR can also be used to "Shoot-the-Shower" [114]. This involves aiming a series of laser shots along the track of a detected shower to directly observe the atmospheric scattering properties between the shower track and the fluorescence detectors. It can also be used to determine if there were clouds moving in the field of view of the FD/FDs which observed the event.

6.3.5. Central and eXtreme Laser Facilities

The Central Laser Facility (CLF) [115] and the eXtreme Laser Facility (XLF), are both located near the centre of the ground array and are roughly equidistant from each eye. They are similar to the LIDAR in that they are comprised of a pulsed 355 nm laser mounted on a steerable frame. Instead of measuring the back scattered light, the fluorescence detectors observe the laser shot, and the scattering from the centre of the array to the FD can be determined. By comparing the attenuation of the light measured by each FD, the lateral uniformity of the aerosol distribution can be measured. The energy and geometry of the laser shot is well known. Therefore, by comparing the reconstructed energy and geometry determined by the FD, the reconstruction process can be checked using the CLF.

Together all of these facilities assist in the reconstruction of EAS at the southern Pierre Auger observatory.

6.4. Collisional quenching by water vapour

The fluorescence yield of air was determined from laboratory measurements at reference pressures, temperatures and air compositions. Initially calculations were performed using dry air, to eliminate the variable of humidity. More recently the AIRFLY collaboration has studied the effect of humidity on the fluorescence yield.

From the derivation described in [105], the fluorescence yield at wavelength λ, temperature T and pressure p, can be expressed as

$$Y_{air}(\lambda, p, T) = Y_{air}(337, p_0, T_0) I_\lambda(p_0, T_0) \frac{1 + \frac{p_0}{p'_{air}(\lambda, T_0)}}{1 + \frac{p}{p'_{air}(\lambda, T_0)\sqrt{\frac{T}{T_0}}\frac{H_\lambda(T_0)}{H_\lambda(T)}}} \tag{6.7}$$

where $Y_{air}(337, p_0, T_0)$ is the absolute yield of the 337 nm band (photons emitted per MeV of energy deposited) at pressure and temperature $p_0 = 800$ hPa and $T_0 = 293$ K. $I_\lambda(p_0, T_0)$ is the λ band intensity relative to the 337 nm band, and $p'_{air}(\lambda, T_0)$ is the band quenching reference pressure. $H_\lambda(T)$ takes into account the temperature dependence of collisional de-excitation cross sections.

In this section where we study the effect of collisional quenching by water vapour, the temperature effect has been excluded by setting $\frac{H_\lambda(T_0)}{H_\lambda(T)}$ equal to 1. The effect of including the temperature dependence of the collisional de-excitation cross sections will be investigated in section 6.11. In the current reconstruction process both effects are not taken into account.

To introduce quenching by water vapour, the following substitution is made in equation 6.7.

$$\frac{1}{p'_{air}} \longrightarrow \frac{1}{p'_{air}} \left(1 - \frac{p_h}{p}\right) + \frac{1}{p'_{H_2O}} \frac{p_h}{p} \tag{6.8}$$

where p_h is the water vapour pressure and p'_{H_2O} is the water vapour collisional quenching pressure.

To be able to introduce this improvement to the current fluorescence calculation, both the vapour pressure as a function of height, and the water vapour collisional quenching pressure for each excitation level are required. The former must come from measurements at the project site, and the latter from laboratory measurements.

6.4.1. Measurement of quenching parameters

The humidity dependence of the air fluorescence yield has been measured by the AIRFLY Collaboration [105]. Fluorescence measurements were taken at a single temperature and

pressure, at relative humidities ranging from 0 % to 100 %, corresponding to water vapour pressures up to 25 hPa. The values of the parameter p'_{H_2O} are presented for four wavelength bands in table 6.3. For more information on the experimental setup see reference [45].

The wavelengths for which the quenching parameters were calculated correspond to the highest intensity emission wavelengths from each of the molecular nitrogen vibrational state emission bands. The same values of p'_{H_20} can be used for all wavelengths produced from the same initial electronic-vibrational excited state.

Table 6.3.: Measurement of water vapour collisional quenching pressure p'_{H_20} for each of the molecular electronic-vibrational excited state emission bands by the AIRFLY Collaboration [105].

NOTE:
This table is included on page 91 of the print copy of the thesis held in the University of Adelaide Library.

6.5. Vapour Pressure Profiles

Data acquired from the radiosonde launches (as discussed in section 6.2) can be used to create vapour pressure profiles. These then allow the effect of collisional quenching by water vapour on the fluorescence yield to be taken into account. Using readings of relative humidity and temperature, the vapour pressure, referred to from here on as ν[hPa], can be calculated by multiplying the Magnus formulae [116] for the saturation vapour pressures for $T \geq 0°$ and $T < 0°$, and multiplying them by the relative humidity (RH):

$$\nu[hPa] = 6.1078\, e^{\left(\frac{17.08085T}{234.175+T}\right)} \times RH \quad T \geq 0°C \tag{6.9}$$

$$\nu[hPa] = 6.10714\, e^{\left(\frac{22.44294T}{272.44+T}\right)} \times RH \quad T < 0°C \tag{6.10}$$

This can be done for the relative humidity and temperature readings (in $°C$) from each individual launch, and averaged to create monthly or seasonal vapour pressure profiles. As the radiosonde readings are taken every 8 seconds, rather than after a fixed height has been traversed, the data from each launch contains readings taken at different heights, with anywhere between 3−50 meters being traversed between readings [116]. To deal with this problem, an artificial point every 200 m has been interpolated, beginning at 1600 or 1800 meters depending on the elevation of the launch site. This was done by B. Keilhauer, a member of the Auger Collaboration, who published her seasonal humidity profiles and their effect on the fluorescence yield in [117]. She created these seasonal profiles using the radiosonde launch data from August 2002− December 2008. The work presented here attempts to recreate her work, and then tries to improve the precision and possibly the accuracy, with which the effect of vapour pressure on the fluorescence yield can be determined. Therefore, I only used data from the same launches as Keilhauer did in creating her initial seasonal relative humidity profiles. This work was conducted in parallel with Martin Will, who has published his findings in his diploma thesis [118].

6.6. Seasonal Profiles

Initially, due to low statistics, seasonal relative humidity profiles were calculated by B. Keilhauer to illustrate the effect of including humidity dependence into the fluorescence yield calculation. The number of launches used to create the Spring, Summer, Autumn and Winter profiles were 31, 20, 28 and 31 respectively. All of these launches were conducted between 00:00 UTC and 09:59 UTC, which corresponds to 2100 hrs and 0659 hrs local time. Both the vapour pressure profiles and the uncertainty in these profiles are presented in figure 6.6. The error bars in the top plot are one standard deviation, and these are shown in the bottom plot. As can be seen in the top image there are large differences in the seasonal profiles, especially within the first few kilometres. The uncertainties at these heights are also quite large. The standard deviations were calculated by comparing the individual launch vapour pressure profiles with the average seasonal profiles.

6.6.1. Implementing the correction

The seasonal models were placed in data files and read into a local version of the $\overline{Off}\underline{line}$ [119], which is the official reconstruction and simulation software of the Pierre Auger Observatory. At each step where the fluorescence yield was calculated, the relevant vapour pressure profile, based on the season in which the event occurred, is selected and the correction was applied. To obtain the vapour pressure for any given height, linear interpolation was used between each 200 m height increment for which a value of the vapour pressure exists. These vapour pressure profiles were called from a separate text file, rather than from the atmospheric database. Once a set of vapour pressure profiles are decided on by the collaboration, the end product would be added to a MySQL database for access by anyone running the $\overline{Off}\underline{line}$ software. Currently only relative humidity is available through the database, but this will be changed shortly to allow the vapour pressure to be accessed directly. This is important as a different result is obtained by using the average relative humidity and the average temperature profiles to create an average vapour pressure profile, compared to calculating the individual vapour pressure profiles and then averaging.

6.6.2. Shift in reconstructed parameters

The reconstructed showers are all from the 2007 ICRC elongation rate data set. This means that they have all passed high quality cuts and anti-bias cuts. Information on these quality and anti-bias cuts can be found in [120]. Table 6.4 lists the observed relative shifts in energy and the absolute shift in X_{max} for 3,927 events. The events have been divided up into the four seasons, by the date on which the event was recorded. Histograms of the energy shifts are presented in figure 6.7. On average the shifts are small. However shifts in energy of $7\,\% - 8\,\%$ were observed for some events.

The showers that are most affected by the humidity dependence of the fluorescence yield, are showers that occur during summer, when the vapour pressure near the ground is at its highest. The effect is also larger the closer a shower maximises to the ground, which are vertical showers with energy around 10^{19} eV, or inclined showers with larger energies. As such the correction appears to have an energy dependence. However, on average, showers

Table 6.4.: Lists of the average shifts in the reconstructed shower energies and X_{max}, as well as the RMS of these distributions. These shifts are the result of using the seasonal vapour pressure profiles created in section 6.6, to calculate the effect of including the vapour pressure dependence in the fluorescence yield calculation for 3927 high quality events.

Season	$\frac{\Delta E}{E}$ [%]	RMS [%]	ΔX_{max} $[\frac{g}{cm^2}]$	RMS $[\frac{g}{cm^2}]$
Summer	2.4	1.3	4.5	2.7
Autumn	2.1	1.2	3.7	2.3
Winter	1.2	0.6	1.8	0.9
Spring	1.5	0.7	2.4	1.1

maximise at around 4km above the ground level, where the vapour pressure is roughly 25 % of its value at the ground level. This explains why on average the relative shift in energy is only a couple of percent. The shifts in energy are all positive ($\triangle E = E_{new} - E_{old} > 0$), and the change in the depth of shower maximum ($\triangle X_{max} = X_{new} - X_{old} > 0$) is always an increase in the depth.

6.6.3. Uncertainties in seasonal profiles

The uncertainty on the humidity correction to the yield can be up to 50 %, due to the large fluctuations in the vapour pressure profiles within the first few kilometres above the ground within each season. This may become important for high energy events for which the magnitude of the correction can approach $8 - 10$ %. One way to reduce this uncertainty would be to create monthly profiles rather than seasonal profiles. While this will reduce the number of launches used to create each profile, it is worth investigating to see if, despite the reduction in statistics, the uncertainty can be improved.

Another task is to investigate the weather conditions at the times of each launch, to determine if rain, fog or overcast conditions are leading to the large variation between individual vapour pressure profiles.

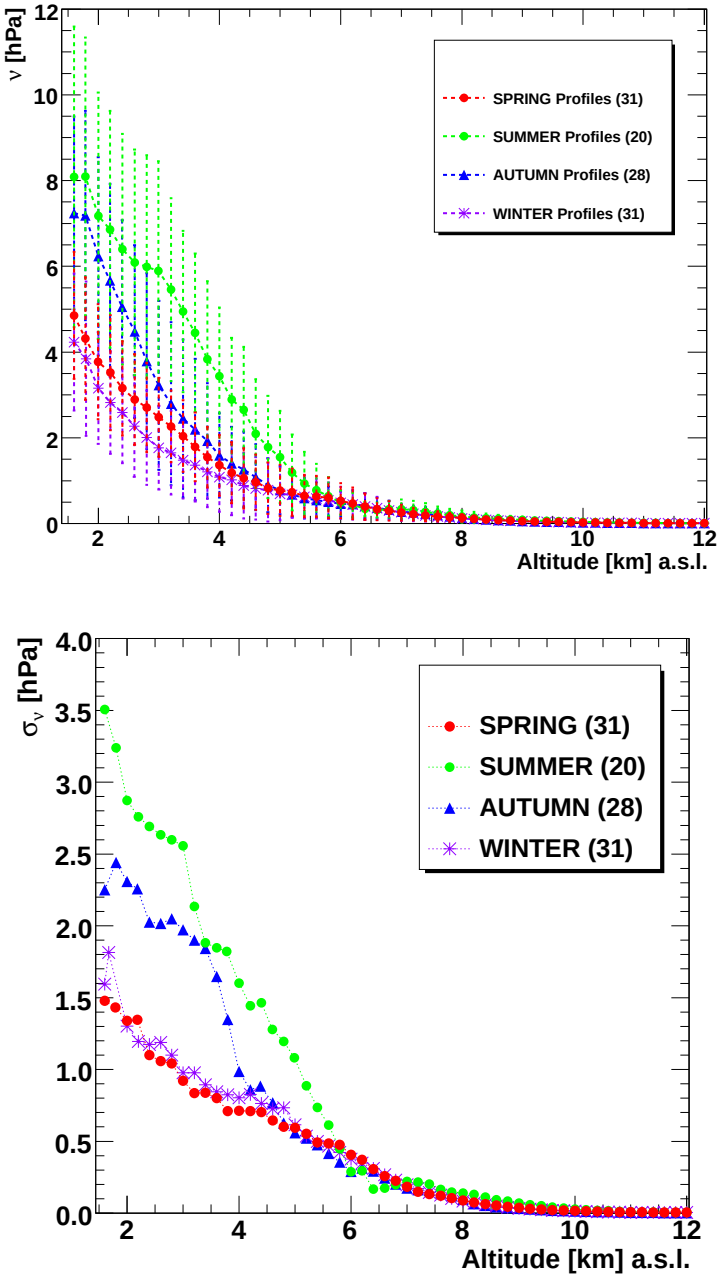

Figure 6.6.: Top: Seasonal vapour pressure profiles constructed using data from night-time radiosonde launches conducted over the southern Pierre Auger Observatory. The error bars represent one standard deviation in the mean. The numbers next to the seasons in the legend correspond to the number of launches used to create each profile. Bottom: The standard deviations from the top figure, plotted as a function of height. These are large near the ground, especially in the summer and autumn seasons ($\sim 50\,\%$).

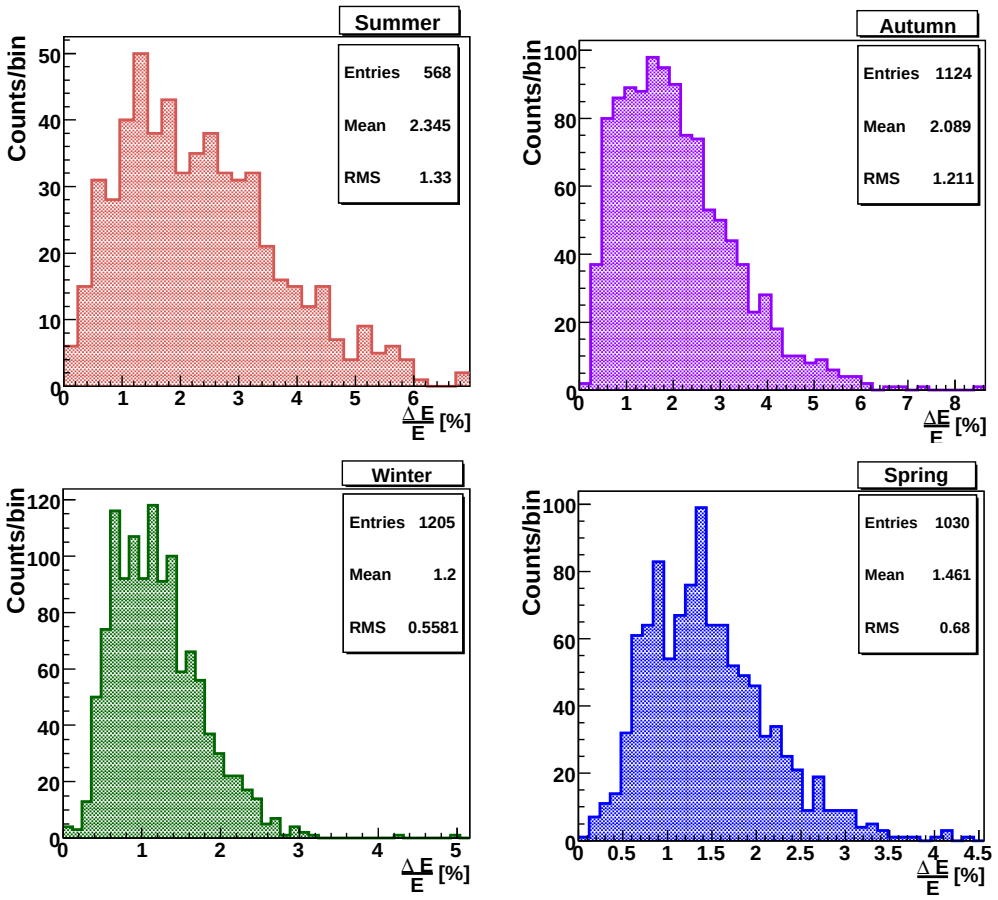

Figure 6.7.: Histograms of the relative shifts in energy for 3927 events spread out over the four seasons. The largest average shift was that for Summer, but the highest shift in energy here was for an event in Autumn.

6.7. Cloud Cover

The first step to investigate the possible effects of weather conditions on humidity profiles was to take a closer look at individual launches. A number of launches were identified as having large spikes in their humidity profiles, where the relative humidity peaked to 80 % or higher. In some cases a temperature inversion occurred at the same height. An example of this is shown in figure 6.5. These two artefacts can be indicative of a radiosonde passing through a layer of cloud. As the fluorescence detectors cannot operate during overcast conditions, it makes sense to remove launches conducted during overcast conditions if it can be shown that vapour pressure profiles are on average different depending on whether the sky is clear or overcast.

6.7.1. Identifying Overcast Days

Using the IR monitor at the CLF and the cloud cameras it is possible to identify the cloud conditions at the times of radiosonde launches. I chose to label the launches as either clear, overcast or undetermined, based on the information obtained either by one, or both of the instruments. It was not possible to classify the data from all launches, as the cloud cameras only became operational in April 2004 and the information from the IR vertical cloud monitor at the CLF is only available from April 2005. There are also some holes in these databases that meant that some of the more recent data could not be classified. These instruments are also only operational at night time, as this is when the fluorescence detectors are operating. As such, day-time profiles cannot be classified, and have been left out of this work. Whether or not data from day-time radiosonde launches should be included will be discussed later in section 6.9.

6.7.2. Statistics

Table 6.5 shows the number of launches that have been classified as being conducted on either clear or overcast nights, as well as those that could not be classified, either due to the lack of information from the atmospheric monitors, or if the conditions were determined to

be partly cloudy but not completely overcast. The main reason behind the large number of unclassified launches is the inclusion of launches conducted in the years prior to the implementation of cloud monitoring devices.

Table 6.5.: The number of radiosonde launches conducted on nights determined to be clear or overcast from each season, as well as the number which remain undetermined.

Season	Total	Clear	Overcast	Undetermined
Summer	20	8	5	7
Autumn	28	7	7	14
Winter	31	7	8	16
Spring	31	7	6	18

6.8. Comparing 'Cloudy' and 'Clear' Seasonal Profiles

To test whether data from radiosonde launches conducted during overcast conditions were on average different from those conducted during clear conditions, I created seasonal relative humidity profiles and vapour pressure profiles, using data collected only on clear nights, and data collected only on cloudy nights. The results for the Summer profiles are shown in figures 6.8 and 6.9.

On average, the relative humidity profile for the overcast data set is higher than for the clear data set, with two distinct peaks located at two common cloud heights. These are not observed in the clear profile. The difference between the clear and overcast vapour pressure profiles is not as large, but there is a definite reduction in the vapour pressure in the first kilometres when looking at the clear profile. Perhaps the most significant difference between the two is the reduction in the uncertainty associated with each of the vapour pressure profiles. Even though there were only 8 launches used to create the 'clear' summer vapour pressure profile, it's standard deviation is equal to that of the summer profile made up of all clear, overcast and undetermined launches, with 20 launches. It is quite clear that the large spread in the seasonal profiles is partly due to the fact that they are composed of two significantly different subsets of data; vapour pressure readings taken during either clear or overcast conditions.

From these observations, I have concluded that all radiosonde data from launches that were conducted during overcast conditions should be excluded. It is shown in figure 6.8 that the vapour pressure is systematically reduced within the first few kilometres. This height range is important, as roughly half of the integrated water vapour exists within $1-2\,\mathrm{km}$ (one scale height) of the ground.

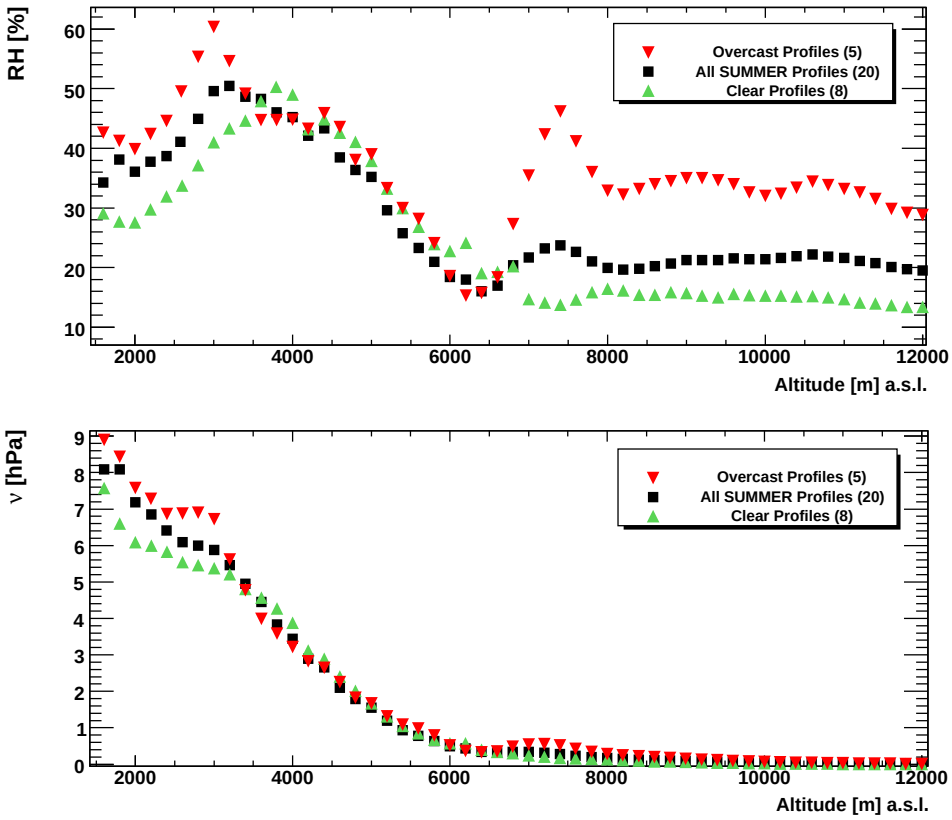

Figure 6.8.: The Summer clear and the Summer overcast relative humidity and vapour pressure profiles, plotted with the complete Summer seasonal profile, which includes clear, overcast and undetermined profiles. The relative humidity is shown in the top plot and the vapour pressure is shown in the bottom plot. The numbers next to the profile names in the legends indicate how many individual launches were used to create each average profile. It can be clearly seen that the relative humidity and vapour pressure profiles depend on whether the conditions are clear or overcast.

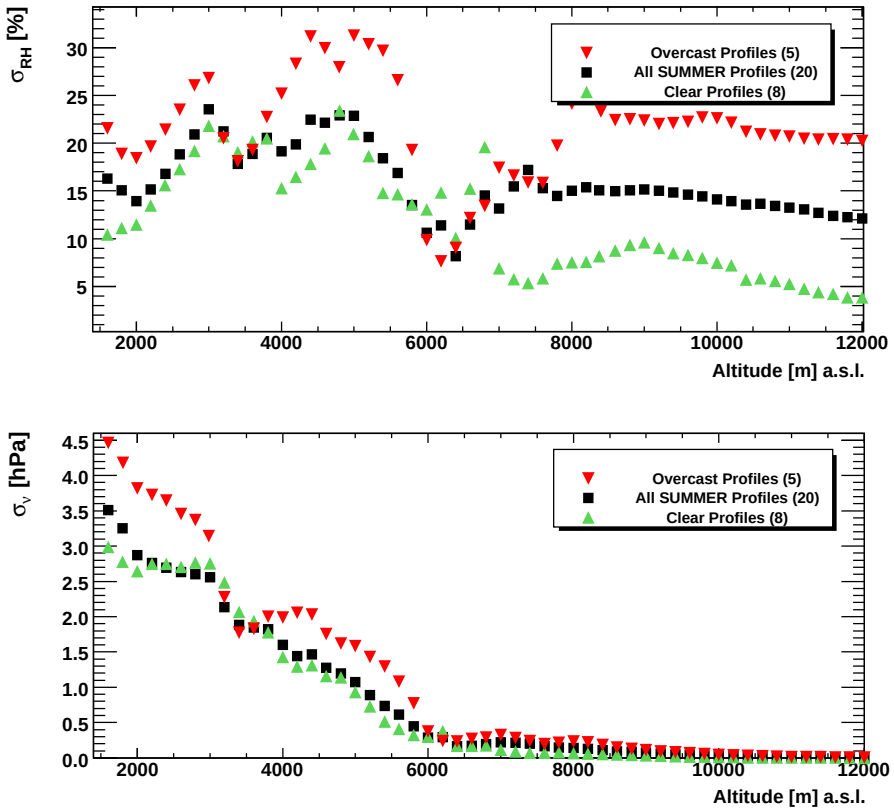

Figure 6.9.: The magnitude of the standard deviations of the summer clear and overcast relative humidity and vapour pressure profiles, plotted with those of the complete seasonal profiles, which includes data from launches classified as clear, overcast or undetermined. The uncertainty in the relative humidity is shown in the top plot and the uncertainty in the vapour pressure is shown in the bottom plot.

6.9. Discarding Day-time launches

Data from 277 ascents were available for creating the vapour pressure profiles at the time of this work. 162 of these were conducted between 9pm and 7am local time. As the fluorescence detectors only operate at night time, it needed to be checked whether there is a difference between day and night vapour pressure readings. This will determine whether the inclusion of day-time data will introduce a systematic shift in the profiles or if their exclusion will simply increase the statistical uncertainty.

There are definitely large temperature and relative humidity changes at ground level between day and night. While the resulting fluctuations in vapour pressure are much more subtle, a definite daily trend can be seen. This is illustrated in figure 6.10. The data shown on the left in this figure are all of the relative humidity readings from the weather station at the Los Leones FD for the month of March in 2006. On the right are the vapour pressures calculated from the relative humidity and temperature readings using equations 6.9 and 6.10.

Not only is it important to note if there is a difference between day and night vapour pressures on average, but the standard deviation on these average values is also important. This is because if there is a larger variation in vapour pressure during the day than at night, then not only would a systematic uncertainty be added by using day time values, but the statistical uncertainty could be increased. Table 6.6 lists the average day and night ground-level vapour pressures and the spread in the values. Night-time data are defined as those that are recorded between 0000 hrs UTC and 0959 hrs UTC, and day-time data are readings taken outside of this time frame.

The night-time vapour pressure is larger than the day time vapour pressure between September and April, and smaller between May and August inclusive. This shows that there is a yearly trend, in which day time vapour pressure profiles vary between being systematically larger and smaller than the night time profiles.

Another concern is the fact that the cloud conditions cannot be ascertained for these day-time launches. It has been demonstrated in section 6.8 that the overcast and clear vapour pressure profiles are systematically different, and hence identifying and excluding the data

Table 6.6.: Average monthly values of ground-level vapour pressure, for both day-time and night-time, as measured by the Los Leones weather station over 2005 and 2006. The night-time vapour pressure is larger between September and April, and smaller between May and August inclusive.

Month	N	$\langle$ v[hPa] $\rangle$ (night)	RMS	N	$\langle$ v[hPa] $\rangle$ (day)	RMS
January	5560	9.08	3.31	9465	8.28	3.06
February	5891	9.90	3.20	9751	8.87	3.10
March	6560	8.95	2.74	11031	8.35	2.78
April	6518	7.13	2.82	10958	7.12	2.91
May	6733	4.98	1.86	11325	5.04	1.74
June	6527	4.28	1.57	10981	4.74	1.77
July	6733	4.20	1.17	11337	4.56	1.45
August	6722	3.92	1.07	11296	4.09	1.22
September	6483	5.23	1.43	10781	5.19	1.61
October	6512	5.51	1.82	10907	5.05	1.93
November	6499	6.15	2.33	10913	5.66	2.29
December	4704	7.48	3.22	7987	7.023	2.86

from cloud-affected launches is important. Instead of including the day time profiles in the construction of vapour pressure profiles to increase statistics, I would recommend that the statistics should simply be increased by conducting future launches on clear nights to ensure that the vapour pressure profiles are both accurate and precise.

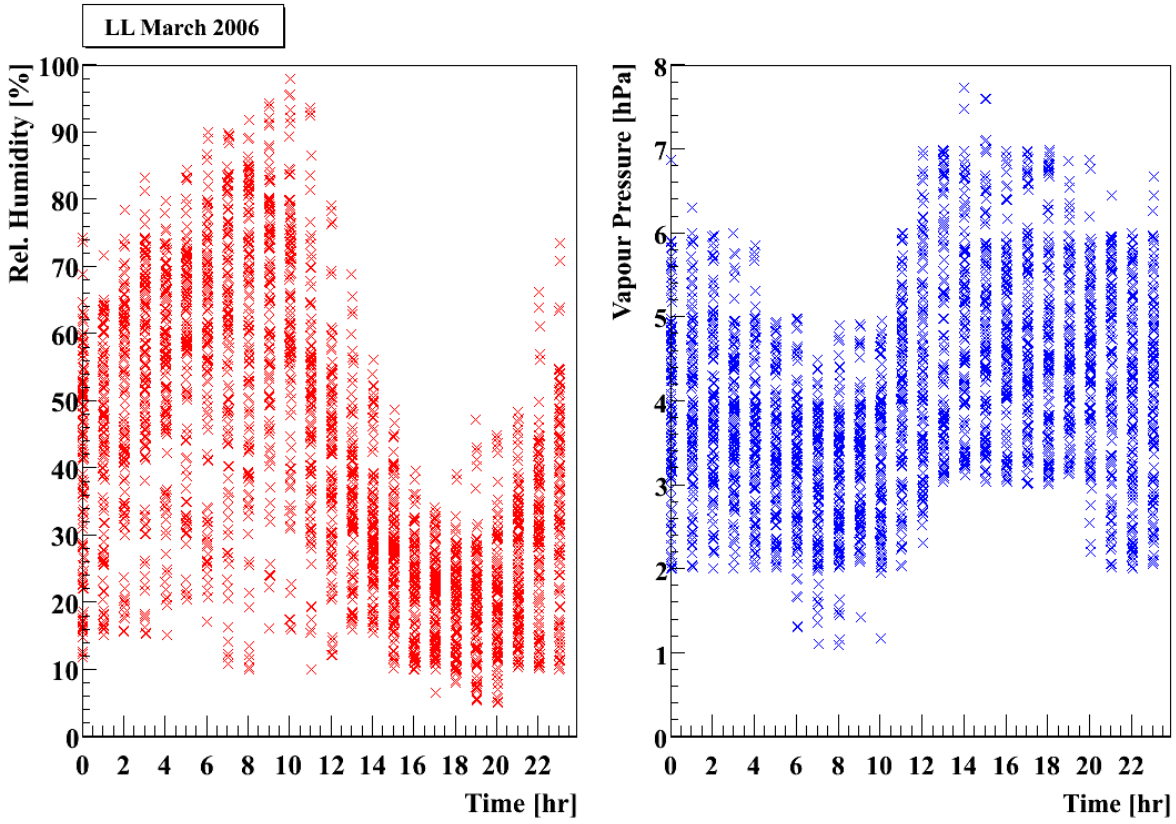

Figure 6.10.: Left: All relative humidity readings from the weather station at the Los Leones fluorescence detector site from March 2006, grouped into one hour blocks. Right: The value of the vapour pressure [hPa] calculated from the temperature and relative humidity readings using equations 6.9 and 6.10. Weather station readings are taken every 5 minutes. A definite daily trend can be seen here.

6.10. Creating Monthly Profiles

Due to my findings in section 6.9, I will continue to limit my work to only using data from launches conducted at night time. Also, based on the results of my comparison between clear and overcast vapour pressure profiles, data from any launches identified as having being conducted during overcast conditions will be excluded. Launches conducted at times when the weather could not be determined either by the infra-red cloud cameras or the vertical cloud monitor have been included.

The obvious next step is to see if the uncertainty in the vapour pressure profiles can be reduced by having monthly profiles rather than seasonal profiles. From table 6.6 it can be seen that the water vapour concentrations in the atmosphere can almost halve at ground level from March (9 hPa) to May (5 hPa), and yet the same seasonal vapour pressure profile would be applied to both.

6.10.1. Moving boxcar profile

Table 6.7 shows the number of launches available within each month to create the monthly profiles. Some months have very few launches, making it difficult to create monthly profiles for these particular months as the statistical uncertainty would become too large. One way to deal with this problem is to use a moving boxcar method.

Similar to the way that the seasonal profiles were created, in which three months of data were used to produce each profile, a moving boxcar method can be applied to use data from launches conducted in the previous and subsequent months to develop each monthly profile. For example, the March monthly profile would contain launch data from February, March and April, all with equal weighting.

6.10.2. Shift in reconstructed parameters

After replacing the seasonal vapour pressure profiles with the monthly profiles created here, the average effect of the vapour pressure on the shower reconstruction can be re-calculated, this time using the monthly vapour pressure profiles. As expected from the

Table 6.7.: Number of launches available from each month after overcast launches have been removed. Also shown are the number of launches used to create each monthly model using the boxcar method.

Month	No. of launches available	No. used in boxcar profile
January	3	15
February	11	23
March	9	25
April	5	21
May	7	13
June	1	16
July	8	23
August	14	28
September	6	24
October	4	27
November	17	22
December	1	21

vapour pressure profiles shown in figure 6.11, the shifts in energy and depth of shower maximum are largest for January, February and March. Table 6.8 lists the mean and the RMS of the relative shifts in energy and the absolute shifts in the depth of shower maximum for each month. While shifts in energy can reach 8-10% for showers which maximise close to the ground, these are extreme cases that occur for high energy vertical showers. Due to anti-bias cuts that have been applied to the data set that we used to test the impact of the monthly profiles, we do not have high energy showers with zenith angles of less than 20° included in our results.

6.10.3. Uncertainties in monthly profiles

The removal of the data from radiosondes launched during overcast conditions caused systematic shifts in the average vapour pressure profiles as well as a reduction in the uncertainty in the average profiles. Despite this the uncertainty in the profiles is still quite large (see figure 6.12). This is especially notable within the first few kilometres above the ground. Most of this appears to be due to the large natural variations in the vapour pressure at the ground, and these propagate through to greater heights.

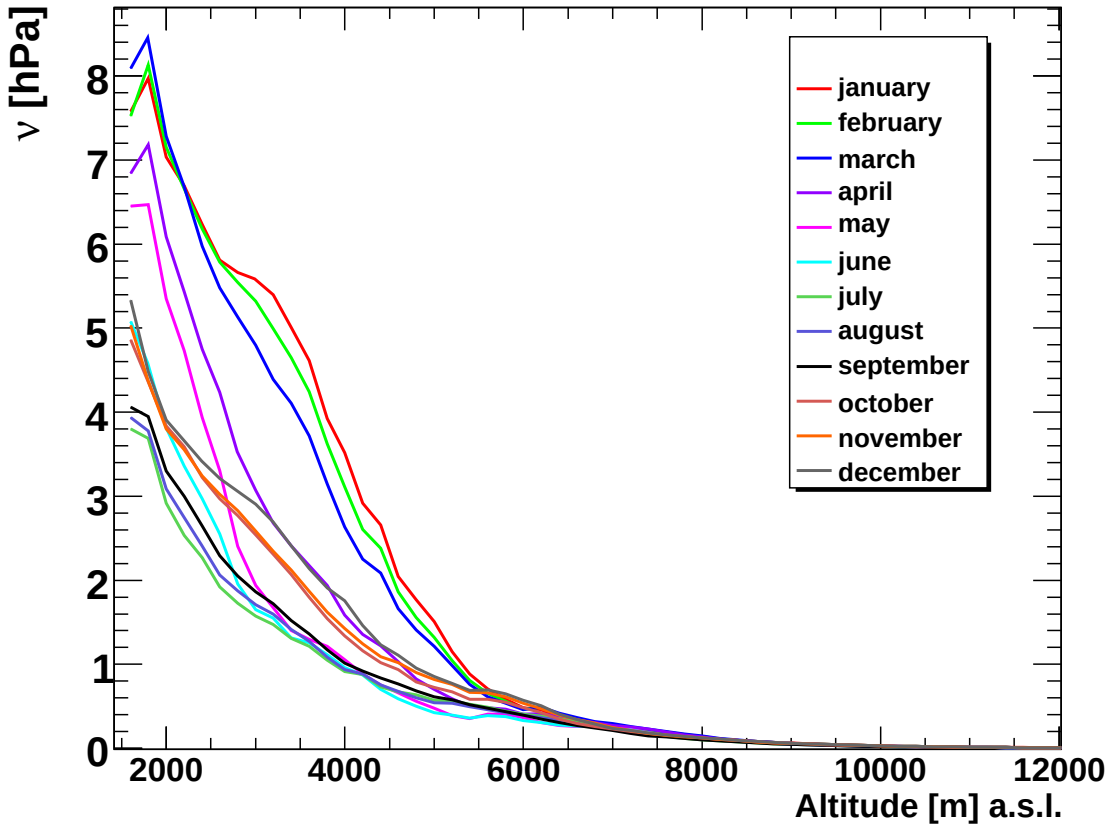

Figure 6.11.: Here the monthly vapour pressure models created using the moving boxcar method are shown. The number of launches used to create each profile can be found in Table 6.7.

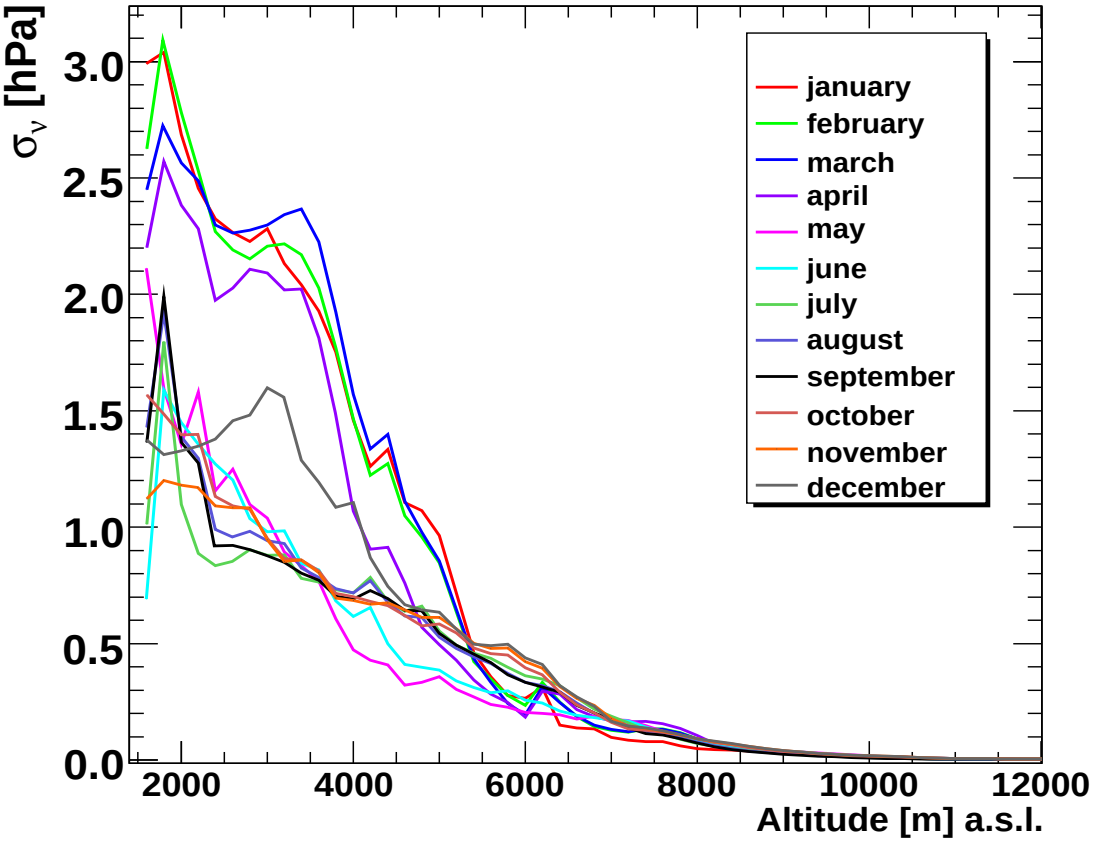

Figure 6.12.: Here the magnitude of the standard deviations on the monthly vapour pressure models presented in Figure 6.11 are shown. The number of launches used to create each profile can be found in Table 6.7.

Table 6.8.: Average shifts in energy and X_{max}, as well as the RMS of the distributions, as the result of using the monthly vapour pressure models in the event reconstruction. The shifts are with respect to not using the humidity correction.

Month	$\frac{\Delta E}{E}$[%]	RMS	$\Delta\ X_{max}\ [\frac{g}{cm^2}]$	RMS
December	1.7	0.8	2.9	1.2
January	2.8	1.4	5.7	2.8
February	2.8	1.5	5.5	2.8
March	2.6	1.4	4.9	2.5
April	2.0	1.1	3.5	1.9
May	1.6	1.0	2.4	1.7
June	1.3	0.6	1.9	1.2
July	1.1	0.5	1.6	0.6
August	1.2	0.5	1.8	0.8
September	1.3	0.6	2.0	0.9
October	1.5	0.7	2.4	1.1
November	1.6	0.7	2.6	1.1

6.11. Including the effect of temperature dependent collisional cross-sections into the fluorescence yield

Referring back to equation 2.3, the temperature dependence of the collisional cross sections can be included by introducing the factor $\frac{H_\lambda(T_0)}{H_\lambda(T)}$, which was set to 1 for the humidity dependence study. Here, for the temperature dependence study by AIRFLY [105], dry air has been used, and the fluorescence yield measurements were taken in the temperature range 240 K to 310 K.

The data were fitted with the function;

$$\frac{H_\lambda(T_0)}{H_\lambda(T)} = \left(\frac{T}{T_0}\right)^{\alpha_\lambda} \tag{6.11}$$

and the values of α_λ are listed in table 6.9. These values show that there is a significant temperature dependence when comparing the values to the usual assumption that $\alpha_\lambda = 0$. There is also a wavelength band dependence with the 391.4 nm band differing significantly from the other measurements.

Table 6.9.: Measurement of temperature dependence parameters for a selected group of air fluorescence bands by the AIRFLY Collaboration[105].

NOTE:
This table is included on page 110 of the print copy of the thesis held in the University of Adelaide Library.

6.11.1. Shift in reconstructed parameters

The shifts in energy and depth of shower maximum are illustrated in figure 6.13. The shift in energy is a positive shift of approximately 4.5%. As the fluorescence yield had been

over-estimated at temperatures below $20°C$ before the temperature correction had been put in place, the energy deposited was underestimated. At lower temperatures, fewer photons are produced per unit of energy deposited into the atmosphere. The shift in X_{max} is approximately -5 g cm^{-2}. This is because the effect of the correction became larger the further the temperature deviated from the temperature at which the collisional cross sections were originally calculated ($20°C$). Hence the depth of shower maximum was shifted to slightly higher altitudes.

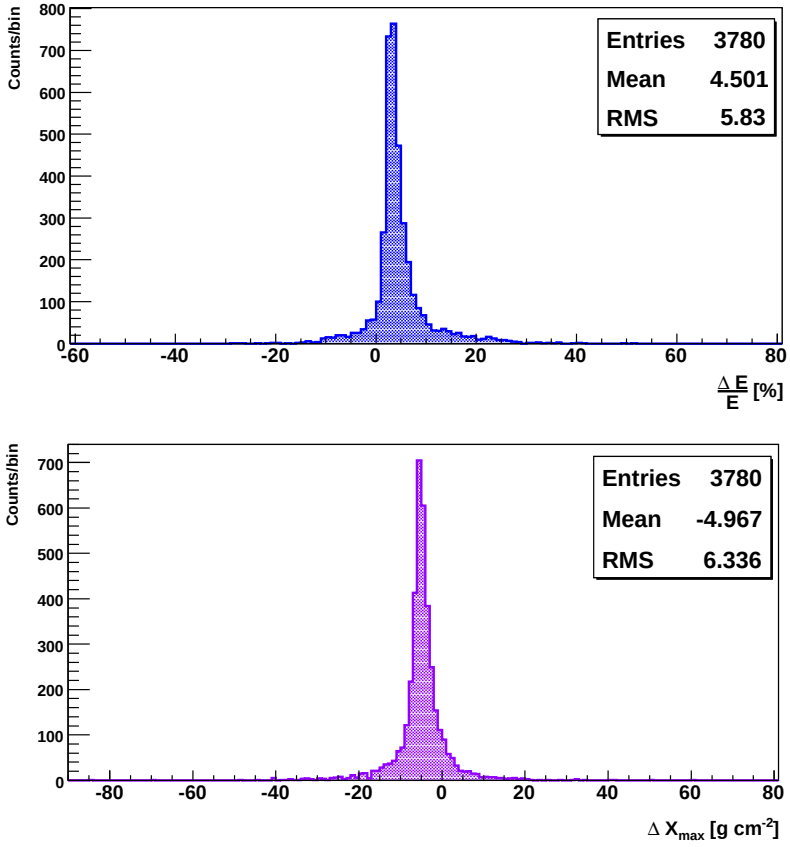

Figure 6.13.: The change in the reconstructed energy and depth of shower maximum of 3780 events, as the result of taking temperature into account in the quenching calculations.

Figures 6.14 and 6.15 show the shifts in the reconstructed energy and depth of shower maximum as a function of energy for 3,780 events.

The effect on the reconstructed energies is largest for high energy showers, as it was for

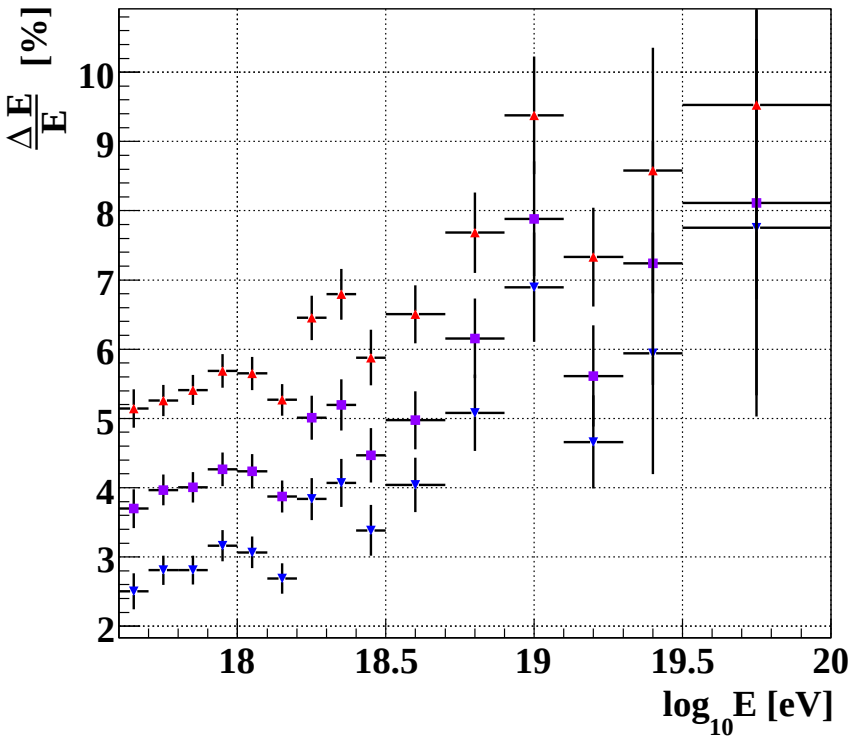

Figure 6.14.: The change in the reconstructed energies of 3780 events as a function of energy. The band containing approximately 90% of the data is indicated by the red and blue markers which are the mean values plus or minus two standard deviations.

the vapour pressure correction.

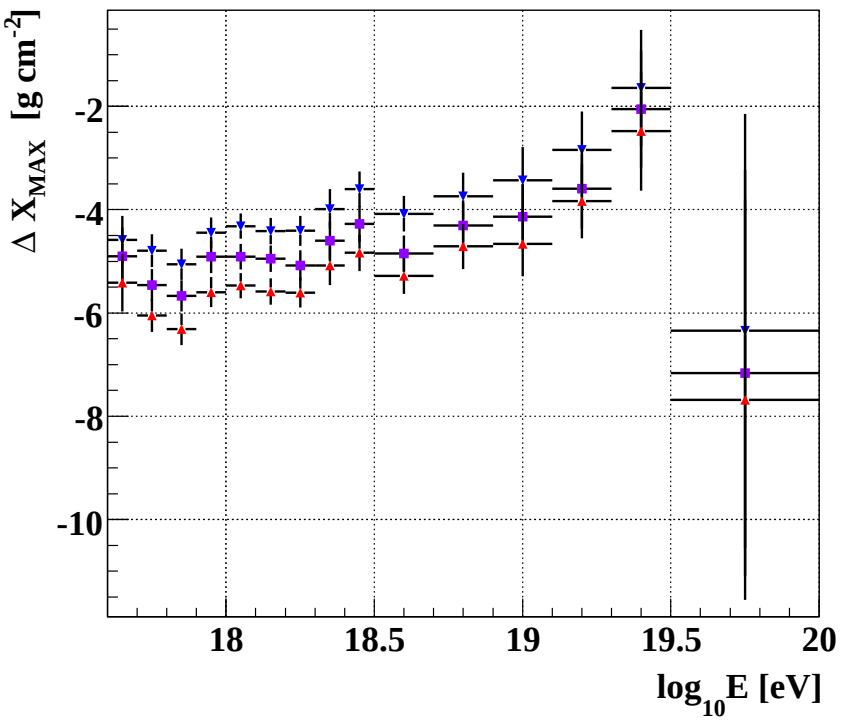

Figure 6.15.: The change in the reconstructed depth of shower maximum of 3780 events as a function of energy. The band containing approximately 90% of the data is indicated by the red and blue markers which are the mean values plus or minus two standard deviations.

6.11.2. Overall changes to Reconstruction of Hybrid Showers

The corrections for collisional quenching by water vapour, and the temperature dependent cross sections led to an increase in the reconstructed energy of the events. However, as the humidity correction is largest near the ground, whereas the temperature correction is at its largest far above the ground, they have opposite effects on the depth of shower maximum. The vapour pressure correction deepens X_{max}whereas the temperature correction makes it shallower.

6.12. Techniques for reducing uncertainties on Vapour Pressure Profiles

While the monthly models are capable of predicting the vapour pressure profile on most clear nights, outliers do occur. As can be seen by looking at the monthly vapour pressure models, not only does the average value at the ground change on a yearly cycle but so does the scale height of the variation in vapour pressure.

6.12.1. Re-scaling monthly models

One way in which the vapour pressure profiles could be improved would be re-scaling the profiles using measurements of the vapour pressure at the ground from the weather stations located at each fluorescence detector as well as at the centre of the array. This also changes the uncertainty in the monthly vapour pressure profiles, as the uncertainty in the measurement of the vapour pressure at the ground is very small. One thing that should also be checked here is the lateral homogeneity of vapour pressure readings at the ground over the whole array. As showers can land tens of kilometres away from any given weather station it is important to check the average difference between the vapour pressure calculated using different weather station readings of temperature and relative humidity.

Figure 6.16 shows the difference between the vapour pressure calculated using temperature and relative humidity measurements from the weather stations at Los Leones and at the

CLF in the middle of the array. Comparing over 11,000 pairs of measurements, it shows that there is no systematic difference between the weather station measurements of vapour pressure at the two sites.

As quoted in table 6.2 in subsection 6.3.1, the weather station uncertainties associated with measuring the relative humidity and temperature are 2% and 0.4° respectively. This then gives us the uncertainty in the vapour pressure as

$$(\sigma_\nu)^2 = \left(\frac{\partial \nu}{\partial RH}\right)^2 (\sigma_{RH})^2 + \left(\frac{\partial \nu}{\partial T}\right)^2 (\sigma_T)^2 \tag{6.12}$$

$$(\sigma_\nu)^2 = \left(a\, e^{\left(\frac{bT}{c+T}\right)}\right)^2 (\sigma_{RH})^2 + \left(RH\, a\, e^{\left(\frac{bT}{c+T}\right)} \frac{bT}{(c+T)^2}\right)^2 (\sigma_T)^2 \tag{6.13}$$

where $a = 6.1078$, $b = 17.08085$ and $c = 234.15$ for T ≥ 0°C, and $a = 6.10714$, $b = 22.44294$ and $c = 272.44$ for T<0°C, as stated in equations 6.9 and 6.10. Propagating these errors through, the uncertainty in the vapour pressure at the ground as a function of temperature for a relative humidity of 100 % is shown in figure 6.17. We assume the instrumental uncertainties for temperature and relative humidity given in [109].This uncertainty remains under 1 hPa even for extreme humidity levels. This is smaller than the uncertainty associated with the monthly models at ground level. We can also see that the uncertainties associated with the equipment used to measure the atmospheric parameters is comparable to the average differences in vapour pressure over the entire array.

The next step is to see how knowing the vapour pressure at the ground will affect the uncertainties at different heights. Each vapour pressure profile can be approximated by an exponential function for which we require the vapour pressure at the ground, and the scale height of the water vapour H.

$$\nu(h) = \nu_g e^{-\frac{(h-h_g)}{H}} \tag{6.14}$$

where h_g is the altitude of the weather station that provides the value of ν_g, h is the altitude at which the vapour pressure is being calculated, and H is the scale height of

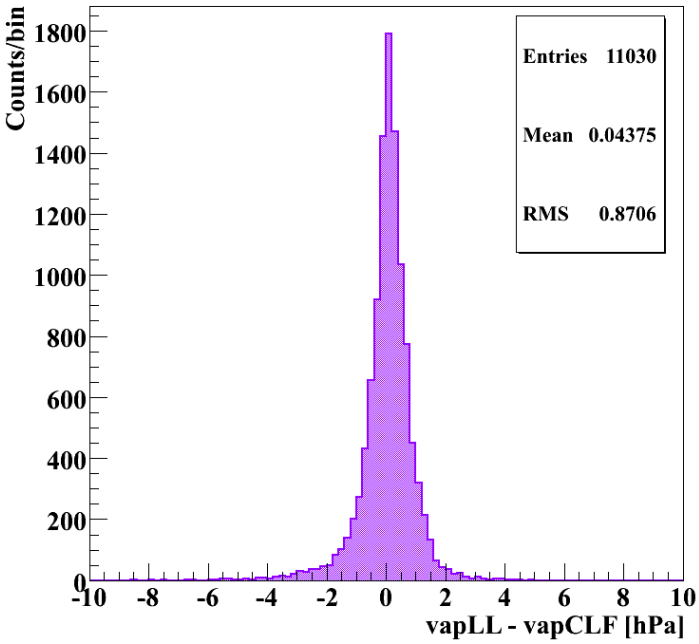

Figure 6.16.: The difference in the measurements of vapour pressure at the weather station located at Los Leones compared to that in the middle of the array at the CLF. There is no systematic difference between measurements at the two sites.

water vapour coming from exponential fits to the monthly models. We can then find the uncertainty by adding the uncertainties of the vapour pressure at the ground and the scale height in quadrature:

$$\sigma_\nu^2 = \left(\frac{\partial \nu}{\partial \nu_g}\right)^2 (\sigma_{\nu_g})^2 + \left(\frac{\partial \nu}{\partial H}\right)^2 (\sigma_H)^2 \tag{6.15}$$

$$\sigma_\nu^2 = \left(e^{-\frac{(h-h_g)}{H}}\right)^2 (\sigma_{\nu_g})^2 + \frac{(h-h_g)}{H^2}\left(\nu_g e^{-\frac{(h-h_g)}{H}}\right)^2 (\sigma_H)^2 \tag{6.16}$$

Here the temperature and relative humidity are taken to be independent parameters. The uncertainty in the vapour pressure at the ground σ_{ν_g}, comes from the RMS of the lateral homogeneity at the ground, which was 0.87 hPa from figure 6.16, and the uncertainty in

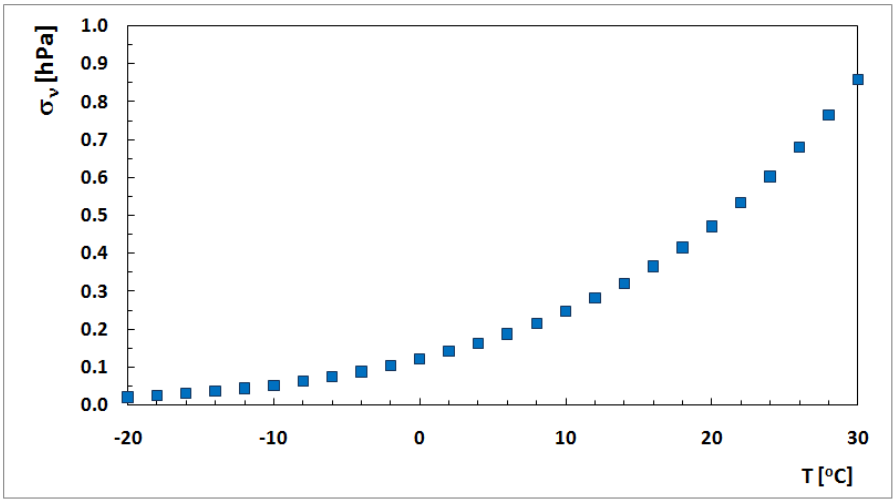

Figure 6.17.: This figure shows the uncertainty in vapour pressure calculations as a function of temperature for 100% relative humidity. This is calculated using the instrumental uncertainty in weather station measurements listed in table 6.2, and equations 6.9 and 6.10 for the vapour pressure.

the measurement of the vapour pressure which comes from the instrumental errors quoted in table 6.2 being propagated through equations 6.9 and 6.10. As the average temperature and relative humidity at the ground is different for each month, the uncertainty in the vapour pressure at the ground will also be different on a monthly basis. This is then added in quadrature with the RMS of the lateral homogeneity at the ground (0.87 hPa). These are listed in table 6.10.

The uncertainty in the scale height σ_H, is taken as the RMS of the scale heights from each of the individual launches used in each month's vapour pressure profiles. The scale height $\overline{H}$, is simply the average of the scale heights for the launches used to make up each monthly profile.

Figures 6.18, 6.19 and 6.20 show the standard deviation of the original monthly models compared to the re-scaled monthly models. For all months, the rescaled monthly models have equal or smaller standard deviations for roughly the first 6km above sea level, and dramatically reduce the uncertainty near the ground in the summer months.

This method can easily be implemented into the reconstruction procedure, with the weather station data being extracted from the database to give the vapour pressure at the

Table 6.10.: The uncertainty in the vapour pressure at the ground for each month, calculated by adding the RMS of the lateral homogeneity to the instrumental uncertainty in measuring the vapour pressure at the ground. The average temperatures and the relative humidities were calculated using data from 2004 - 2008, from between 00:00 UTC and 09:59 UTC.

Month	$\overline{T}$[K]	$\overline{RH}$[%]	$\overline{\nu}$[hPa]	σ_{ν_g}[hPa]
January	16.2	47	8.764	0.946
February	15.4	64	11.273	0.938
March	13.0	59	8.919	0.921
April	8.2	64	6.965	0.897
May	3.0	69	5.190	0.883
June	1.2	67	4.482	0.881
July	1.3	72	4.836	0.881
August	2.7	69	5.092	0.883
September	5.2	55	4.863	0.888
October	7.9	51	5.425	0.896
November	11.2	51	6.731	0.910
December	14.6	42	7.065	0.932

Table 6.11.: The average scale height $\overline{H}$[km] found by fitting an exponential to each individual vapour pressure profile used in creating the monthly models. The uncertainty in the scale height is the RMS of the launches used to calculate these averages. The third column presents the relative uncertainties.

Month	$\overline{H}$[km]	σ_H[km]	$\frac{\sigma_H}{\overline{H}}$ [%]
January	2.096	0.432	20.6
February	1.945	0.393	20.2
March	1.752	0.419	23.9
April	1.471	0.399	28.3
May	1.300	0.377	29.0
June	1.459	0.413	28.3
July	1.615	0.461	28.5
August	1.645	0.436	26.5
September	1.712	0.429	25.1
October	1.973	0.378	19.2
November	2.053	0.399	19.4
December	2.101	0.471	22.4

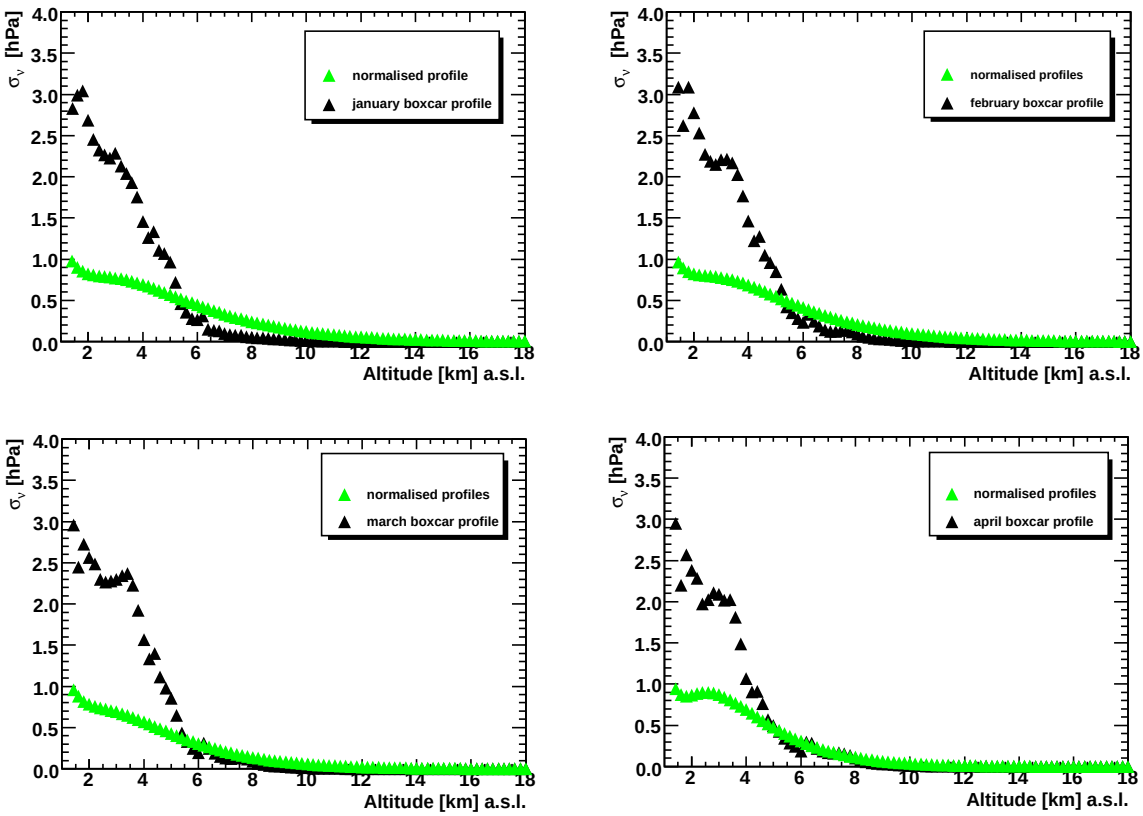

Figure 6.18.: Comparing the standard deviations from the original monthly profiles for January, February, March and April, with the same profiles normalised to the ground.

ground as well as the uncertainty in this value. The scale heights and their uncertainties would be the monthly averages quoted in table 6.11. These two values could then be used to create the exponential vapour pressure profile. It should be noted that this would only be a valid method for clear nights, as during overcast conditions, the vapour pressure profile does not approximate an exponential. While the uncertainty in the vapour pressure at the ground cannot be known to a greater accuracy, improvements could possibly be made on the uncertainty in the scale height.

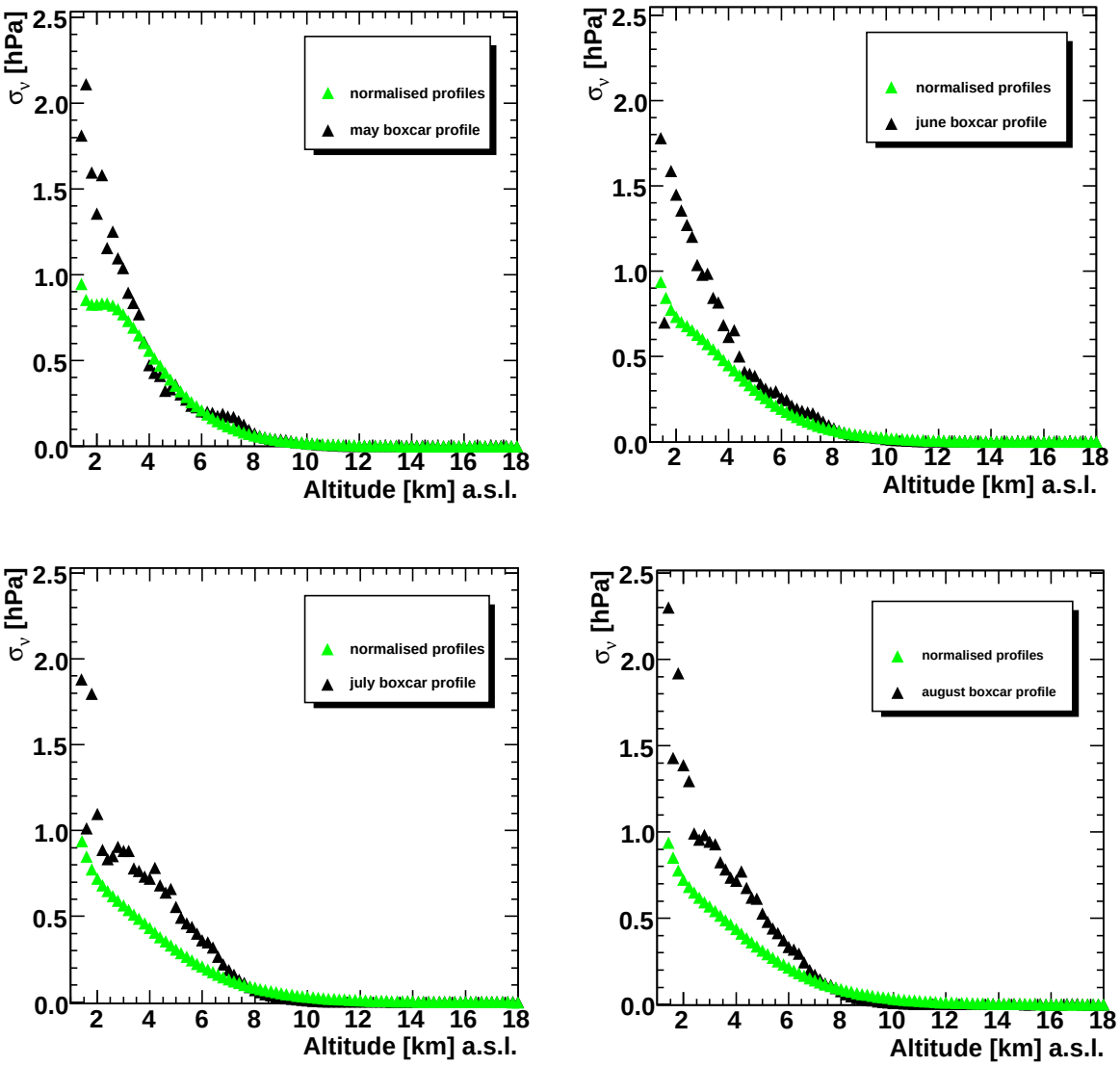

Figure 6.19.: Comparing the standard deviations from the original monthly profiles for May, June, July and August, with the same profiles normalised to the ground.

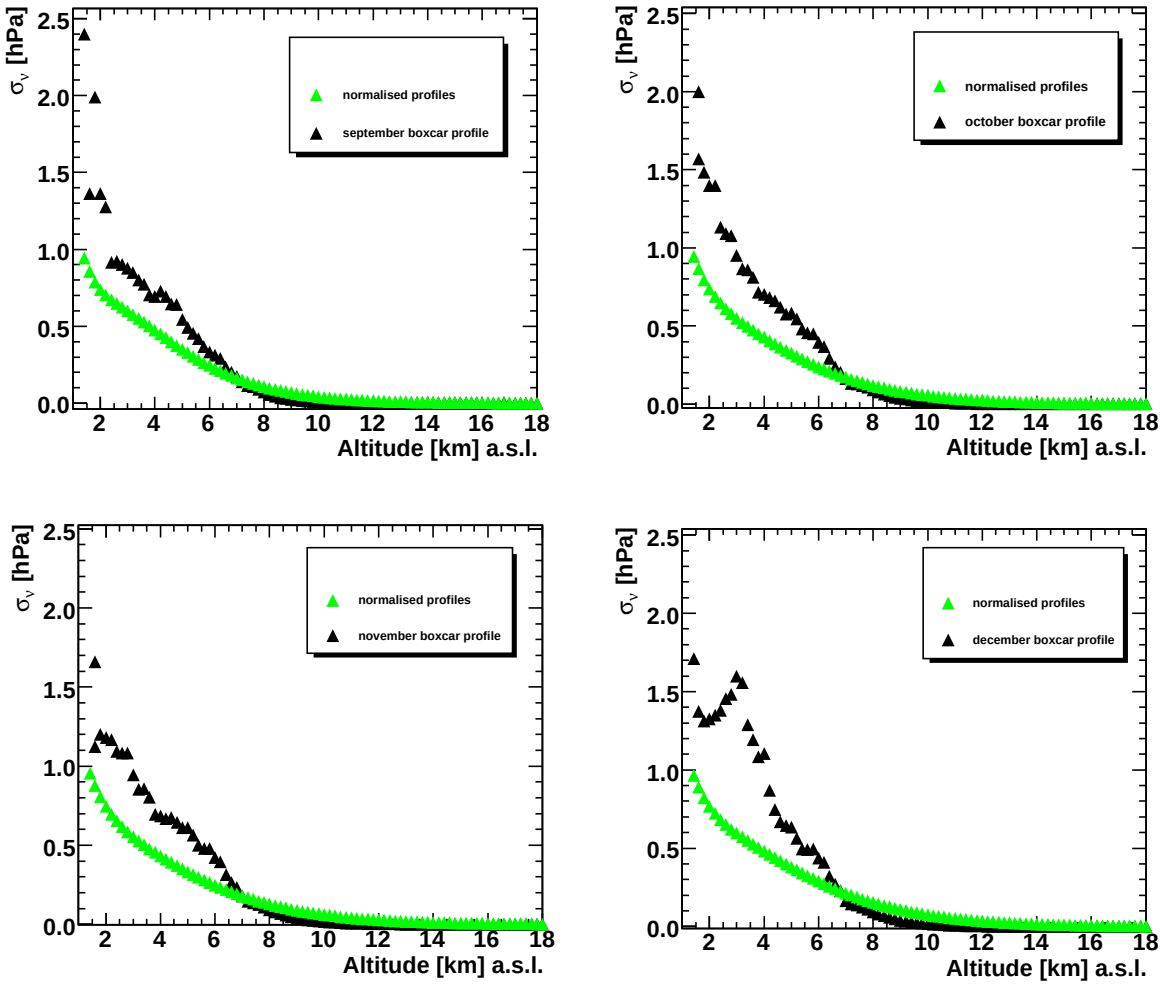

Figure 6.20.: Comparing the standard deviations from the original monthly profiles for September, October, November and December, with the same profiles normalised to the ground.

6.12.2. Using sky temperature measurements

As introduced in subsection 6.3.3, an infra-red detector can be used to measure the temperature of the sky.

The infra-red brightness of clouds is greater than that of clear sky at night time, allowing overcast conditions to be identified by using an infra-red detector centred at a wavelength of 10 μm. This is not always true when pointing the detector close to the horizon. However, data used in this study all comes from a single pixel directed vertically.

Infra-red detectors can also be used to measure the integrated water vapour. This is because water vapour emission wavelengths are within the bandpass of the detectors. Therefore the integrated vapour pressure can be determined by finding a relationship between the sky temperature measured by the IR detector, the vapour pressure at the ground and the temperature at the ground.

Maghrabi's Doctorate Thesis [121] discusses this idea in detail, and his work has determined a factor in terms of the sky and ground temperatures, which when plotted against the total integrated water vapour, yields a correlation. This is only applicable for clear skies, and for the vertical sky temperature.

The Maghrabi Factor is given by:

$$MF = T_{sky} + 31.1 - 0.417\,T_{ground}\ [^{\circ}C] \tag{6.17}$$

Both the sky temperature and the ground temperature (in $^{\circ}C$) are measured at the CLF, with the sky temperature coming from a single pixel that records the infra-red radiation from the sky at zenith.

Figure 6.21 shows the Maghrabi factor calculated using temperature measurements taken at the time of 38 launches, plotted against the square-root of the vapour pressure at ground multiplied by the scale height of the vapour pressure, $\sqrt{\nu_g H}$.

This factor comes from integrating equation 6.14 over all heights, from which we receive $\nu_g H$, the total integrated water vapour. The square root is simply an experimentally observed form of the correlation.

The vapour pressure at ground was taken from the CLF weather station, and the scale heights came from fitting exponential functions to the vapour pressure profiles calculated for each launch. No errors are presented here, as the instrumental error in determining temperature and relative humidity are too small to see on the plots. Also, the launch data errors are non-existent due to instrumental error being quoted as very small, and hence there are no accurate measures of uncertainty on the fitted exponential functions used to find the scale height. The cloud cover was determined for the time of each of the launches, and they were either classified as clear, patchy cloud or overcast. As can be seen in the plot, the launches conducted under clear conditions show a good linear relationship between the Maghrabi factor and $\sqrt{\nu_g H}$, whereas the launches conducted during overcast conditions do not follow the same correlation.

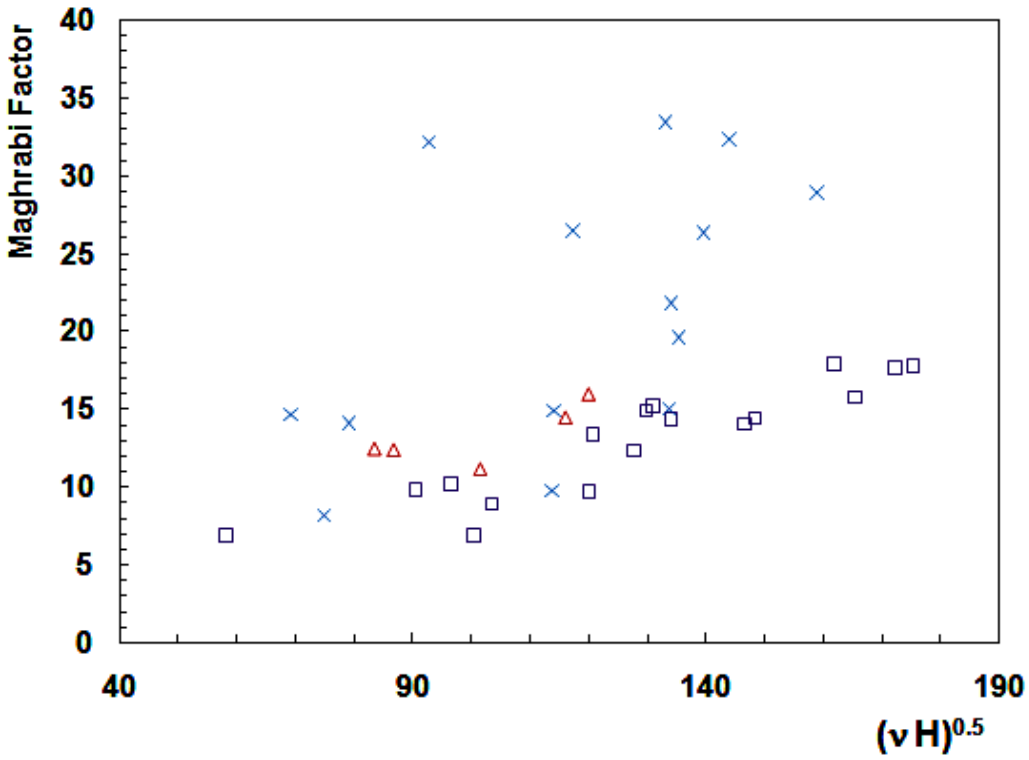

Figure 6.21.: Plotted here is the Maghrabi factor for 38 launches plotted against the square-root of the vapour pressure at ground multiplied by the scale height of vapour pressure measured by each individual launch. Nights classified as clear are represented by squares, patchy cloud by triangles and overcast by crosses.

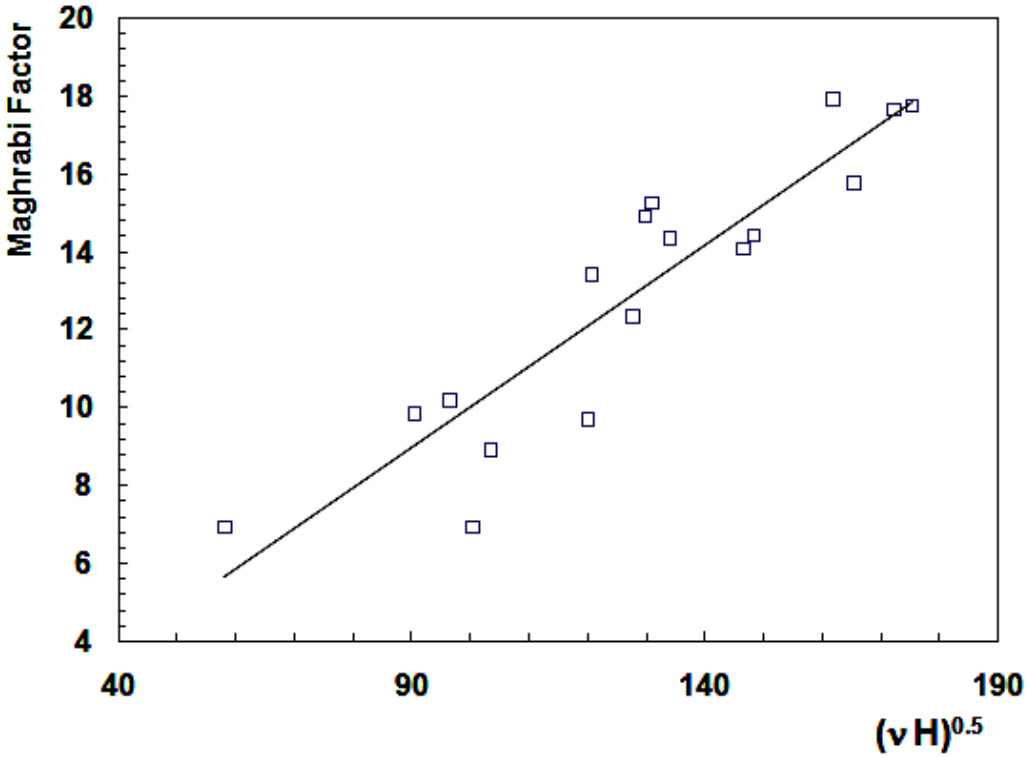

Figure 6.22.: Plotted here is the Maghrabi factor for launches conducted on nights determined to be clear, plotted against the square-root of the vapour pressure at the ground multiplied by the scale height of vapour pressure determined for each individual launch.

Figure 6.22 shows only the data points coming from 'clear' launches, to which a straight line has been fitted. Once again, without errors it is difficult to quantify the correlation, but what this shows is that by using temperature and relative humidity readings at the CLF, and the temperature of the sky above the CLF, we can determine the ground vapour pressure and the vapour pressure scale height. These two quantities then produce vapour pressure profiles that can be recalculated every-time weather station readings are taken, which is at 5 minute intervals.

The following three equations show explicitly how the scale height of the vapour pressure profile can be determined using measurements from a weather station and an infra-red detector.

$$MF = a + b\sqrt{\nu_g H} \tag{6.18}$$

$$T_{sky} + 31.1 - 0.417\,T_{ground} = a + b\sqrt{\nu_g H}$$

$$H = \frac{(T_{sky} + 31.1 - 0.417\,T_{ground} - a)}{b^2\,\nu_g} \tag{6.19}$$

The uncertainty in the value of the scale height would come from the uncertainty in the correlation. Due to the low statistics presented here, a definitive conclusion on how much of an improvement this method would introduce cannot be made. But even with the small number of events used to find the correlation, the resulting uncertainty in the scale height was approximately 500 m once the vapour pressure at the ground had been determined. This value is comparable to the uncertainties in scale height listed in table 6.11 which were calculated from fitting exponential functions to radiosonde data.

6.13. Conclusion

I have presented several approaches to creating vapour pressure profiles, utilising combinations of data from radiosonde launches and various atmospheric monitoring devices. I have shown that removing radiosonde data taken during overcast conditions systematically shifts the vapour pressure to lower values within the first few kilometres above ground, and reduces the uncertainty on the average profiles. Due to low statistics, data from radiosonde launches conducted on nights when information on the atmospheric conditions could not be obtained were included in the average vapour pressure profiles. It has been determined that excluding the daytime profiles is preferable to their inclusion, as none of these can be classified as being conducted during clear or overcast conditions. They also show a small systematic difference to night time conditions on average. These differences only occur near ground level, but this is where the vapour pressure and its uncertainty are at their greatest.

Using vapour pressure measurements from the weather stations to rescale the monthly vapour pressure profiles greatly reduces the uncertainty on the profiles for the first few kilometres above the ground. The method of using the sky temperatures along with the weather station data to determine the scale height of water vapour and hence create a simple exponential profile every 5 minutes is promising, but further statistics are required to decide if this would be a better option than changing the normalisation and using an average scale height.

After this work was conducted, the Global Data Assimilation System (GDAS) started to be used by Auger collaborators [122]. Data are taken every three hours and there is available data dating back to June 2005.

This resolves many of the issues addressed here as the GDAS vapour pressure profiles appear to be good matches to the Auger radiosonde data on average. While the balloon launches remain the most accurate way to measure the height-dependent atmospheric parameters above the Southern Auger site, GDAS is a cost-effective alternative that is able to provide up-to-date and reliable measurements.

7. Residual light

This Chapter addresses the process of light collection at the Fluorescence Detectors and the interpretation of that light. Both fluorescence and Cherenkov photons are received at the detectors, some of which have travelled directly from the point of emission on or around the shower track, and some that have suffered multiple Rayleigh and aerosol scatters before arriving at the detector. How this light is collected, and how it is interpreted, affects the shape and magnitude of the longitudinal shower profile. This has a direct effect on the reconstructed shower energies and depths of shower maximum. The work here identifies a halo of light around shower tracks on the FD cameras and works to determine the source of this light. Finally, the halo is parametrised and accounted for in the reconstruction process.

7.1. Lateral Width

At any given time, the photons that make up the shower image originate from a range of shower ages [123], illustrated by surface S in figure 7.1. They are defined as the photons which arrive at the FD during the time interval Δt. Within Δt, the shower front moves down the shower axis a distance $\Delta L = R\Delta\chi$, where $\Delta\chi$ is the change in the shower position during Δt, and R is the distance from the shower to the FD. Therefore we obtain an elemental volume ΔV from which the photons originate, and the number of photons is given by:

Figure 7.1.: Geometry of an EAS as seen by the fluorescence detector. Photons which arrive simultaneously at the FD originate from surface S.[124]

$$dN_{\gamma}^{rec} \mid_{\Delta V} = f(X,r) dS \frac{A}{4\pi R^2} \int T(\lambda)\eta(\lambda) d\lambda \tag{7.1}$$

where $f\,(X,r)$ is the light distribution as a function of slant depth X, and radial distance from the shower axis r. A is the light collecting area of the detector, $\eta(\lambda)$ is the normalised fluorescence spectrum, $T(\lambda)$ is the light propagation transmission factor and dS is the projection of the surface $r\Delta\phi\Delta r$ onto a plane perpendicular to the direction of the shower axis.

The photons $dN_{\gamma}^{rec} \mid_{\Delta V}$, form an instantaneous image on the camera $f_{\gamma}(\alpha)$ given by

$$f_{\gamma}(\alpha) = \frac{dN_{\gamma}^{rec} \mid_{\Delta V}}{\alpha d\alpha d\phi}, \tag{7.2}$$

where α is the angle between the direction to the centre of the image spot and the direction to ΔV, and ϕ is the azimuth angle in the plane of the camera. The size of the shower

image is defined as the minimum angular diameter α of the image spot containing a certain fraction $F(\alpha)$ of the total light recorded by the FD. If we assume that the shower width at the shower is not affected by absorption and scattering during its propagation to the detector, then we can determine $F(\alpha)$ by calculating $F(r)$, which is the fraction of light within a distance r of the shower axis.

$$F(\alpha) \equiv \int f_\gamma(\alpha')\, 2\pi\alpha' d\alpha' \sim \int f(r')\, 2\pi r' dr' \equiv F(r) \tag{7.3}$$

Here $f(r)$ is the normalised lateral distribution of fluorescence light, referred to as the shape function. Finally, the lateral width of the shower is given by

$$F(r^*) = 1 - (1 + a(s)\, r^*)^{-b(s)}, \tag{7.4}$$

where s is the shower age, initially introduced in section 3.3.

The parameters $a(s)$ and $b(s)$ were determined using Monte Carlo simulations of extensive air showers, and the details can be found in [125].

The parameter r^* is equal to the distance r from the shower axis, divided by r_M the Molière radius. The lateral width will be discussed further in Chapter 8.

7.2. Atmospheric Transmittance

In the ultra-violet (UV) band, attenuation through different forms can be placed in order of importance (i.e. the weight of their effect on the transmission of the fluorescence through the atmosphere). These are Rayleigh scattering, aerosol scattering and absorption. They will be discussed here with relevance to the 300-400nm wavelength band.

7.2.1. Rayleigh Scattering

The most important type of scattering that needs to be considered in this work is Rayleigh scattering. For the fluorescence and Cherenkov light, this is the scattering of the photons

by the molecular atmosphere. It applies when the particle sizes are smaller than approximately one tenth of the photon's wavelength. The cross-section is proportional to λ^{-4}, so shorter wavelengths are more readily scattered. The scatters are considered to be elastic although slight changes in the wavelength of the photons may be caused by scattering off an excited vibrational state of a molecule (increases the photon's energy) or by exciting a vibrational mode in the molecule (decreases photon energy). The scatters that result in a change in the photon's energy are called Raman scatters.

The angular distribution of Rayleigh scattering is given by equation 7.5.

$$\frac{d\sigma}{d\Omega} \propto 1 + cos^2\theta \tag{7.5}$$

It has a very slow angular dependence where θ is the angle between the scattered photon's initial and final direction.

7.2.2. Aerosol Scattering

Aerosol scattering is the scattering of photons by large molecules and compounds such as dust, water vapour and man-made aerosols. It is extremely difficult to model as the scattering angle has a large dependence on the aerosol's size (illustrated in figure 7.2), shape and dielectric constant. Also, aerosol contents can vary significantly in concentration and composition over short time scales. The size distribution of aerosols varies with height and weather conditions. The majority of aerosols are concentrated near the ground, and their distribution is often well described by an exponential with a typical scale height of $1-2\,\mathrm{km}$.

The dependence of the differential scattering cross-section per solid angle on the scattering angle is shown in equation 7.6. Once again θ is the angle between the scattered photon and the initial photon directions, and C and D are constants which are on average equal to 8.9×10^{-5} and 2.14 respectively [126].

$$\frac{d\sigma}{d\Omega} \propto e^{-D\theta} + Ce^{D\theta} \tag{7.6}$$

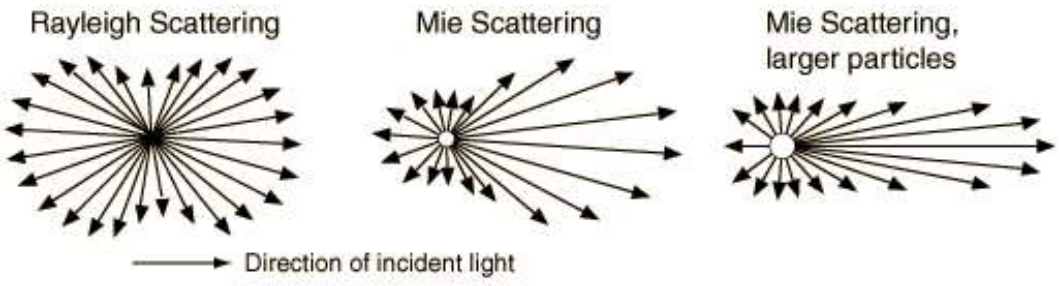

Figure 7.2.: This illustration shows the scatting of photons by particles of different sizes. The term 'Mie scattering' is an alternate name for aerosol scattering in the case of spherical aerosols. The relative size of the arrows is meant to indicate the weights of the scattering directions. The larger the size of the scatterer, the stronger the forward scattering of the photons.

Due to the complexities of modelling the scattering of fluorescence and Cherenkov radiation by aerosols, it is important to conduct EAS experiments at locations with low aerosol concentrations. This allows approximate aerosol models to be implemented without incurring a large uncertainty. An example of a suitable location is a high mountainous elevation, such as the Pierre Auger Observatory.

The 'clearness' of the atmosphere at the project site was tested using telescopes following bright stars, and measuring their brightness at a range of zenith angles. The vertical transmission was described in terms of the number of air masses that the light must traverse in order for the intensity to decrease to e^{-1} of it's initial value. For a perfect Rayleigh atmosphere (no aerosols), the number of air masses is 2.2 (for $\lambda = 365\,\mathrm{nm}$). The average value measured at the site was 2.06 air masses [127]. This value varies through the year with lower opacity in summer and higher in winter.

A horizontal attenuation monitor (HAM), was used to monitor the clarity of the atmosphere at $\lambda = 365\,\mathrm{nm}$. The result was a mean horizontal attenuation length of 13.3 km and a rms of 2.5 km. For an atmosphere with no aerosols, the value would be 18.7 km. For the vertical transmission value and the horizontal attenuation length the atmosphere at the site was classified as 'clear' [127].

7.2.3. Absorption

The atmosphere can attenuate a light signal through absorption of the radiation by various molecules, such as ozone O_3, water vapour H_2O, and carbon dioxide CO_2. In the UV, absorption by ozone only occurs for $\lambda < 290\,\mathrm{nm}$ [47]. This is very close to the wavelengths of interest, but just below, and it is not of concern when considering the N_2 fluorescence spectrum. Also the ozone concentration is very low in the lower atmosphere where most of the fluorescence light is generated. The other main absorbers of radiation are H_2O and CO_2, but these are only important for $\lambda > 800\,\mathrm{nm}$. Therefore it is not necessary to consider absorption in the calculation of the attenuation of fluorescence light in the EAS reconstruction algorithm.

7.3. Multiple Scattering of Fluorescence Light

When reconstructing the longitudinal profile of an EAS observed by the fluorescence detectors, the atmospheric attenuation must be taken into account. Using atmospheric models and nightly measurements of the vertical optical depth, we can determine the fraction of the light emitted around the shower axis that has been scattered out of the field of view of the detector, and then correct for this in the reconstruction process. For distant showers some of this light, through multiple scatters, can re-enter the field of view of the detector. This forms a halo of light around the shower track on the camera. This effect was studied by Roberts [128] through Monte Carlo simulations, and a parametrisation was derived for predicting the fraction of multiply scattered fluorescence light that is received within a given angular distance ζ of the shower track on the camera. Robert's expression for the fraction of multiply scattered fluorescence light is

$$\kappa = 0.774(OD \times \alpha R^{0.5}\zeta^{1.1})^{0.68}, \tag{7.7}$$

where OD is the total optical depth (for molecular and aerosol scattering) between the source and the fluorescence detector, α is the total scattering coefficient (the fraction of the beam scattered per metre of path in units m^{-1}) at the source, R is the distance (m)

from the source to the FD, and ζ is the half-angle of the angular acceptance at the FD (in degrees).

Using this parametrisation we can subtract the multiple-scattered fluorescence component from the total signal, and continue with a signal that is then directly from the source. Initially, the scattered light had been assumed lost, and as such the observed light was being interpreted as direct fluorescence light. The effect of this correction is a reduction in the reconstructed shower energies and a small reduction in the reconstructed depth of shower maximum. The shift in energy is on average $-2.7\,\%$, but this shift is energy dependent and therefore can slightly alter the shape of the energy spectrum. Figures 7.3 and 7.4 illustrate the energy dependent shifts in energy and depth of shower maximum X_{max}. The energy dependence is due to the fact that higher energy showers maximise closer to the ground where the optical depth and the scattering probability are larger, leading to a larger fraction of multiple scattered fluorescence light.

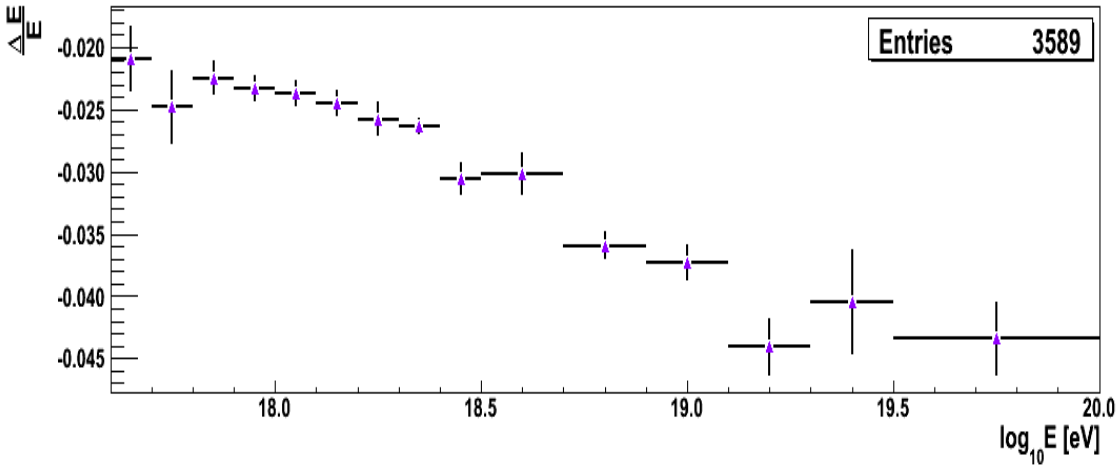

Figure 7.3.: The relative shift in energy as a function of energy, resulting from correcting for multiply scattered fluorescence light as parametrised in Eq. 7.7. The average effect is a small reduction of the shower energy, which has an energy dependence.

The magnitude of this effect as shown here, was determined by implementing the correction for multiple scattered fluorescence in the reconstruction process, using the data set presented in the 2007 ICRC Auger Collaboration elongation rate paper [129]. This data

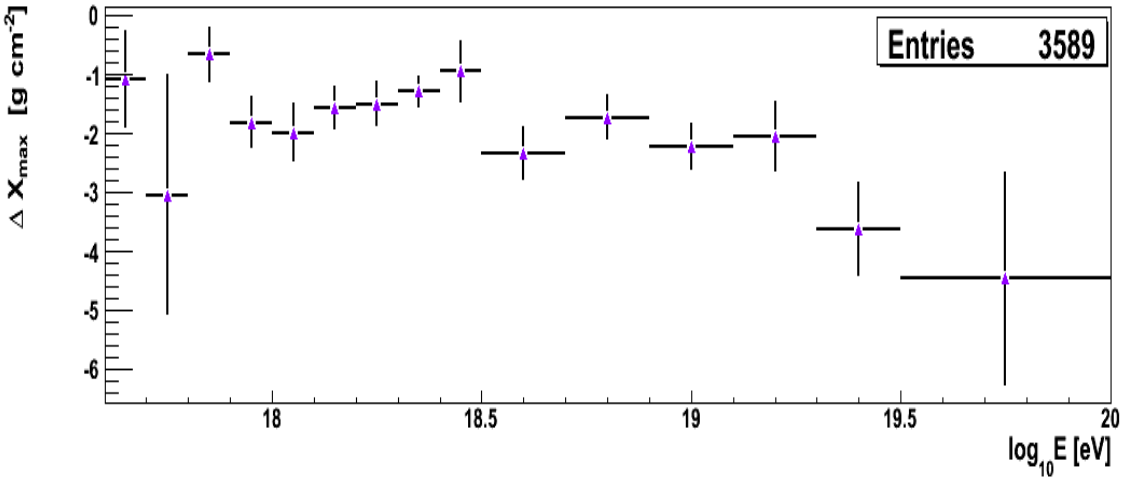

Figure 7.4.: The absolute shift in depth of shower maximum X_{max} as a function of energy, resulting from correcting for multiply scattered fluorescence light as parametrised in Eq. 7.7. The average effect is a small reduction of the depth of shower maximum.

set will be used throughout the remainder of this chapter.

7.4. Residual halo

The standard light collection algorithm used in the Auger Offline framework is the method employing the "ζ search" algorithm. This determines which pixels will contribute to the total signal in each 100 ns time bin. Using the reconstructed shower geometry, we know the position of the light spot on the camera surface for each time bin. We define a circle of radius ζ centered on the spot centre, and we include signal from a pixel for that time bin if the pixel's centre is within that circle. This is illustrated in figure 7.5. ζ is increased in increments of 0.1° out to a user defined angle. Then the value of ζ that optimises the S/N is determined and a safety margin of 0.2° is added to this value. This angle is called best zeta (ζ_{best}). An example of this is shown in figure 7.6. The integrated signal is shown in purple, and the signal to noise in green. For this shower the S/N is optimised at 1.1°, which gives a value of ζ_{best} =1.3°. However it can be seen that the integrated signal continues to increase well beyond this acceptance angle.

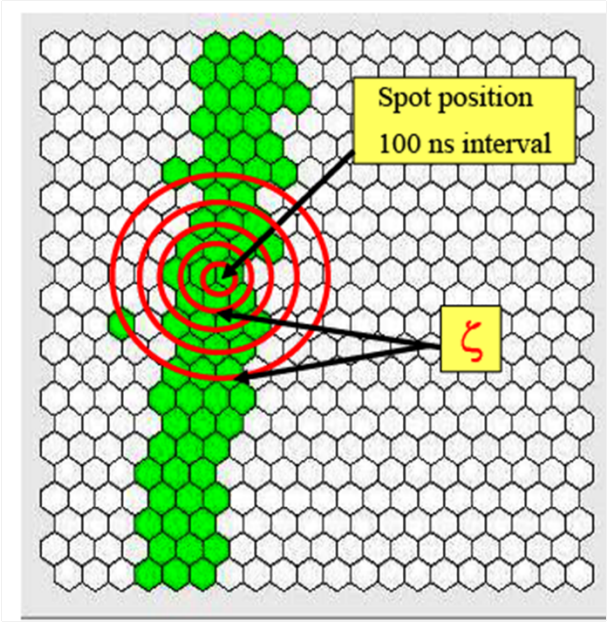

Figure 7.5.: Illustration of a shower track (in green) across a FD camera. The red circles are centred on the spot center for a given time step, and the radius of each circle is the angular acceptance angle ζ.

After the lateral width of the shower has been taken into account, as well as the halo around the shower track due to multiple scattered fluorescence light, the integrated signal

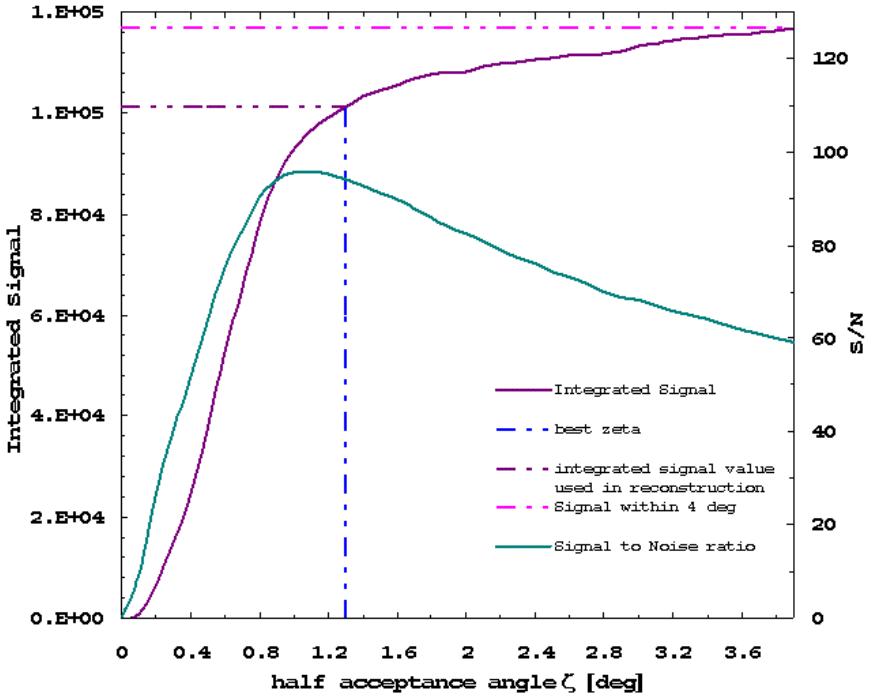

Figure 7.6.: Integrated signal and signal to noise as a function of the angular acceptance angle ζ. The dashed vertical line indicates the angle at which the signal to noise optimises plus the 0.2° safety margin. The dashed horizontal lines indicate the integrated signal at ζ_{best} and at 4.0°.

as a function of angular distance from the shower track continues to increase well beyond ζ_{best}. This is illustrated in figure 7.7. While it could be argued that if we still believe that there is signal past this angular distance then we should just integrate out further, this would include much more noise, and the uncertainty in the determination of shower energy and depth of shower maximum would increase. This defeats one of the science goals of Auger, which is to determine the energy and composition of cosmic rays to a high precision. The better alternative is to determine the nature of this light forming a halo around the shower track, and then decide how important it is for us to take this light into account.

From the initial investigation of this halo I observed that the halo appeared to be larger for inclined showers compared to vertical showers. This phenomena had not been observed in tests with nitrogen lasers [130]. The halo also appeared to be wider for close-by showers,

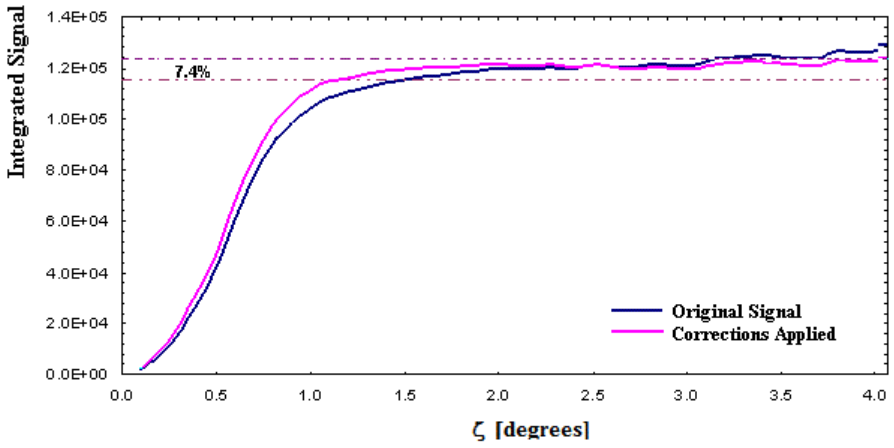

Figure 7.7.: This plot shows the integrated signal as a function of ζ. The integrated signal before the lateral width and multiple scattering of fluorescence corrections are applied, is shown in blue, and after the corrections have been applied is shown in pink. The dashed lines show that past ζ_{best}= 1.0°, there is still a 7.4% increase in the integrated signal once the corrections have been applied.

which is opposite to the behaviour of the multiple scattered fluorescence correction, but similar to the behaviour of the lateral width correction. This led me to believe that the halo may be associated with the intrinsic width of the showers.

7.5. Fractional Increase

The halo will be referred to as the 'fractional increase' from here onwards. I have defined it as the relative increase in the integrated signal from some angular distance from the track ζ, compared to the integrated signal out to 4.0°. It will be labelled as $f_{\zeta-4.0^\circ}$, and is given by,

$$f_{\zeta-4.0^\circ} = \frac{S_{4.0^\circ} - S_\zeta}{S_\zeta} \tag{7.8}$$

where S_ζ is the integrated signal out to ζ, and $S_{4.0^\circ}$ is the integrated signal out to 4.0°. The reason for this 4.0° limit is that past this angular distance the signal from pixels is no longer readout and recorded. The uncertainty on this value is calculated using the integrated noise out to these values. We collect the signal S and the squared noise N^2,

integrated out to ζ and 4.0°. The squared noise includes contributions from night sky noise and Poisson fluctuations of the signal. It is important to note that the signals out to ζ and 4.0° are correlated when calculating the uncertainty in the fractional increase. The contribution to the noise squared between ζ and 4.0° is then $N^2_{4.0^\circ} - N^2_\zeta$.

The uncertainty on the fractional increase is given by:

$$\Delta f_{\zeta-4.0^\circ} = f_{\zeta-4.0^\circ} \sqrt{\left(\frac{N^2_{4.0^\circ} + N^2_\zeta}{(S_{4.0^\circ} - S_\zeta)^2} + \frac{N^2_\zeta}{S^2_\zeta} \right)} \tag{7.9}$$

7.6. Search for Correlation

7.6.1. Selection Criteria

To study the nature of the halo of light around the main shower track, I chose to use a set of bright hybrid showers, that met the following selection criteria:

- FD timing fit has a reduced χ^2 <5.
- Gaisser-Hillas fit to the shower detector profile has a reduced χ^2 <5.
- Reconstructed X_{max} is within the viewed track, and that the shower has been observed for at least 100 $\mathrm{g\,cm^{-2}}$ above and below X_{max}.
- View the shower for at least 400 $\mathrm{g\,cm^{-2}}$.
- Zenith angle of shower > 40°.
- Minimum Viewing Angle > 25°.
- Only events seen by Los Leones (eye1) or Coihueco (eye4).
- Time residual between the SD time and the fit is less than 200 ns.
- Distance between the reconstructed shower axis and the tank used in the fit is less than 2000 m.

7.6.2. Initial Search for Correlations

As showers can be quite noisy, looking at the fractional increase in each time bin would be difficult. Instead, for the initial work in trying to find correlations, I divided up the field of view of the detector into roughly 8° elevation ranges and calculated the fractional increase across the track segment. I then calculated the maximum distance to each 8° track segment and the maximum shower age observed within this segment. The reason for using the maximum shower age and distance is that for a given shower geometry the distance to the track influences the minimum shower age and hence the average shower age within the field of view. This is illustrated in figure 7.8. The average distance to the track is also affected by the field of view for close-by showers, so the maximum distance is used here. These two parameters are often correlated. As low energy showers maximise higher in the atmosphere we observe them at large shower ages. They must also land close to the detectors for the showers to be bright enough to reconstruct successfully. On the other hand high energy showers can be observed at much larger distances, but we are less likely to observe large ages for these showers as on average they maximise closer to the ground.

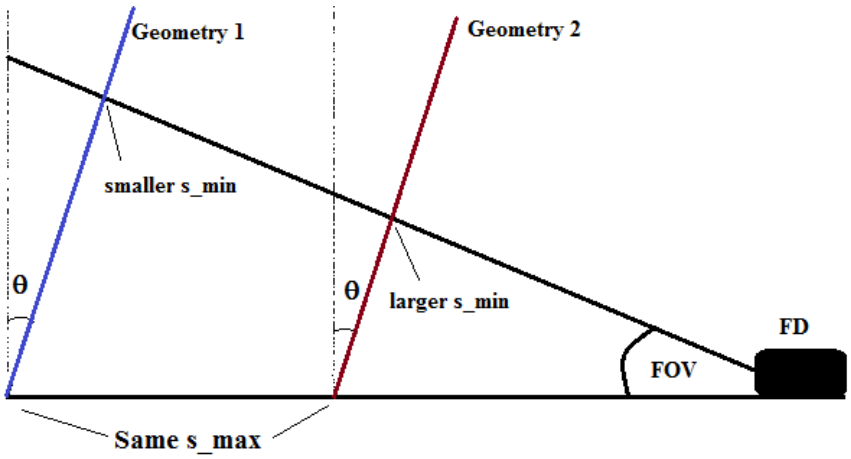

Figure 7.8.: Illustration showing the bias that the field of view imposes on the average shower ages viewed by the Fluorescence Detectors. For the two shower axes shown here, the closer shower would have a larger average shower age in the field of view than the more distant shower.

Initially I decided to check whether the halo was constant over the entire shower track. To

do this I broke the camera up into 4 elevation ranges; less than 8°, 8° to 16°, 16° to 23°, and 23° to 30°. Using 90 bright events whose tracks spanned all four elevation ranges, I calculated the value of ζ_{best} for each track segment individually, and then compared the signal within ζ_{best}, which is the signal value that would have been used in the reconstruction, to the integrated signal out to 4.0°. Figure 7.9 shows the fractional increase calculated for these 90 showers for each of the four track segments. On average $f_{\zeta_{best}-4.0^\circ}$ is largest for the lowest 8° of the shower track, and it decreases as the pixel elevation increases.

In practice, the entire shower track is used to find the value of ζ that maximises the signal-to-noise ratio, to which the safety margin of 0.2° is added. But as can be seen figure 7.10, the average value of ζ_{best} is almost 0.2° larger in the bottom 8° of the camera than in the top 8°. This means that if I had conducted the same test as described above, but with ζ_{best} calculated by averaging over the whole track, then the fractional increase would be even larger towards the bottom of the shower track and even smaller towards the top.

As $f_{\zeta-4.0^\circ}$ was at its largest for each shower track within the lower 8° of the camera I then chose to focus on this segment to search for correlations with various shower parameters. The first correlation found was with the zenith angle of the showers. I found that the fractional increase between ζ_{best} and 4° increased with the zenith angle of the shower. A possible reason for this is that inclined showers traverse a larger atmospheric mass than vertical showers of the same energy and composition. This leads to the fluorescence detectors viewing the shower at larger shower ages. Figure 7.11 shows this correlation between $f_{\zeta-4.0^\circ}$ and zenith angle, as well as the correlation between the maximum shower age, $s_{max}(X)$, viewed by the lowest 8° of the camera with the shower's zenith angle.

Figure 7.12 shows the correlation between $f_{\zeta-4.0^\circ}$ and $s_{max}(X)$ directly. A steady increase in the fractional increase out to 4.0° can be seen as the maximum shower age in the field of view increases.

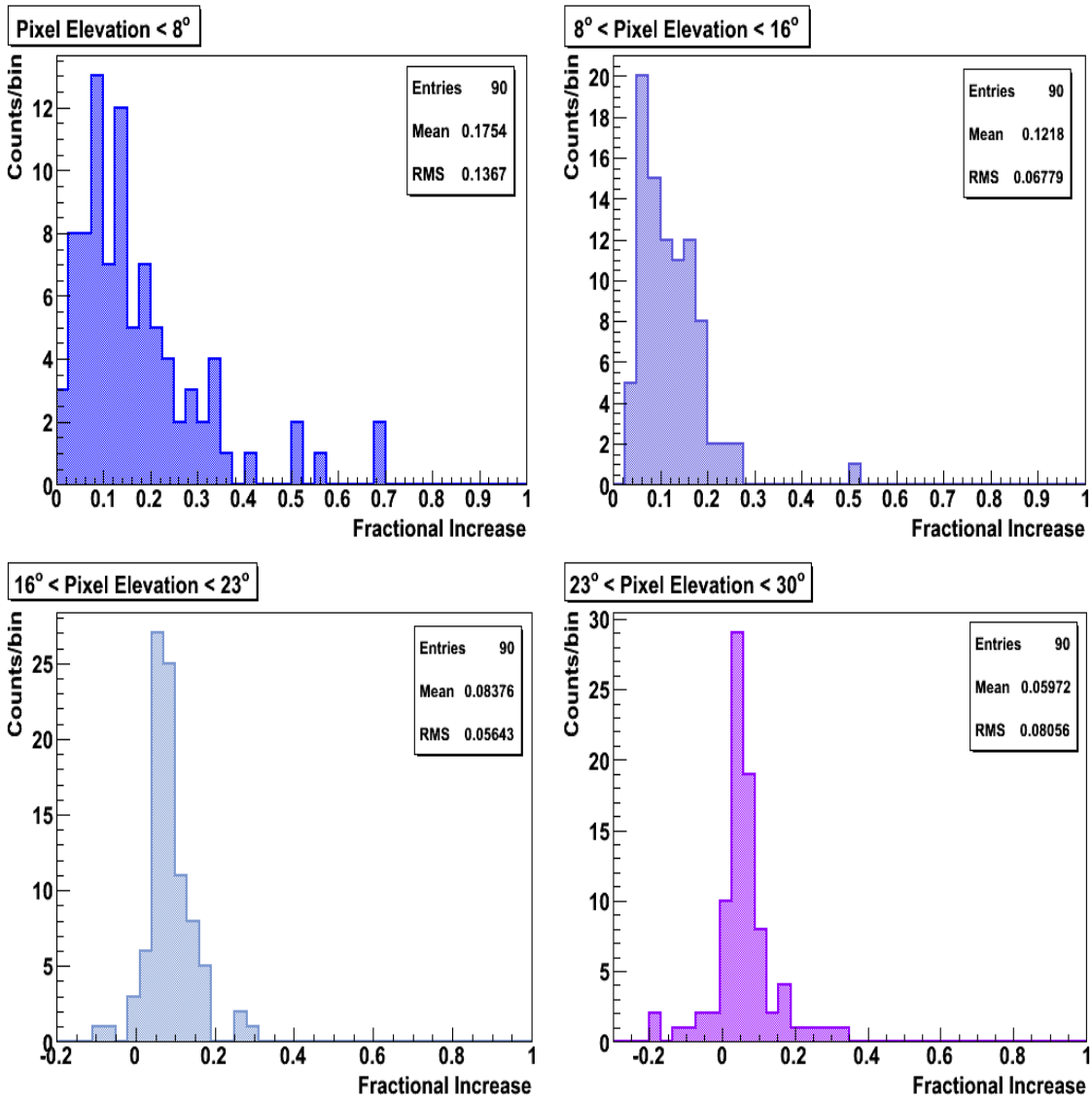

Figure 7.9.: Histograms showing the fractional increase calculated for 90 bright showers in four regions across the camera. The mean fractional increase is largest in pixels within the lowest 8 degrees of the shower, and decreases moving up the camera.

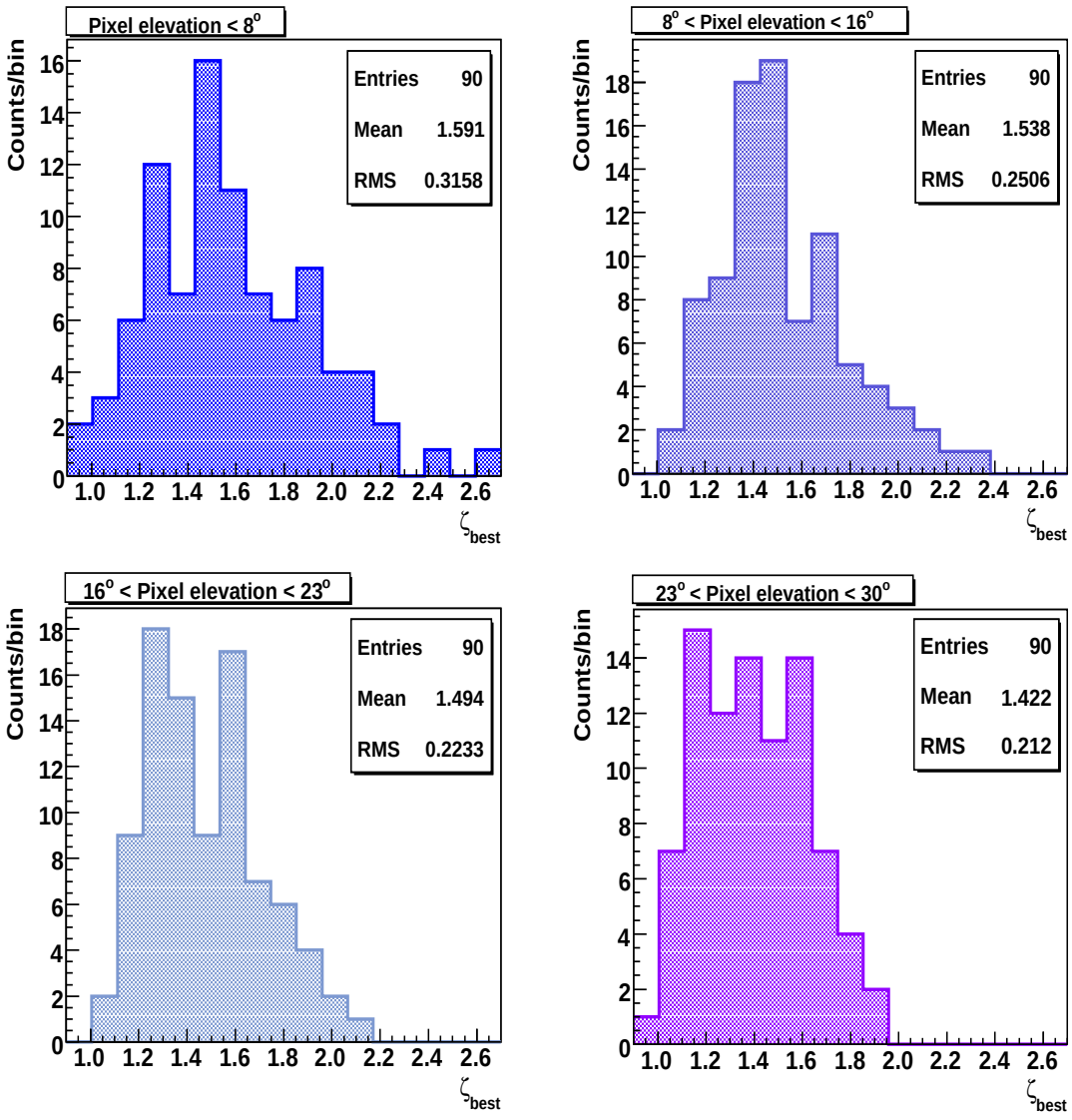

Figure 7.10.: Histograms showing the values of angular distance (in degrees) from the shower track that optimises the signal to noise, calculated for 90 bright showers in four regions across the camera. On average, ζ is largest for the lowest track segment, and decreases as the track segments get higher on the camera.

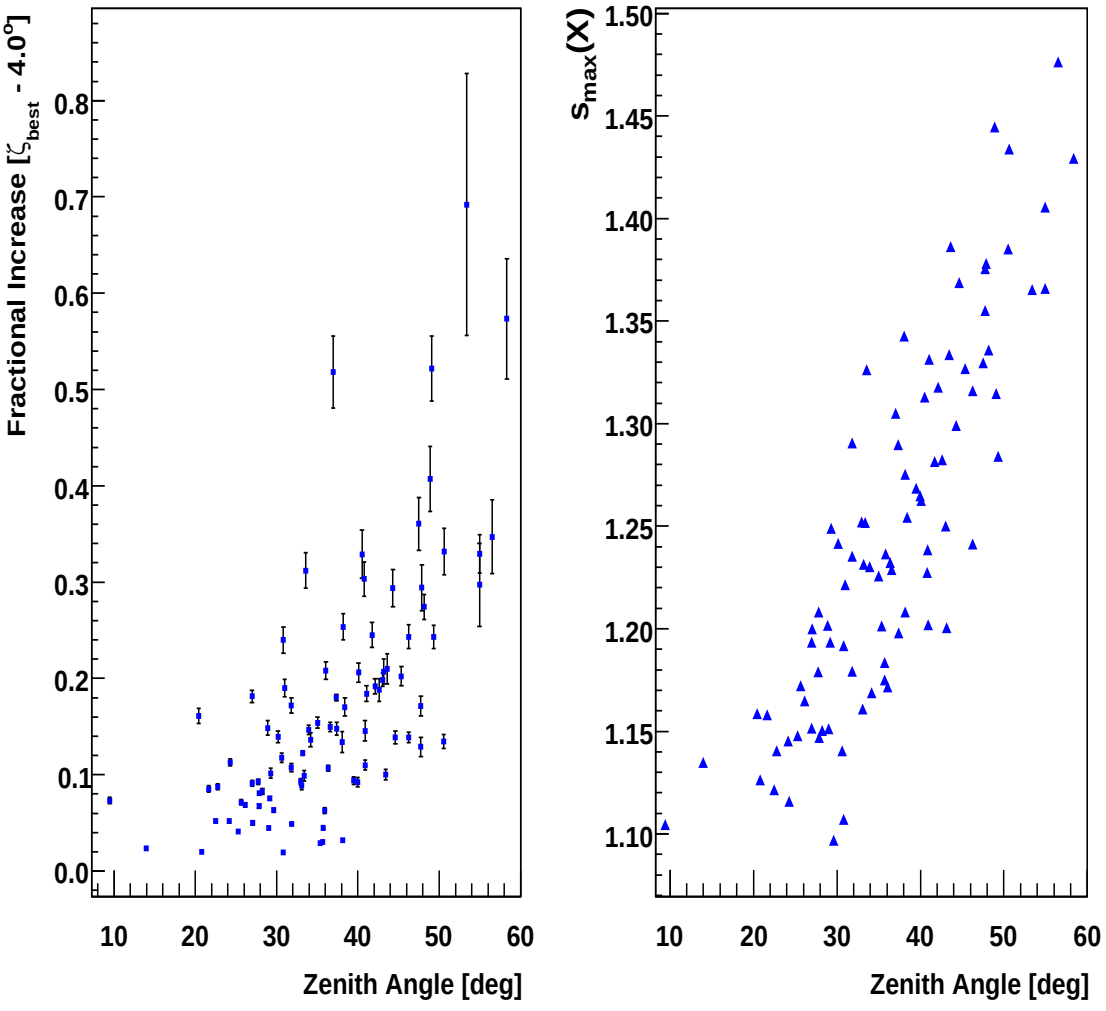

Figure 7.11.: The plot on the left shows the fractional increase between ζ_{best} and 4.0° vs. the zenith angle of the shower for the lowest 8° of elevation. The error bars in the right plot were calculated using equation 7.9. On the right is the maximum age $s_{max}(X)$ viewed by the lowest 8° of the camera vs. the zenith angle of the shower.

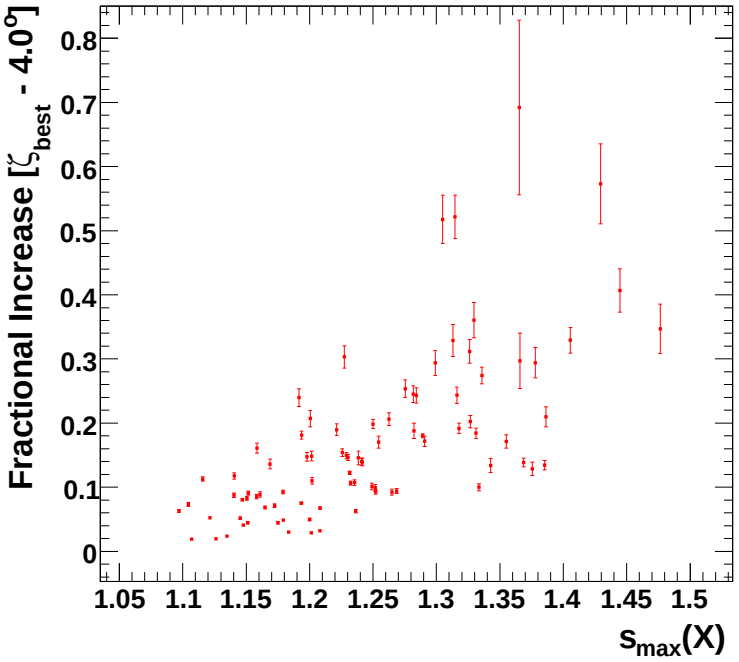

Figure 7.12.: This is the same data from figure 7.11, but with the fractional increase plotted against maximum age viewed by the camera within the lowest 8° of elevation.

7.6.3. Method required for further study

Using pieces of the shower tracks spanning 8° in elevation proved to be too large for this study. In the case of inclined showers, a large amount of shower development can occur over such a large angular distance. Instead I chose to divide up the shower tracks into 1.5° elevation angle increments, to study the behaviour of the fractional increase with shower evolution and with shower geometry in more detail. Once again, the value of ζ_{best} was calculated for each 1.5° segment of the track, and the integrated signal and the integral noise were calculated out to ζ_{best}, and out to 4.0°.

7.7. Shower age correlation

In section 7.6.2, a loose correlation between the fractional increase of the integrated signal and the shower age was found using a handful of bright events. A hypothesis for the correlation with shower age is that it is due to the fact that scattered Cherenkov light dominates the light at the bottom of the shower track where the atmosphere is thickest, especially for showers of large age, where the Cherenkov beam is strongest. Here the corrections relating to the lateral width of the direct fluorescence light at the detector, and for the multiple scattered fluorescence light have already been applied, leaving a residual which we believe is partly due to scattered Cherenkov light.

7.7.1. Creating correlation coefficients dependent on angular acceptance

Initially the fractional increase was calculated for a specific value of ζ out to 4.0°. However, what is required is a correlation that will take the shower age, and any value of ζ and calculate the expected fractional increase. Figures 7.13 and 7.14 show the correlation between $f_{\zeta-4.0^\circ}$ and shower age, for 2,081 1.5° track segments from across the entire elevation range, for values of ζ ranging from 1.0° to 2.5°. The best fit to the data was found to be an exponential function of the form $e^{A.s(X)+B}$. Such exponential functions were fitted to the fractional increase as a function of shower age for each value of ζ between $[1.0^\circ, 2.5^\circ]$.

This is displayed in figures 7.13 and 7.14. Then plotting the constant B and the slope A of these exponential fits as a function of ζ , the fractional increase out to 4.0° can be calculated.

$$f_{\zeta-4.0^\circ} = e^{A(\zeta)s(X)+B(\zeta)} \tag{7.10}$$

By using $e^{a+b} = e^a e^b$, eq.7.10 can be simplified to $e^{B(\zeta)}e^{A(\zeta)s(X)} = C(\zeta)e^{A(\zeta)s(X)}$. The parameter A as a function of ζ was found to be

$$A(\zeta) = 1.915\zeta + 1.613 \tag{7.11}$$

Substituting this into eq.7.10 and using the simplification decsribed above, the parameterisation for the fractional increase is now

$$f_{\zeta-4.0^\circ} = C(\zeta)e^{s(x)(1.915\zeta+1.613)}. \tag{7.12}$$

What this shows is that the fractional increase is a function of shower age, and that for any value of ζ we can parameterise the light outside of ζ out to 4.0°. This could then be used to correct for this halo of light if we determined $C(\zeta)$. To determine the source of this halo, correlations with other shower parameters are required. Therefore $C(\zeta)$ will remain undefined for now.

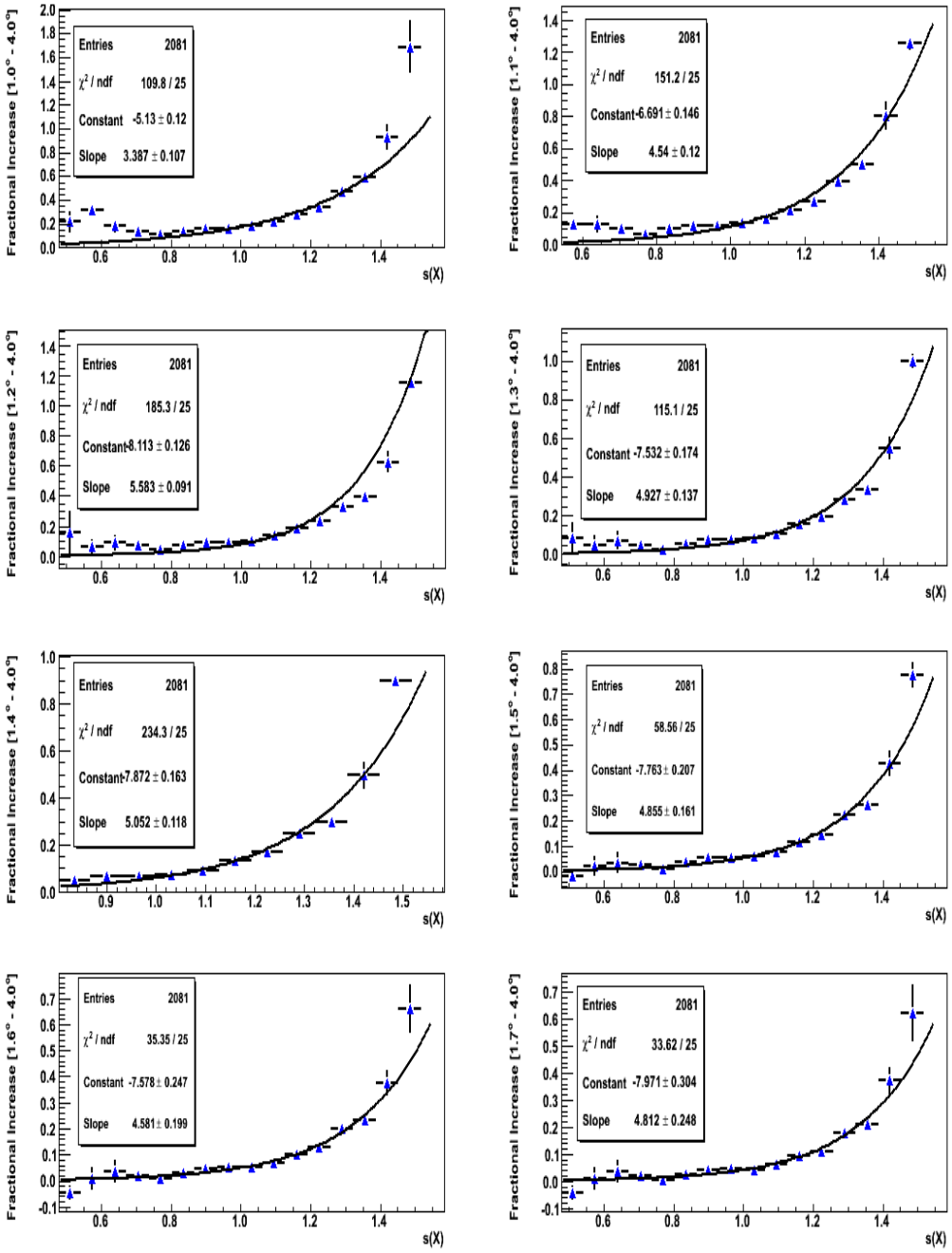

Figure 7.13.: Exponential fits to the fractional increase between ζ and 4.0°as a function of shower age, for eight different values of ζ ranging from 1.0 to 1.7. Corrections for fluorescence lateral width and multiple scattering have already been applied.

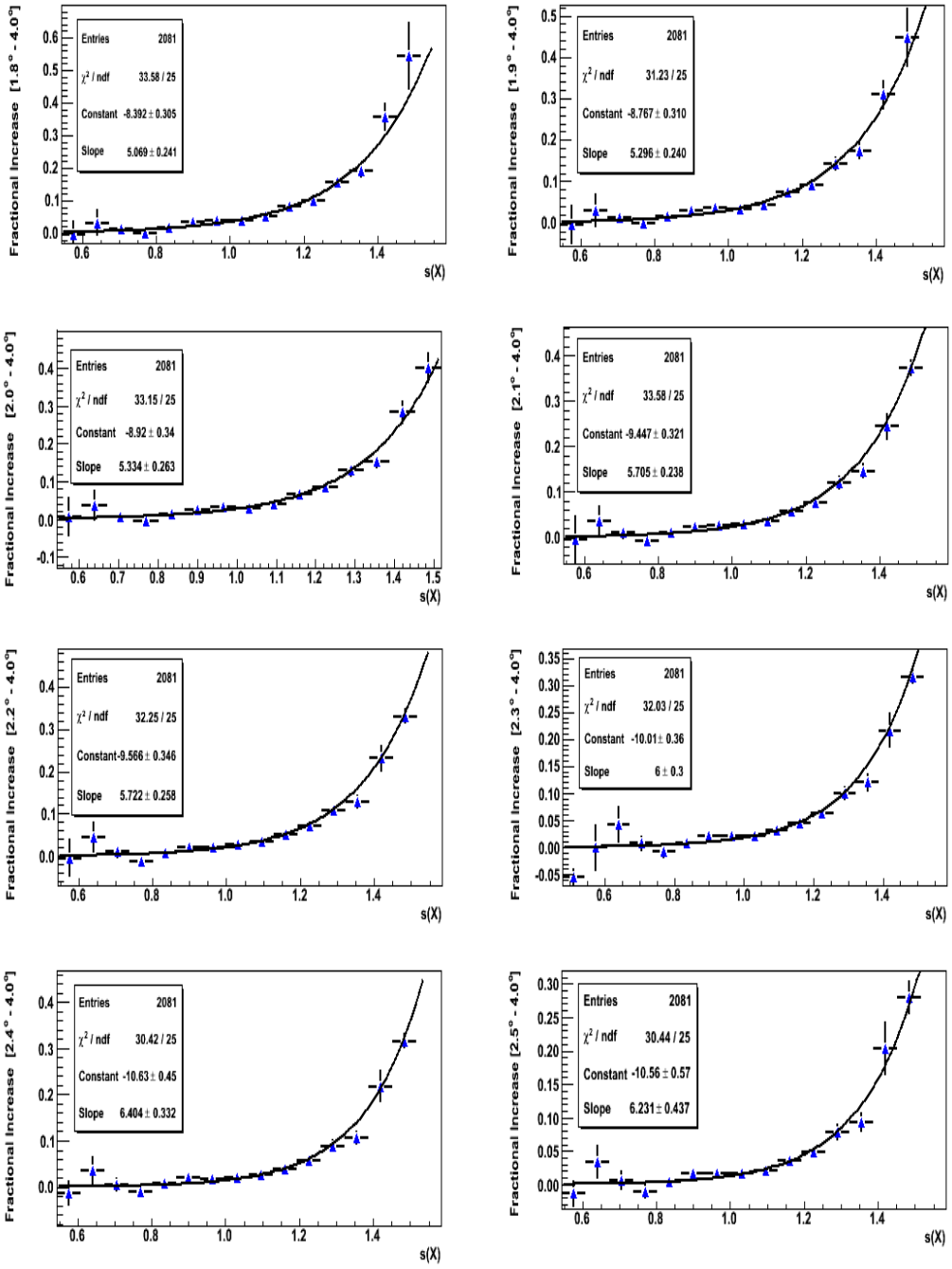

Figure 7.14.: Exponential fits to the fractional increase between ζ and 4.0°as a function of shower age, for eight different values of ζ ranging from 1.8 to 2.5.

7.8. Scattering probability correlation

If the halo that we are observing is due to singly scattered Cherenkov light, then we should observe a correlation between the scattering probability at the track and the magnitude of the halo. The correlation should also depend on the distance to the shower track and the Rayleigh phase function (see Eq. 7.5 in sub-section 7.2.1). The Rayleigh phase function is used in preference to the aerosol phase function as the aerosol phase function is strongly forward peaked. This means that the Cherenkov light is scattered by aerosols along the shower axis, and this component of scattered light would be small compared to the direct Cherenkov light, which would only be a problem if the shower axis is directed towards the FDs. Showers with large Cherenkov fractions are not properly reconstructed, and hence any shower that we view at less than 20° to the shower axis is not used. The Rayleigh scattering probability α (the fraction of the beam scattered per metre of path in units m^{-1}), is a function of wavelength, but to make this easier I have chosen to use the value of α for the dominant Cherenkov wavelength. From Cherenkov theory, the Cherenkov yield is proportional to λ^{-2}. The Cherenkov yield is shown as a function of λ in figure 7.15, as well as the detector efficiency as a function of wavelength in figure 7.16, and the product of these two in figure 7.17. From figure 7.17 it can be seen that the product of the detector efficiency and the Cherenkov Yield is roughly flat for $320\,\mathrm{nm} < \lambda < 380\,\mathrm{nm}$, so $\lambda = 354\,\mathrm{nm}$ was chosen.

In trying to find these correlations, we must concede the fact that the scattering probability will be correlated with shower age, as large shower ages occur deep in the atmosphere where the atmospheric density is the largest.

In figure 7.18, the fractional increase is plotted as a function of scattering probability α, the Rayleigh scattering phase function (where ξ is the angle between the detector and the shower axis), and the distance from the FD to the shower track, d, all multiplied by Eq. 7.12, for each 1.5° element. This is shown for four values of ζ. The result is a linear correlation for each value of ζ.

What we can see is that for large shower ages, large scattering probabilities, small distances and small scattering angles, the fractional increase is at its largest.

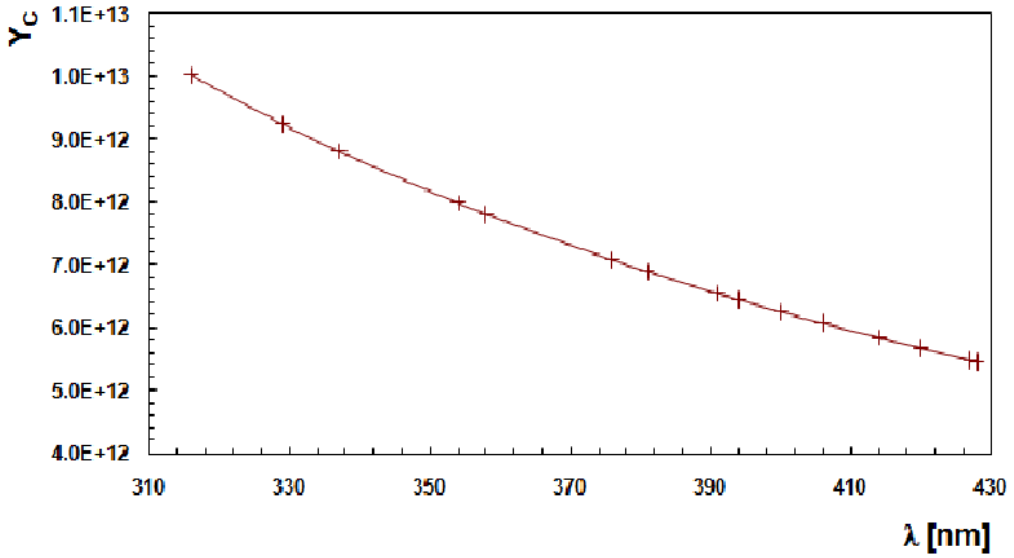

Figure 7.15.: The Cherenkov yield as a function of wavelength for the fluorescence detectors' range of sensitivity.

The d^{-1}correlation, rather than the instinctive d^{-2}, is due to the fact that the fractional increase has been calculated for fixed angular track segments. As this is also the way it will be done in the reconstruction algorithm this is not an issue.

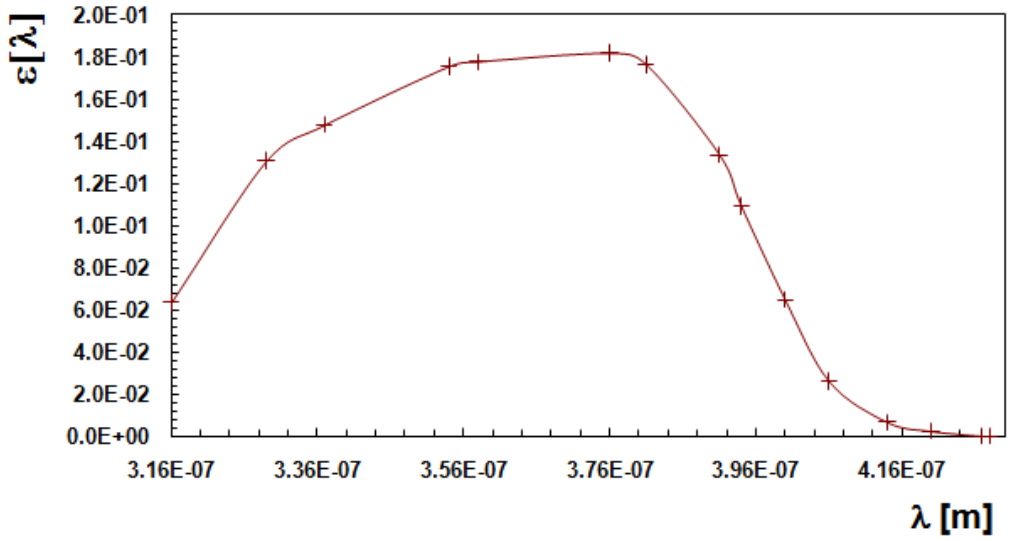

Figure 7.16.: The fluorescence detector efficiency as a function of wavelength. This is a combination of mirror reflectivity, optical filter transmission and PMT quantum efficiency.

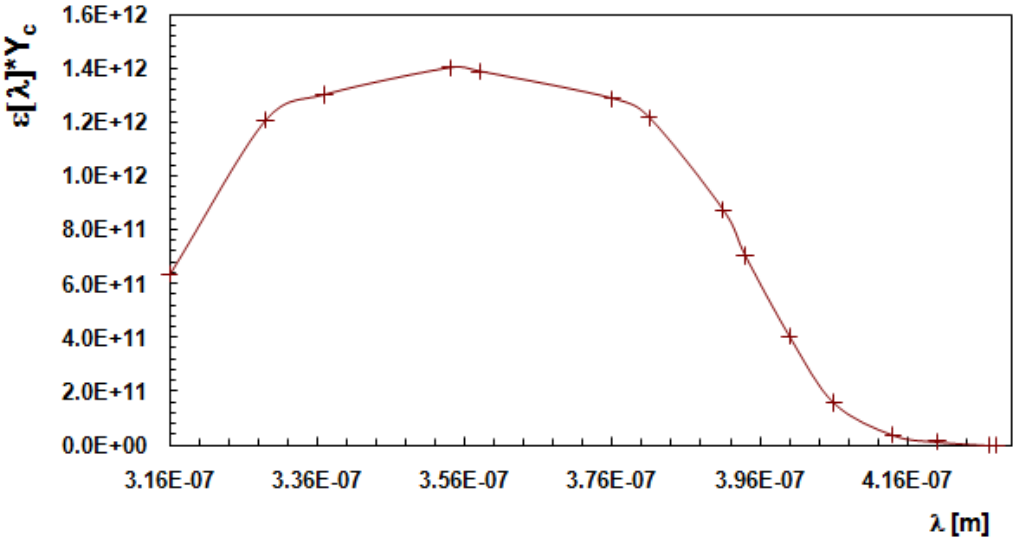

Figure 7.17.: The fluorescence detector efficiency multiplied by the Cherenkov spectrum displayed in figure 7.15, as a function of wavelength. This is roughly flat between 330 nm and 380 nm.

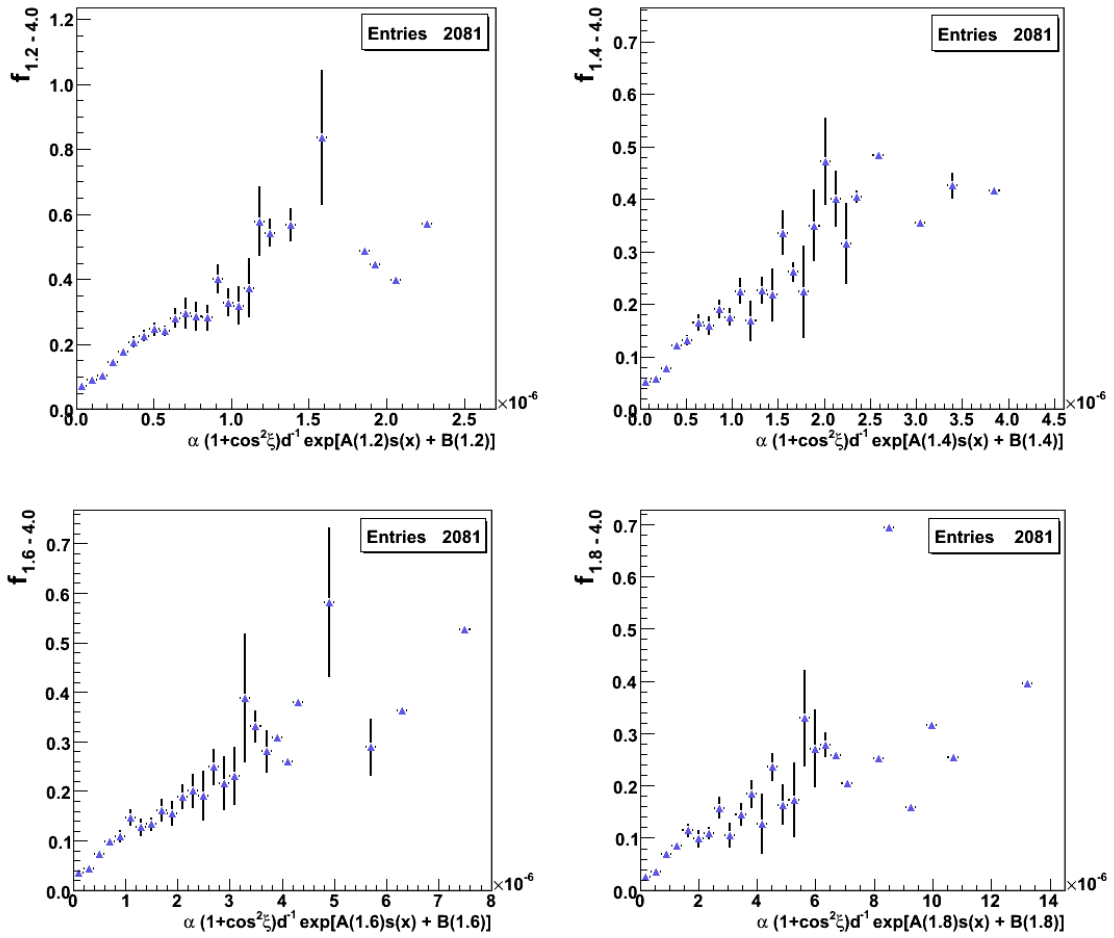

Figure 7.18.: The fractional increase between ζ and 4.0° plotted against the product of $\frac{\alpha\left(1+\cos^2\xi\right)}{d}e^{s(x)(1.915\zeta+1.613)}$, for ζ equal to 1.2°,1.4°,1.6° and 1.8°. A(s) and B(s) are the fits to the fractional increase as a function of age from section 7.7.1.

7.9. Final Parametrisation

As shown in sections 7.7 and 7.8, correlations with the fractional increase are observed for distance to the shower, shower age, scattering probability and scattering angle between the shower and the camera. These are indicative of the halo arising from scattered Cherenkov light. The Cherenkov light produced by EAS increases in intensity along the shower track, which is the reason for the age correlation. In section 7.7, the correlation with shower age was found as a function of ζ out to 4.0°, and in section 7.8 the same method was invoked to find correlations between the fractional increases out to 4.0° with the scattering probability of Cherenkov light, the Rayleigh scattering angular distribution and the distance to the shower. By using the age correlation as a function of ζ, and multiplying it by $\alpha\ (1+\cos^2\varphi)\ d^{-1}$, a linear fit can be found for each value of ζ.

$$f_{\zeta-4.0^\circ} = D(\zeta) + E(\zeta)\frac{\alpha\ (1+\cos^2\varphi)}{d}e^{s(x)(1.915\zeta+1.613)} \tag{7.13}$$

Then the linear fit parameters $D(\zeta)$ and $E(\zeta)$ can be plotted as functions of ζ, as shown in figures 7.19 and 7.20. The best fits to the data are;

$$D\left(\zeta\right) = 0.10\,\zeta^{-2.57} \tag{7.14}$$

and

$$E\left(\zeta\right) = 1.92\times10^{7}e^{-3.49\,\zeta}. \tag{7.15}$$

These can then be inserted into Eq. 7.13, to give a complete parametrisation (Eq. 7.16)

$$f_{\zeta-4.0^\circ} = 0.10\,\zeta^{-2.57} + 1.92\times10^{7}e^{-3.49\,\zeta}\frac{\alpha\ (1+\cos^2\varphi)}{d}e^{s(x)(1.915\zeta+1.613)} \tag{7.16}$$

The first component in equation 7.16 is independent of shower evolution, shower geometry and the scattering probability. This means that there is one component that does not

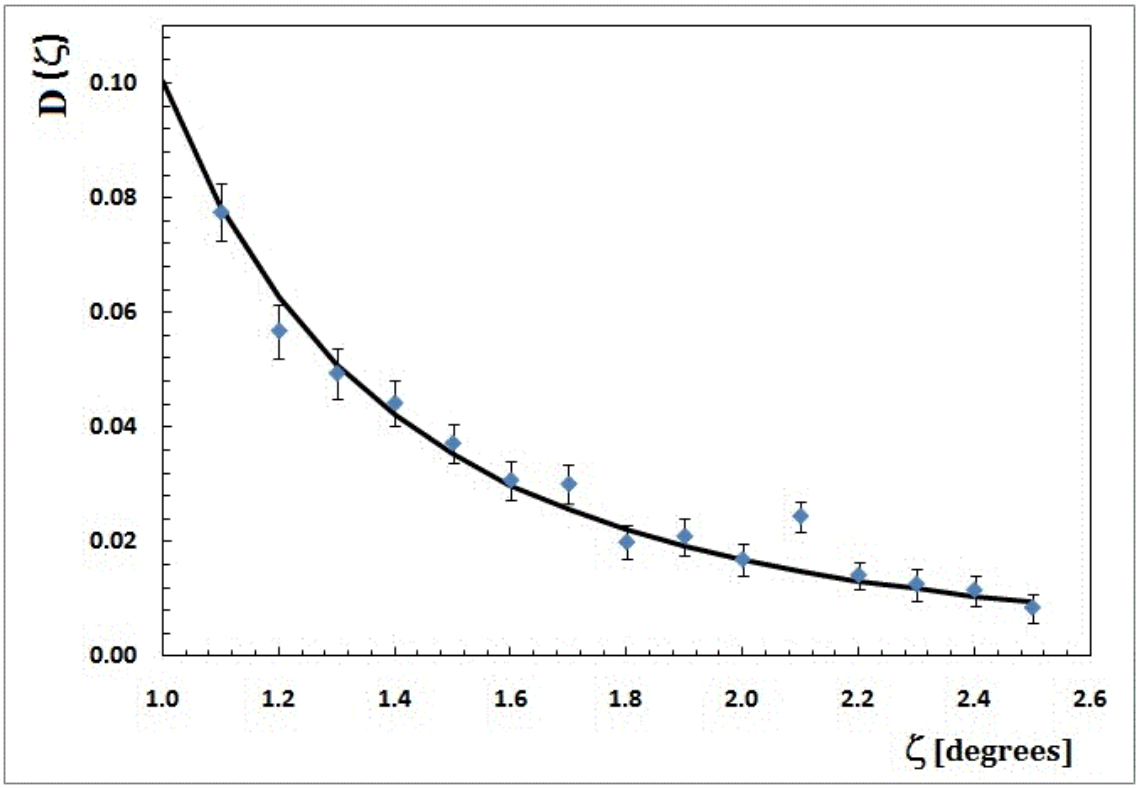

Figure 7.19.: The value of the parameter D from the equation 7.13, for $\zeta \in [1.1, 2.5]$. The error bars are from the uncertainty in the linear fit. The black solid line is a power law, described by Eq. 7.14.

appear to originate from the Cherenkov light, and therefore should not be included when implementing the correction into the reconstruction process. For a typical $\zeta = 1.5°$, the contribution from the first term in equation 7.16 is 0.035 or 3.5%, which must come from another source.

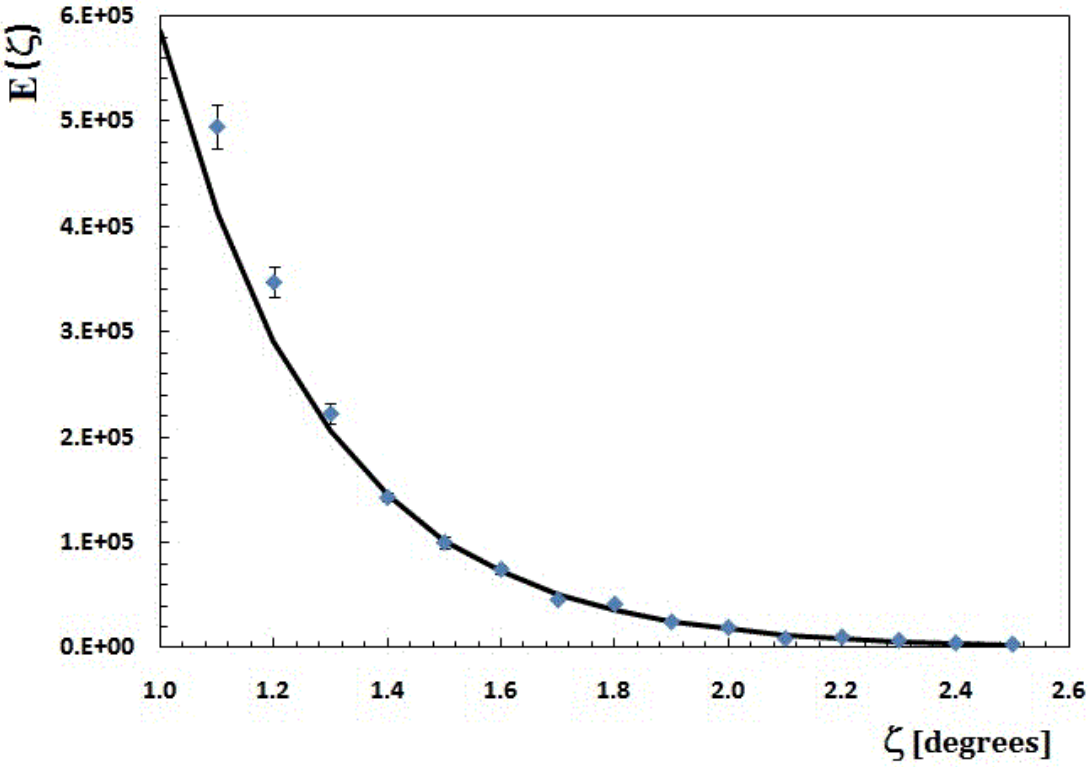

Figure 7.20.: The value of the parameter E from the equation 7.13, for $\zeta \in [1.1, 2.5]$. The error bars are from the uncertainty in the linear fit.

7.10. Implementation into Offline

In the Auger $\overline{Offline}$ module FdCherenkovSubtractor.cc, the expected fractional increase was calculated and then this light was subtracted away from the scattered Cherenkov component. This ensures that the singly scattered Cherenkov light that falls outside ζ_{best} is not subtracted away from the total light signal inside ζ_{best}.

7.11. Results

The shifts in energy and depth of shower maximum due to the correction for scattered Cherenkov light derived above, are shown in figure 7.21. Once again the 2007 ICRC Auger Collaboration elongation rate paper dataset was used. On average, there is a 4 % increase in reconstructed energy and an $8\,\mathrm{g\,cm^{-2}}$ increase in depth of shower maximum. The shifts become more interesting as a function of energy. Figure 7.22 shows that these shifts are energy dependent, with low energy showers being affected by the correction more than higher energy showers. This is because for low energy showers we observe larger shower ages on average, for which the magnitude of the correction is larger. As the shifts are energy dependent this results in a slight change in the slope of the energy spectrum and will affect the elongation rate below $10^{18.5}$ eV. This is opposite to the effect that the multiple scattering of fluorescence light had on the reconstructed shower parameters, where high energy showers were those most affected, with their energies and depth of shower maxima being reduced.

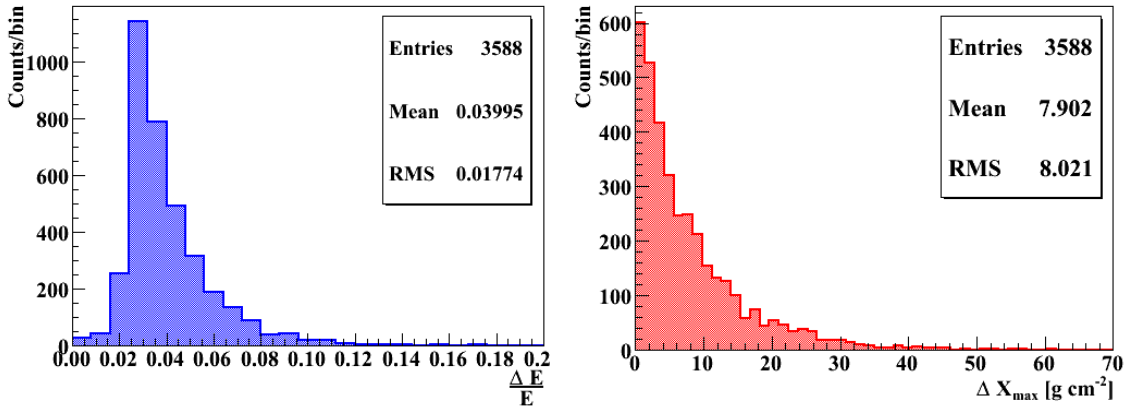

Figure 7.21.: Left: Histogram of the fractional shifts in energy due to the correction for the Cherenkov halo. Right: Histogram of the absolute shifts in depth of shower maximum.

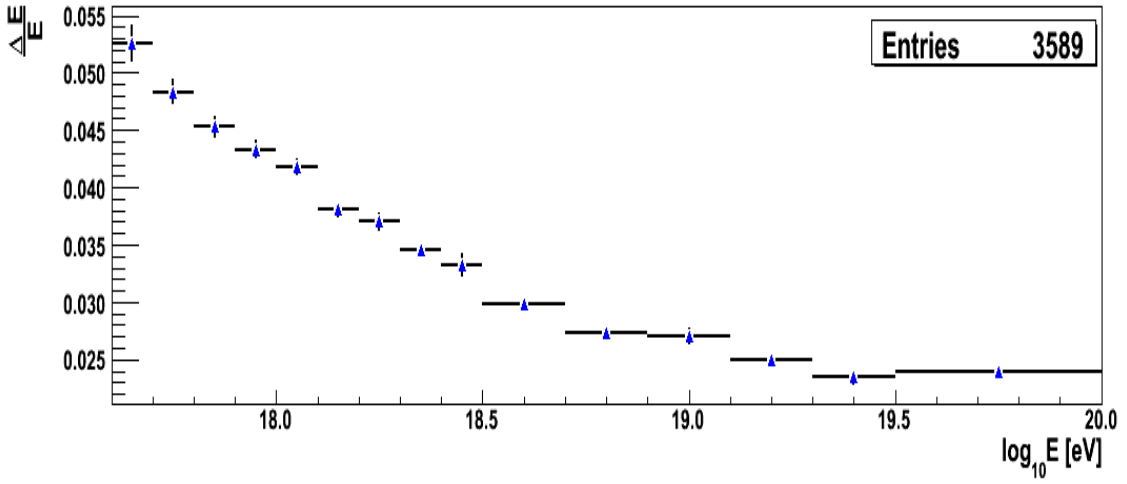

Figure 7.22.: Relative shift in reconstructed shower energy as a function of energy, from applying this correction for the scattered Cherenkov light.

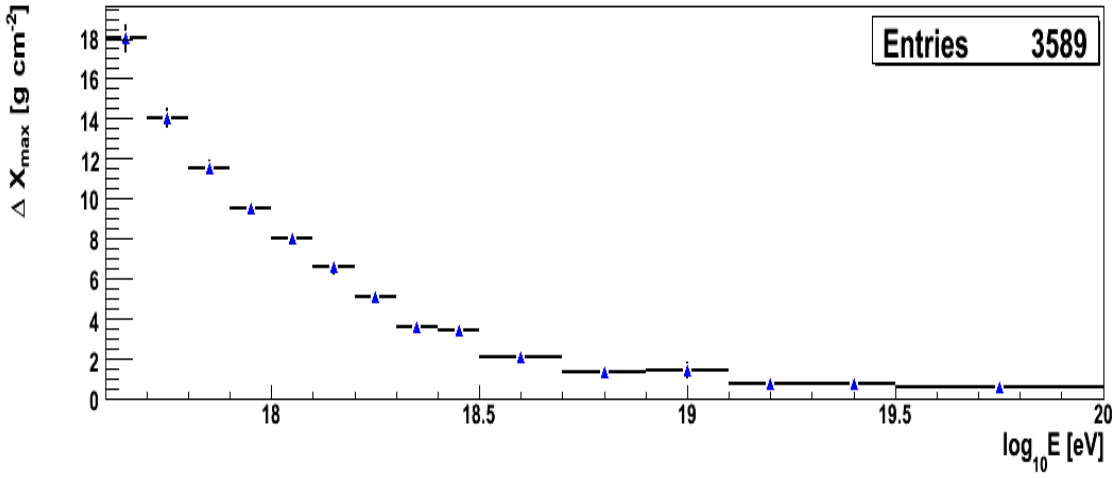

Figure 7.23.: Shift in the reconstructed depth of shower maximum as a function of energy.

7.12. Stability of Correction

Due to the component in the parametrisation that was not included in the implementation in the $\overline{Offline}$, there is still a non-zero fractional increase between ζ_{best} and 4.0°. The magnitude and shape of this halo, as well as possible sources have been investigated in [131, 132, 133, 134, 135]. These investigations are continuing.

7.13. Conclusion

The overall effect of the correction for scattered Cherenkov light on the reconstructed shower energies is 4 %. The change in energy is energy dependent and it may make a small change to the calibration of the surface detector energies, but this shift is within the current systematic uncertainties. An important outcome of this work has been to determine the shift in the calculated depth of shower maximum as a function of energy. This reduced the elongation rate below $10^{18.5}$ eV. A complementary approach has since been conducted by Michael Unger for the Auger Collaboration [136]. He implemented a Cherenkov lateral distribution into the $\overline{Offline}$ using the results of Giller and Wieczorek [137], and finds shifts in energy and X_{max} consistent with this work, with an energy shift of 5 %. This means that the parametrisation presented here is an important check for any theoretical models using the Cherenkov lateral distribution.

8. Lateral Distribution Function

This final chapter confronts the disagreement that exists between the different light collection methods in the calculation of the shape and magnitude of the halo of light that exists around the shower tracks on the FD camera. The standard light collection method was introduced in Chapter 7. Here I will introduce an alternative light collection method called the "spot reconstruction method" developed by Giulio et al. [144], and present the results of my comparison of the two methods' calculations of the halo. Lastly I will state my recommendations for light collection at the FD camera.

8.1. Spot Reconstruction Method

The spot reconstruction method is based on a model for the light distribution at the FD's telescopes' focal surfaces. Spherical aberration of the telescope optics produces a spot shape. This depends on the position of the spot on the camera. So, for a known spot shape, the fraction of the signal expected in a pixel close to the spot centre can be calculated, which can be compared to the signal measured in the pixels. The expected photon flux is estimated assuming a shower development described by a Gaisser-Hillas function, and fitted to the data using the least squares method. The expected total flux in 370 nm equivalent photons, $\widehat{n}^{370}_{\gamma tot}(t; N_{max}, X_{max}, X_1)$, consists of both fluorescence and Cherenkov photons:

$$\widehat{n}^{370}_{\gamma tot}(\mathrm{t};N_{max},X_{max},X_1) = \widehat{n}^{370}_{\gamma fluor}(t;N_{max},X_{max},X_1) + \widehat{n}^{370}_{\gamma cher}(t;N_{max},X_{max},X_1) \quad (8.1)$$

where t is time, N_{max} is the number of particles at shower maximum, X_{max} is the depth of shower maximum and , X_1 is the shape parameter of the Gaisser Hillas function. $\widehat{n}^{370}_{\gamma fluor}(t;N_{max},X_{max},X_1)$ is the expected fluorescence flux in 370 nm equivalent photons and $\widehat{n}^{370}_{\gamma cher}(t;N_{max},X_{max},X_1)$ is the expected Cherenkov flux in 370nm photons.

With the spot model and pixel calibration constants, the expected number of ADC counts can be calculated from the photon flux (Eq. 8.1). We can then calculate the χ^2 which, when minimised, gives the best estimates of the Gaisser-Hillas parameters. In the spot model the Cherenkov component is a function of the fit parameters, which is different to the standard method where Cherenkov light is treated as background to the fluorescence.

8.2. Spot Model

Even in the case of a point source of light, spherical aberration results in a spread of photons at the focal surface. So the photons arriving from the shower at a given time form an image on the focal surface with a typical width of 0.5°. The spot width is also dependent on the lateral distribution of shower particles around the shower track. This lateral distribution is in-turn dependent on the Molière radius (r_M). For a Molière radius of 100 m, the angular image size is 0.6° at a distance of 10 km, and 1.1° at a distance of 5 km [138]. As such the size of the spot due to the optics of the detector as well as due to the transverse dimensions of the shower must be taken into account.

8.2.1. Optical Spot

The spot has been calculated from simulations that take into account the complete optics of the camera, including the camera shadow and the corrector rings. The simulated spot is different for different angles of incidence due to the relative positions of the camera shadow

and the corrector ring optics. Using these simulations the fraction of signal detected by each pixel has been calculated, which can be converted to the number of expected ADC counts using the pixel absolute calibration constants.

One method to check the reliability of the model is by using laser shots from the CLF [139]. As the average distance from the CLF to the FDs is 30 km, the laser shots can be considered as line sources, but multiple scattering of fluorescence light must now be taken into account as it smears the spot on the camera surface. When comparing the spot model to the data from the laser shots, Verzi et al. [144] enlarged the optical spot by a constant factor of 1.5 to account for the multiple scattering, and attained good agreement with the data.

8.2.2. Lateral Width of Shower

At any time, the light arriving at the detector in that instant is made up of light from different directions and slightly different shower development stages. Using the Gora parametrisation mentioned in section 7.1, the effect of the lateral shower width on the shower image can be calculated and therefore taken into account. As the parametrisation is a function of shower age, the calculated fraction of light within each pixel, and hence the number of ADC counts, is now dependent on the Gaisser-Hillas fit to X_{max}.

8.2.3. Mercedes Correction

The spot model takes into account camera inhomogeneities due to the presence of the Mercedes that border the PMTs (refer to section 4.2). The inhomogeneities are largely due to the slight inefficiency of the cones reflecting the light into the PMTs due to the Mylar reflection. The model takes into account the number of photons that enter the PMT without reflection off Mercedes, compared to the number of photons that are reflected by the Mercedes onto the PMT, and includes the Mercedes efficiency which has been measured to be 0.80 [140]. This efficiency is dependent on X_{max}, as it depends on the lateral width of the shower. This work showed that, in correcting for the Mercedes, the PMT signal could be from 8 % higher to 13 % lower depending on the position of the spot. As this will be different for each spot position within a shower track the overall effect on an entire shower should be negligible.

8.3. Investigation of the spot model

As discussed in Chapter 7, there appears to be light of an unknown origin that has not been taken account of in the reconstruction process. This light exists outside the angle ζ_{best}, and it still exists after corrections for the shower's lateral width, multiple scattered fluorescence light and singly scattered Cherenkov light had been made. Tests using lasers [130], UV point light sources [142, 143], and by monitoring star tracks across the camera also showed the existence of this halo, which largely ruled out the source being shower orientated. This means that the halo should not depend on the distance to the shower or shower age, which were parameters that the corrections mentioned above were strongly correlated with. One cause for concern, is that the halo observed in the standard reconstruction method, and the spot model prediction of the halo, result in different shapes and magnitudes for this halo [144]. This is confusing as the spot model was tested with real data.

To try and understand the differences between the spot reconstruction method and the standard reconstruction method, I obtained the data for over 6000 bright showers, as well as the spot model's prediction of the light from Valerio Verzi through private communication. Figure 8.1 is a histogram of the light flux from all of the showers, in units of 370 nm equivalent photons, as a function of angular distance from the shower track across the camera, ζ. The light flux from each 100 ns time bin has been summed, so the resulting histogram is the average shape of the light distribution as recorded by the FDs. Also shown are the spot model's predictions for the distribution of the various components of light as functions of angular distance from the shower track. The crosses represent the shower data, and the solid black line is the total spot model which is the sum of all of the components of light, listed in the legend. It can be seen that there is a fairly good agreement between the shower data and the model's predictions. The only slight discrepancy that is visible from this figure is, maybe, a slight overestimation by the model of the tail of the light distribution.

The events that make up figure 8.1 have a range of different geometries. As such the light from each time bin of each event will have a different angular distribution, due to the light arising from different shower evolutions and a range of distances from the detectors. The spot model takes into account age and distance dependent factors, such as the lateral width of the shower and the fraction of multiple scattered light (both fluorescence and

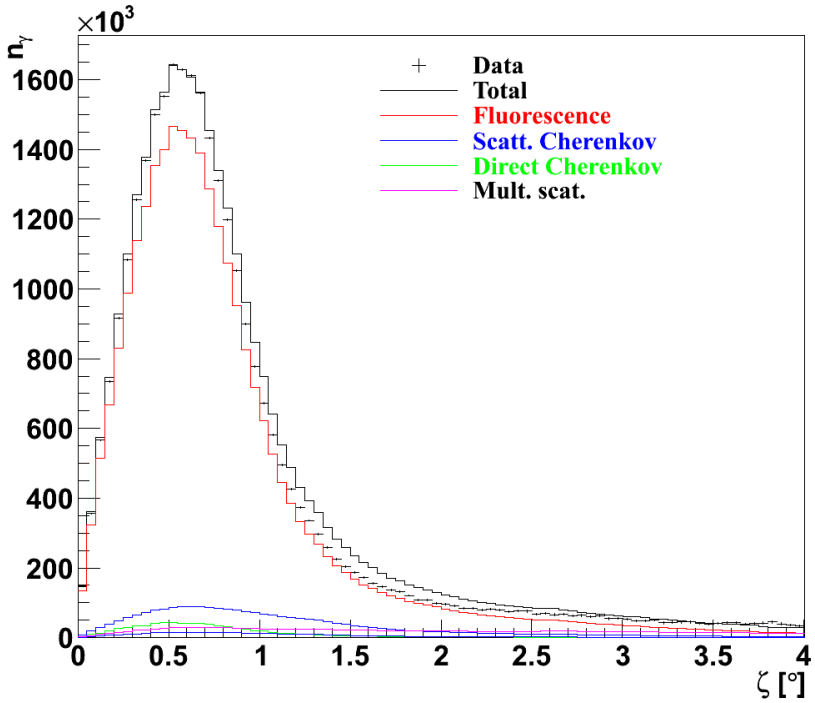

Figure 8.1.: The number of 370 nm equivalent photons as a function of angular distance from the shower track. This is the sum of the light from every 100 ns time step in over 6000 bright events. The crosses represent the shower data, and the solid black line is the spot model prediction of the light distribution. The individual components of the model; the direct fluorescence, multiply scattered fluorescence, direct Cherenkov and scattered Cherenkov are also indicated by the other solid lines. The figure was produced using data and code obtained via private communication [145].

Cherenkov), so there shouldn't be any differences between the shower data and the spot model as a function of shower age and distance.

However, when comparing the data and the model for specific shower ages, I found that the agreement started to fail at large shower ages. Figure 8.2 shows the angular distribution of direct fluorescence light for four different stages of shower evolution. The red line represents the spot model's prediction of the distribution and the green line is the direct fluorescence distribution taken from the data. The top right plot is for light from shower ages between 1.1 and 1.2, for which there is good agreement between the data and the

model but, as the shower ages increase, the disagreement becomes apparent. It seems that the model begins to under-predict the magnitude of the tail of the distribution, and over predict the light at the peak of the distribution.

What I would like to compare is the direct fluorescence component of the model, with the shower data once all non-direct fluorescence components have been subtracted away. Looking at age intervals of 0.1, between 0.6 and 1.4, I calculated the fraction of light between 1.4°and 4.0° for the shower data and the spot model predictions. This is plotted in figures 8.3 and 8.4. Figure 8.3 shows that the model underestimates the magnitude of the halo for showers at ages greater than 1.2, and overestimates for ages less than 1.2. Similarly, figure 8.4 shows that the model underestimates the magnitude of the halo for shower distances less than 10km, and overestimates for shower distances greater than 10km.

To try and understand the possible reasons for these age and distance dependent differences between the spot model and the shower data, my findings were sent to Valerio Verzi [145] and I received a reply with two possibilities. The first was that the larger than predicted halo for nearby showers and large shower ages may be due to incorrect modelling of the scattered Cherenkov lateral width. As the lateral width of Cherenkov light has been determined from Monte Carlo work by Giller [137], and also empirically in Chapter 7 of this thesis, and the two independent methods predict the same age dependence, I do not feel that the Cherenkov light is the source of the halo. Another suggestion was that a problem with the Gora parametrisation [125] of the lateral width of the fluorescence light could not be ruled out. In fact, as the Gora parametrisation only extends to $s(X) = 1.2$, the spot model used the lateral width at $s(X) = 1.2$ and applied it at larger ages. This is not what has been done in the standard reconstruction method, where the lateral width correction was applied at all shower ages, despite the fact that the correction was only developed for shower ages up to 1.2. When looking back at figure 8.3, this looks like the culprit. The halo predicted by the spot model remains constant at and above ages of 1.2, whereas the halo in the data continues to increase. The inverse can be seen for ages less then 1.2, where the model over predicts the halo. The result is that on average the model fits the data, but there is an age dependent difference between the two, illustrated in figure 8.5.

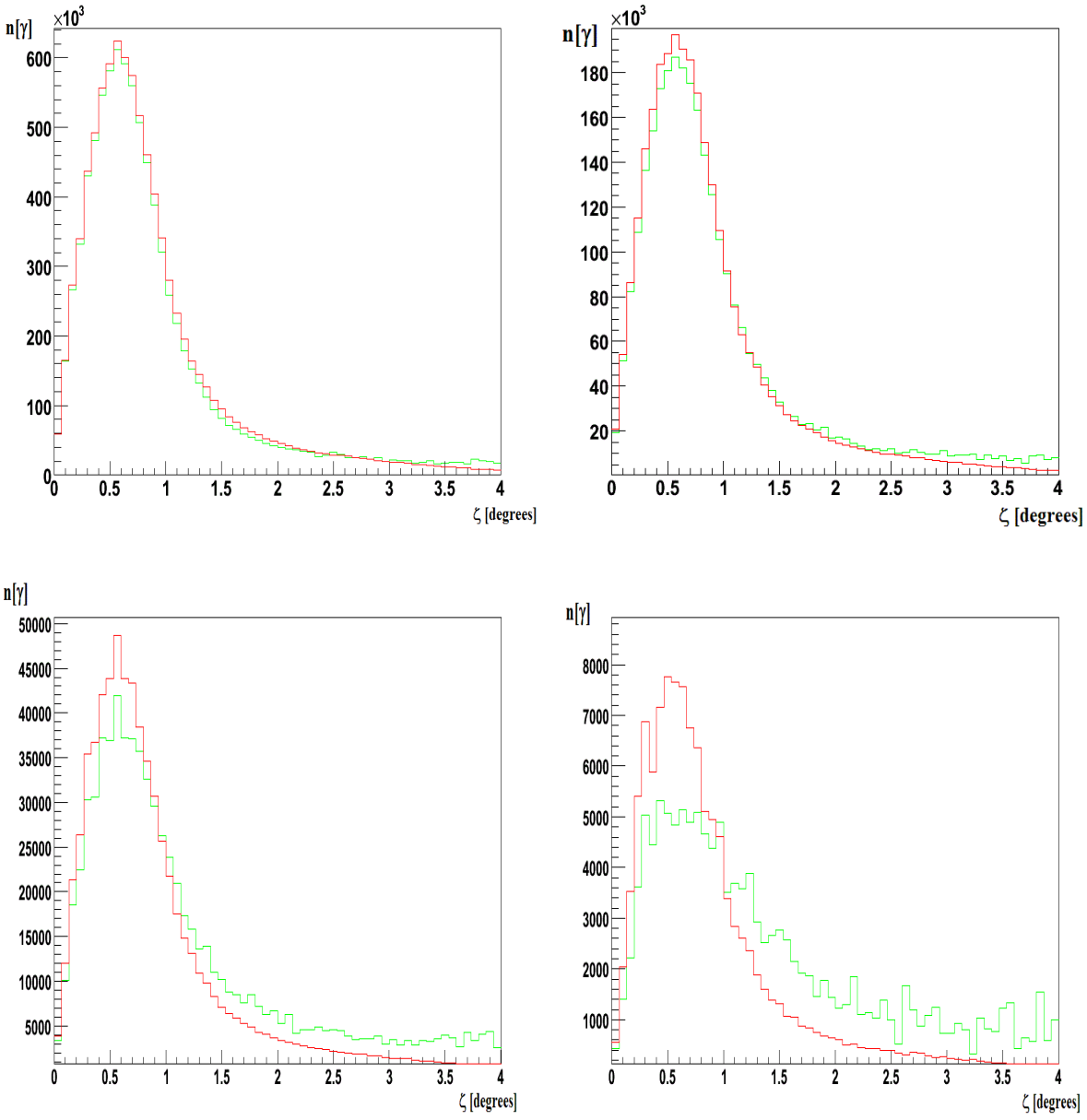

Figure 8.2.: The green line represents the average distribution of direct fluorescence light from the shower data, and the red line is the spot model's prediction of that distribution. The four plots correspond to data from 4 different shower age brackets. Top right: 1.1−1.2, Top Left: 1.2−1.3, Bottom Right: 1.3−1.4, and Bottom left 1.4−1.5.

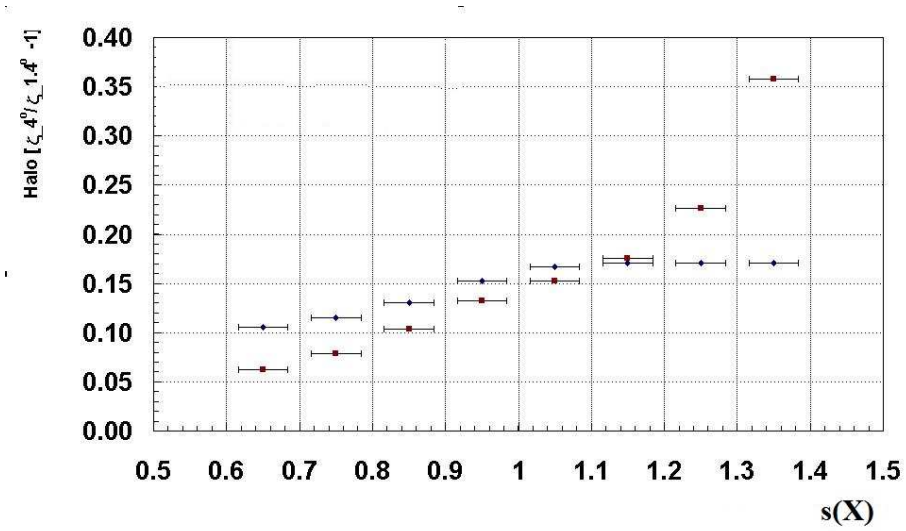

Figure 8.3.: The fraction of light between 1.4° and 4.0°, for ages 0.6 to 1.4, from the spot model's prediction of the fluorescence compared to the data from over 6000 high quality events. The red squares represent the data halo, and the blue diamonds represent the spot model's prediction of the halo.

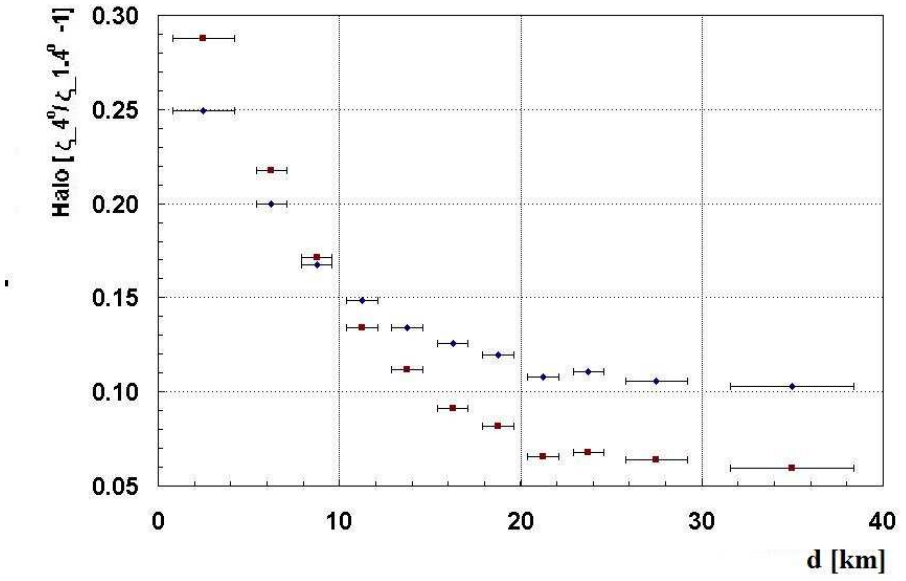

Figure 8.4.: The fraction of light between 1.4°and 4.0° as a function of shower distance, from the spot model's prediction of the fluorescence compared to data from over 6000 high quality events. The red squares represent the data halo, and the blue diamonds represent the spot model prediction of the halo.

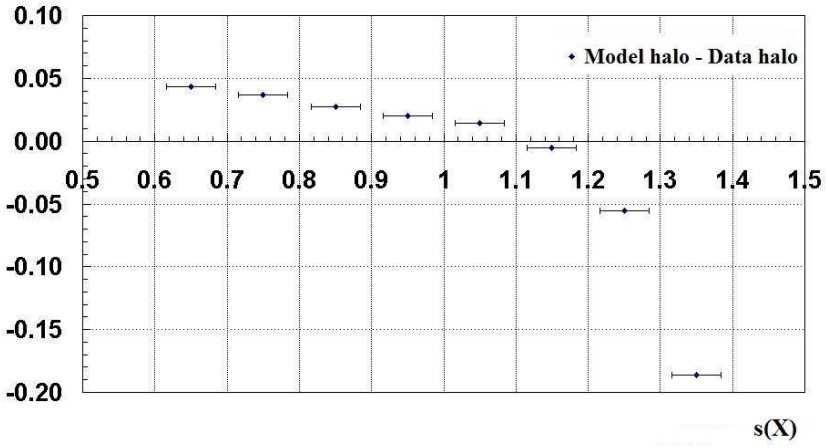

Figure 8.5.: The difference between the fraction of light between 1.4°and 4.0°as a function of shower age as calculated from the spot model prediction of the fluorescence and from the data for over 6000 high quality events.

The parametrisation of the shower lateral width needs to be checked at larger shower ages before it can be applied in the spot model. It is important to check that it is valid at larger shower ages, as it is currently implemented in the standard reconstruction algorithm for all shower ages. In the following sections, the method for calculating the lateral width of the energy deposit in showers will be introduced, and the current lateral width parametrisation will be discussed in detail. Finally I will conduct the same procedure to create a new lateral distribution function that accounts for ages up to 1.5.

8.3.1. CORSIKA

CORSIKA is a Monte Carlo program package [146], that simulates the development of EAS induced by a variety of primary particles, up to the highest energies. The particle interactions are calculated using external codes that can be specified by the user. There are separate codes used for high and low[1] energy hadronic interactions. The models for the high energy hadronic interactions come from extrapolating cross-section, multiplicity and elasticity information of the interactions measured using accelerators at the lower energies. The uncertainty that this introduces into energy determination by fluorescence detectors is small, as the main characteristics of the energy released in the shower comes from the interactions undergone by the electromagnetic component.

The models chosen in previous work on the lateral distribution of energy deposit [147, 124], are the models that I have also chosen to use here. These are the QGSJET01 model for the hadronic interactions with $E_{lab} > 80\,\mathrm{GeV}$ [16], and GHEISHA for hadronic interactions for $E_{lab} < 80$ GeV [167].

8.3.2. Particle Thinning

A detailed simulation of all secondary particles produced within an EAS is impossible, so thinning techniques need to be applied to keep CPU times and particle output files to manageable levels (10^{13} secondaries in a 10^{20} eV shower [148]). The thinning algorithm samples the shower by following representative particles and weighting them accordingly,

[1] $E_{lab} < 80$ GeV

and then discards the remaining secondaries [149]. CORSIKA allows the user to specify the fraction of the initial energy at which to begin thinning. Artificial fluctuations introduced by thinning are reduced by introducing optimum weight limitations [150], in which different weight limits are set for the electromagnetic, hadronic and muon components.

Optimised thinning in this work occurs for an initial energy fraction of 10^{-6}. This means that for an initial energy of $10^{19}\,\mathrm{eV}$ all particles are tracked until their energy falls below $10^{-6} \times 10^{19}\,\mathrm{eV} = 10^{13}\,\mathrm{eV}$. The thinning algorithm continues until the particle weights reach the weight limit. This is set to $(10^{-6} \times 10^{19}\,\mathrm{eV})\,(\mathrm{GeV})^{-1} = 10^{4}$ for the electromagnetic component, and 10^{2} for the hadronic and muon components. At this point the full simulation returns until another simulation threshold is reached. This second simulation threshold is an energy threshold, below which we no longer track the particles. This is because it is computationally expensive to track all low energy particles. When a particle's energy falls below this threshold, we deposit the energy from that particle at its current atmospheric depth. The total ionisation energy deposit is then the sum of ionisation energy from particles with $E > E_{thres}$ and the energy deposited at that depth from particles with $E < E_{thres}$. In this work, as in [125], the thresholds were set at 100MeV for hadrons and muons, and 0.25 MeV for electrons and positrons.

The reduction in CPU time and the size of output files, allows us to simulate many UHECR initiated air showers, and study the lateral distribution's dependence on the initial energy, and the magnitude of shower to shower fluctuations.

8.3.3. Calculation of Energy Deposit

8.3.3.1. Ionisation by tracked particles

The continuous ionisation energy loss of a charged hadron or muon is described by the Bethe-Bloch stopping power formula

$$\frac{dE_i}{dX} = \frac{z^2}{\beta^2}\kappa_1(ln(\gamma^2 - 1) - \beta^2 + \kappa_2) \tag{8.2}$$

where $\beta = v/c$, γ is the particle's Lorentz factor, and z is the charge of the particle in units of e. The constants $\kappa_1 = 0.153287\,\mathrm{MeV}g^{-1}$ and $\kappa_2 = 9.386417$ come from [151], and they are for a medium of dry air.

For the electrons and positrons, the ionisation energy loss is described by the EGS4 code, and is modified in CORSIKA to account for the pressure dependent Sternheimer correction [152]. The continuous energy loss for these particles comes from soft Bremsstrahlung of photons below E_{thres}, and from ionisation energy losses, for which the concept of 'restricted stopping power' is applied [153].

8.3.3.2. Below the energy threshold

The energy released by sub-threshold particles will depend on the particle type. Stable particles, such as electrons, cannot release more than their kinetic energy, so the released energy is $E_r = E_{kin}$. Positrons can annihilate, and therefore $E_r = E_{kin} + 2m_e$. If any products from annihilation have $E > E_{thres}$, then these particles are tracked until they fall below E_{thres}.

Muons and mesons are unstable particles and can release a fraction of their rest mass into ionisation, and some energy is also carried away by neutrinos. Anti-baryons annihilate with a nucleon under the emission of several pions, and the releasable energy is then the kinetic energy, plus the rest mass of the anti-baryon and the nucleon. For unstable particles and anti-baryons we assume an effective fraction of 1/3 of their releasable energy to be taken into account in determining the total energy release [147], and 2/3 is lost mainly to neutrinos.

Another assumption that is made in the CORSIKA simulation, is that the energy released by particles below the energy threshold can be deposited at the depth at which they cross the energy threshold. This is found to be a valid assumption for the energy cuts applied here, and even if the energy cuts were to be increased by a factor of 10, the particles would still be stopped within a few $\mathrm{g\,cm^{-2}}$.

8.4. Previous Parametrisation of the LDF

In this section I will present previous simulations of the lateral distribution function performed by D. Gora [125]. This is the lateral distribution function currently implemented by the Auger Collaboration in the fluorescence detector reconstruction procedure. The energy, zenith angle, and composition dependence were simulated at 10^{19} eV and 10^{20} eV, and then the final lateral distribution function was parametrised using 1000 vertical (zenith angle = 0°) proton showers at 10^{19} eV. All plots presented in this section come from [125].

8.4.1. Energy and Composition Dependence

Gora found that there was only a slight dependence of the integral of the energy deposit over radius on primary composition and energy, which can be seen in figure 8.6 (A). This dependence is reduced even further when plotting the distance from the shower axis in Molière radii units (refer back to section 3.3), shown in 8.6 (B). This is due to the fact that for a given shower geometry, proton and iron showers will on average maximise at different depths, and hence the Molière radius will be different for the iron and proton showers at any given age. Since the Molière radius determines the lateral spread of the particles, iron induced showers have a broader lateral distribution at the same shower age.

8.4.2. Zenith Angle Dependence

The dependence on shower zenith angle was also investigated. Once again, extensive air showers of the same energy and composition, will reach the same stage of evolution at different depths due to their zenith angles. This is displayed in figure 8.7 (A). When the energy deposit is then plotted as a function distance in Molière radii units, this zenith angle dependence is less apparent.

The conclusion from [125] was stated as: "the lateral shape of the energy deposit density versus distance from shower axis measured in Molière units is independent of the primary

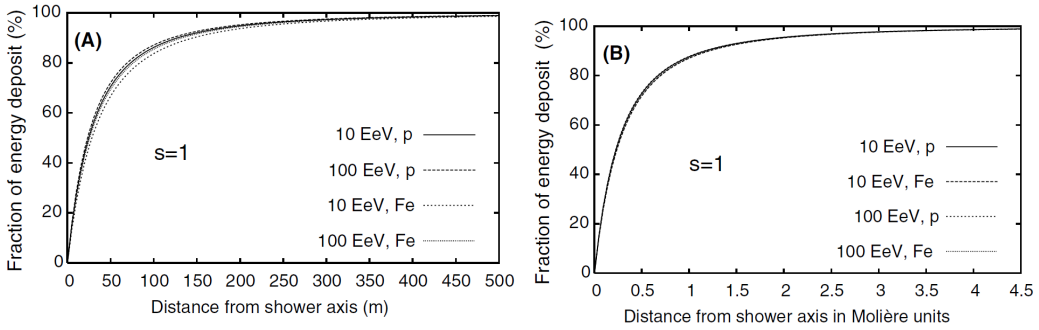

Figure 8.6.: (A) shows the integral of energy deposit at s=1.0, for iron and proton vertical showers at 10^{19} eV and 10^{20} eV, as a function of distance from the shower axis. (B) is the same plot, but with the distance from the shower axis in Molière radii units [125].

energy, primary particle type and zenith angle. It depends, to a good approximation, only on the shower age". Equation 7.4 describing the lateral width $F(r^*)$ from section 7.2 was fitted to the lateral distribution of energy deposit as a function of distance from the shower axis in Molière radius units. The fit parameters a and b were determined as functions of shower age, and are displayed below, and are plotted in figure 8.8.

$$F\left(r^*\right) = 1 - \left(1 + a\left(s\right)\, r^*\right)^{-b(s)},\; r^* = \frac{r}{r_M}$$

$$a(s) = 5.151\, s^4 - 28.925\, s^3 + 60.056\, s^2 - 56.718\, s + 22.331 \tag{8.3}$$

$$b(s) = -1.039\, s^2 + 2.251\, s + 0.676. \tag{8.4}$$

8.5. Extending to larger ages

The initial parametrisation of the lateral distribution of energy deposit was performed for shower ages up to 1.2, and the energy and composition independence checks were only

conducted at 10^{19} eV and 10^{20} eV. The showers used to create the age dependent parameters within the LDF were vertical proton initiated showers with $E = 10^{19}$ eV. At this energy the showers run into the ground before larger shower ages can be observed, but for inclined showers we observe a larger range of maximum shower ages and the parametrisation needs to be extended to include data from ages greater than 1.2. Also iron showers at this energy will maximise higher in the atmosphere, meaning that we will view more of the shower beyond shower maximum, and showers with an energy lower than 10^{19} eV will most likely be observed at larger ages. Blindly extending the functions $a(s)$ and $b(s)$ to larger shower ages, we observe that $b(s)$ turns over just before $s(X) = 1.2$ (see figure 8.9) .

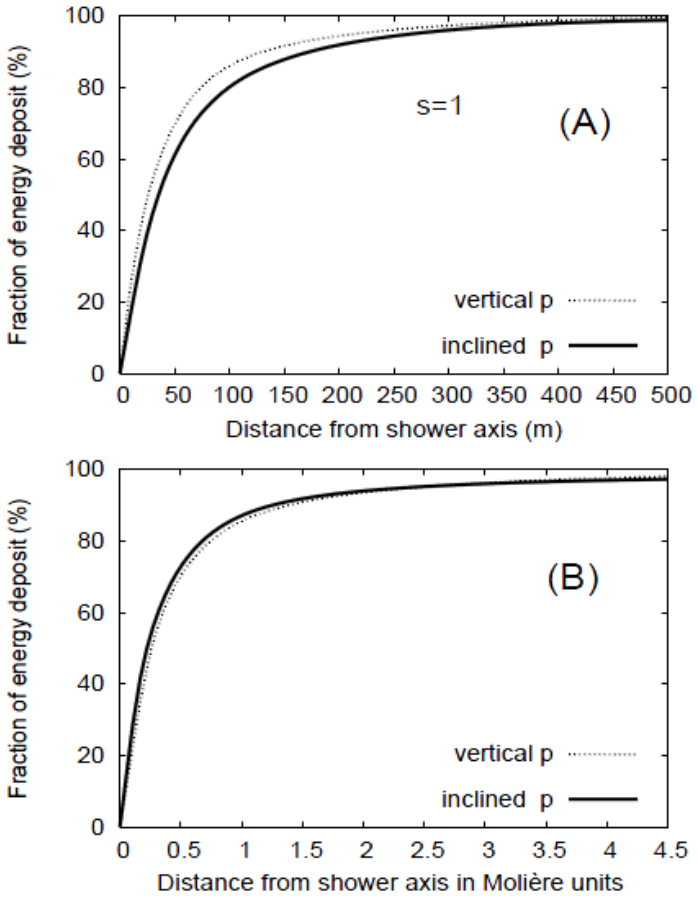

Figure 8.7.: (A)Integral of energy deposit density over radius versus distance from the shower axis for vertical and inclined ($\theta = 45°$) proton showers. (B) The integral profile measured in Molière units. The profiles are shown for 10 EeV showers at s=1 [125].

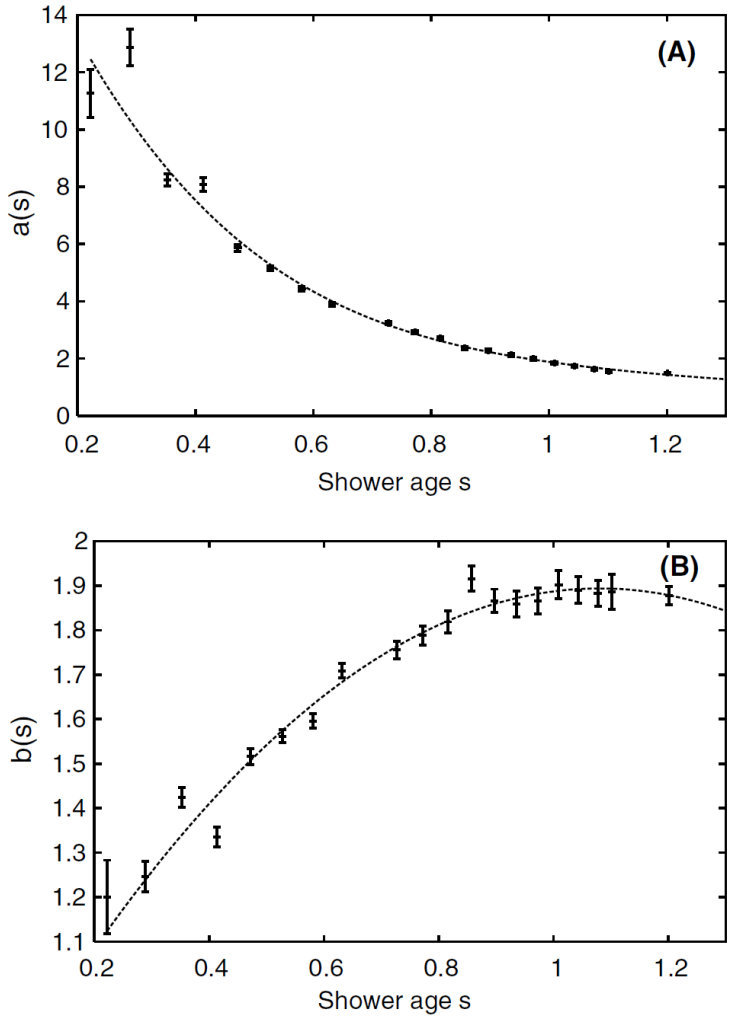

Figure 8.8.: Values of parameters a(s) and b(s), obtained based on integral of CORSIKA energy deposit density for vertical proton showers of energy 10 EeV [125].

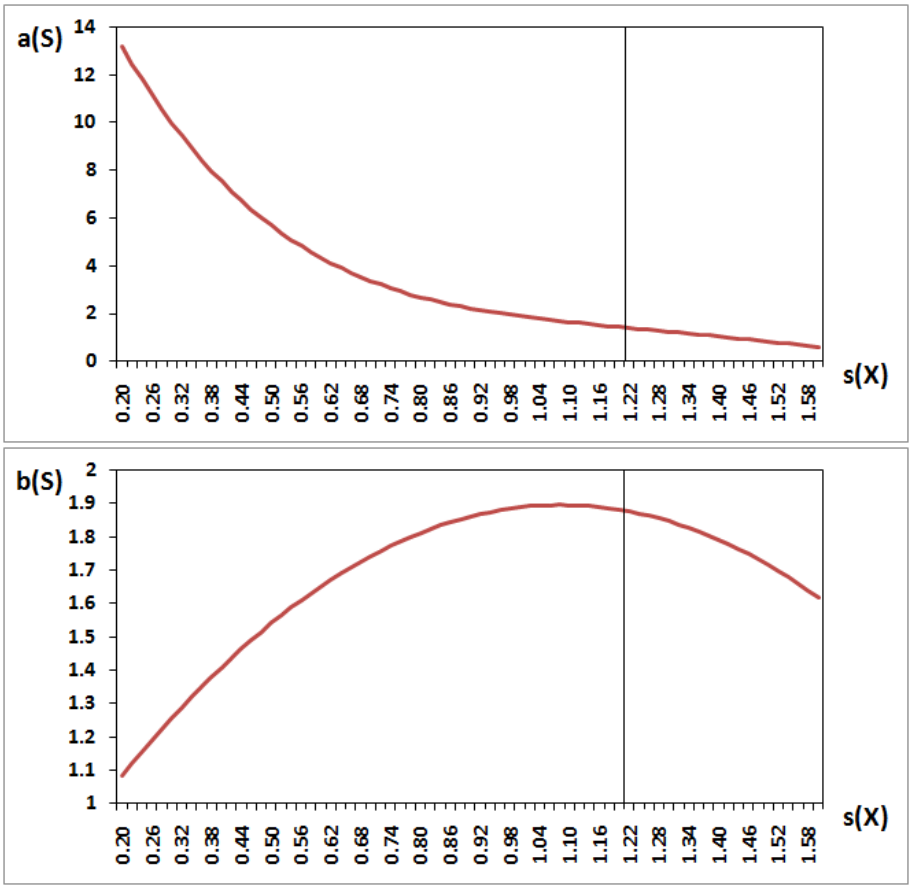

Figure 8.9.: Functions a(s) and b(s) plotted for s(X)$\in$ $[0.2, 1.6]$. The black line at $s(X) = 1.2$ indicates the limit of the Gora parametrisation.

8.6. Checking Universality of Correction

A convenient choice of primary particle for observing large shower ages are iron nuclei at 10^{17} eV. This is because they maximise high in the atmosphere and can be observed at large shower ages. The average simulated energy deposit as a function of distance from the shower axis in Molière radii units is displayed in figure 8.10 for six age ranges. An age dependence in the lateral energy deposit is observable out to ages of 1.5. The data presented in sections 8.6 and 8.7 are the results of simulations that I have performed using CORSIKA.

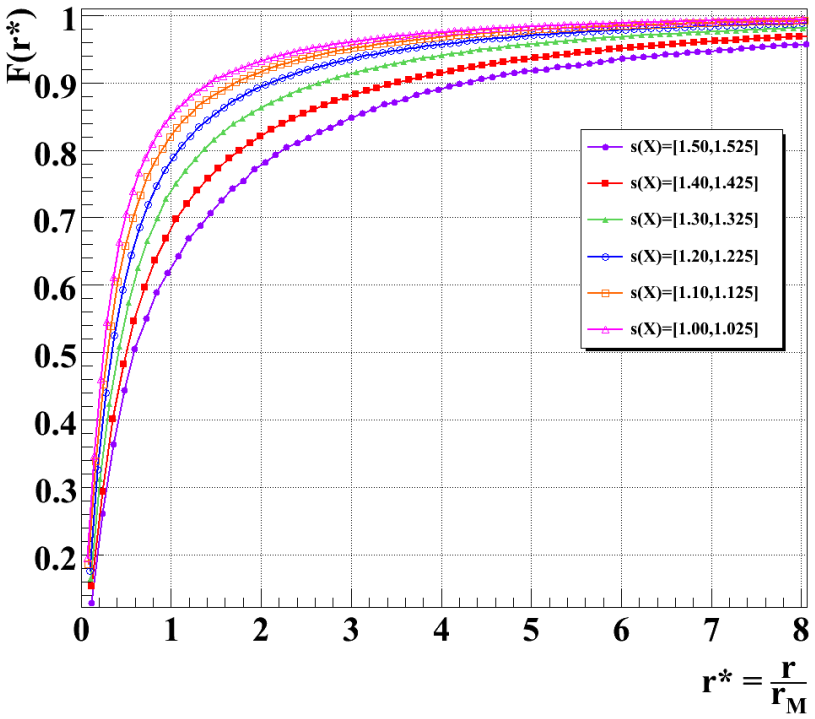

Figure 8.10.: The integral of the lateral energy deposit as a function of distance from the shower axis in Molière radius units. The profiles are averages for different age ranges as indicated. The primary particles were iron nuclei with an energy of 10^{17} eV.

As it has been noted that there is a slight difference between iron and proton showers in terms of their lateral energy deposit, I believe that it is best practise to use a mixture of showers at different energies and compositions to construct a universal parametrisation.

8.6.1. Composition and energy independence down to 10^{17} eV

Figures 8.11, 8.12 and 8.13 show the lateral energy deposit as a function of distance from the shower axis, in Molière radii units, for three different shower age ranges. In each plot, the lateral energy deposit calculated using 10^{17} eV and 10^{19} eV proton, and 10^{17} eV and 10^{18} eV iron nuclei primary particles are shown. There is very little difference in results for different energies and compositions. From this point I proceeded with using data from all energies and compositions to determine the age dependent parameters in the lateral distribution function.

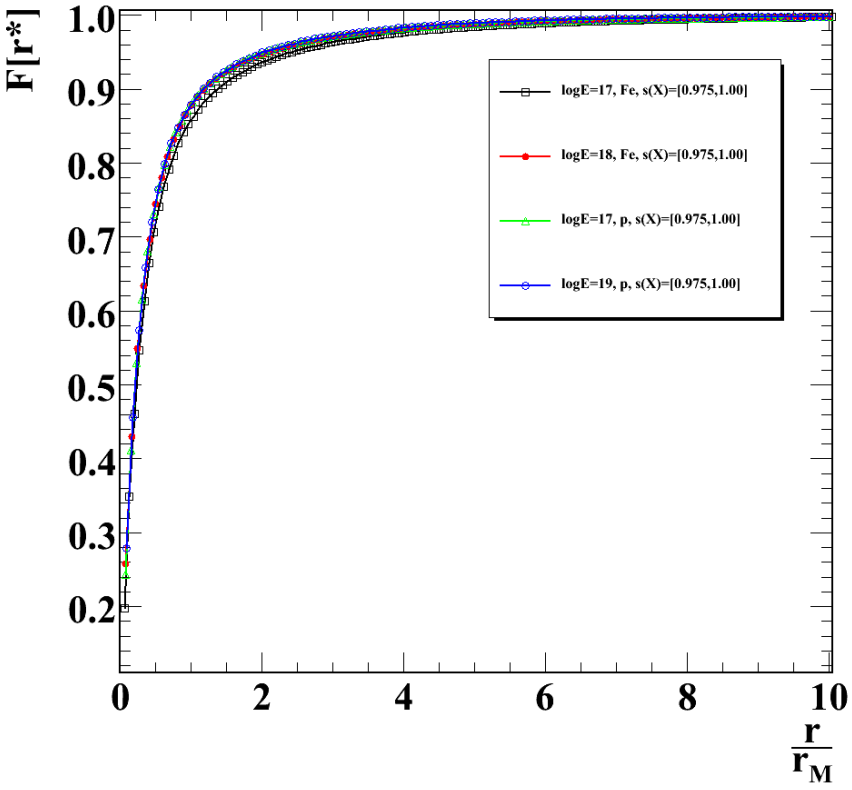

Figure 8.11.: The integral of the lateral energy deposit as a function of distance from the shower axis in Molière radius units. The profiles are averages for different energies and compositions within the age range of $s\,(X) \in [0.975, 1.000]$.

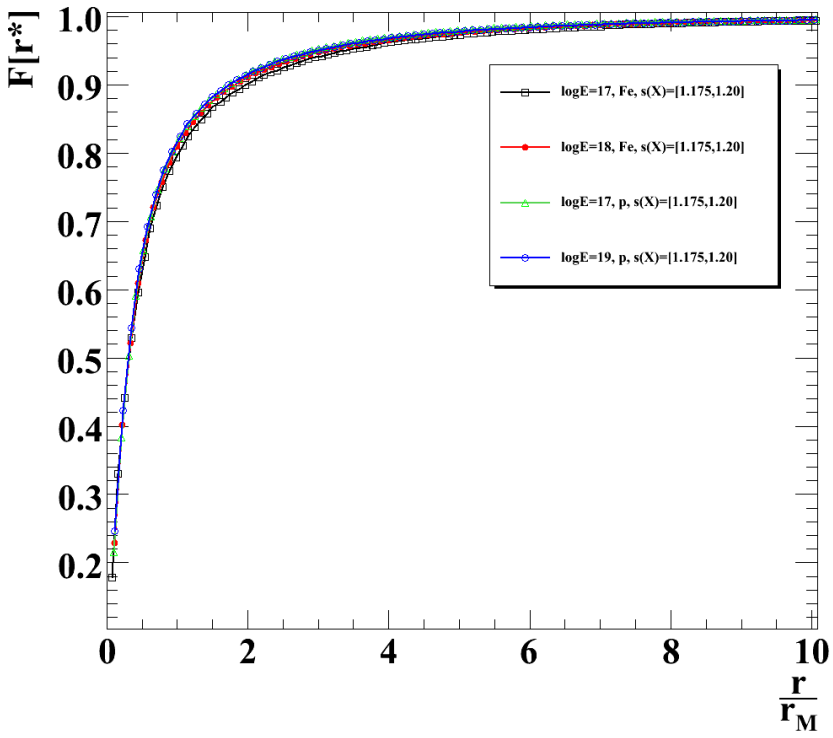

Figure 8.12.: The integral of the lateral energy deposit as a function of distance from the shower axis in Molière radius units. The profiles are averages for different energies and compositions within the age range of $s(X) \in [1.175, 1.200]$.

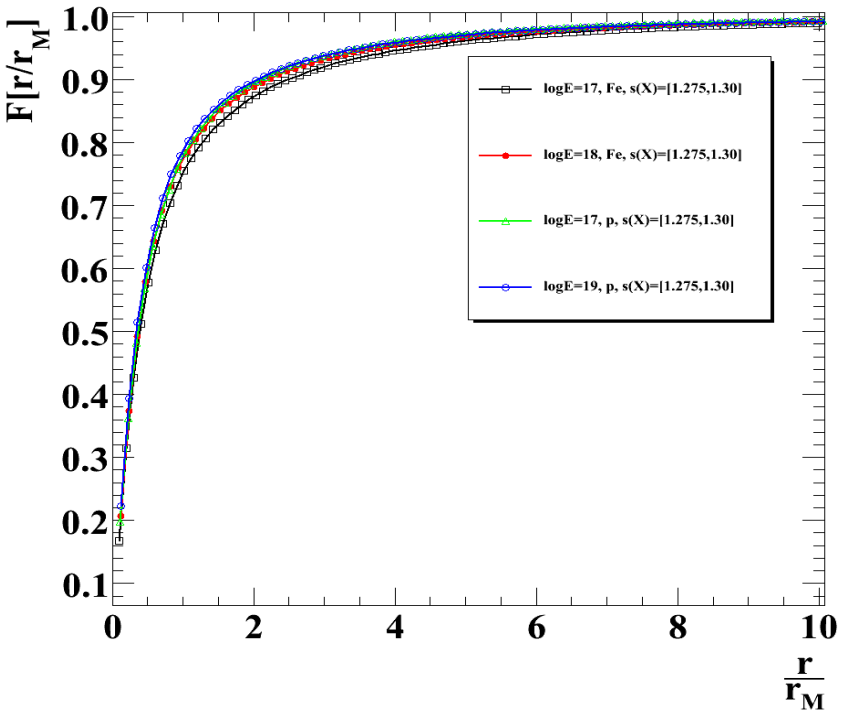

Figure 8.13.: The integral of the lateral energy deposit as a function of distance from the shower axis in Molière radius units. The profiles are averages for different energies and compositions within the age range of $s\,(X) \in [1.275, 1.300]$.

8.7. Comparing with past parametrisation

To create my own age dependent parameters to equation 7.4 (see section 7.1 or more recently sub-section 8.4.2), I produced fits to the lateral distribution of energy deposit for shower ages ranging from 0.2 to 1.5, using data from both iron and proton induced showers at energies ranging from 10^{17}eV to 10^{19}eV. Figures 8.14 and 8.15 show the age dependent parameters that I have determined from fitting equation 7.4 to the data, as well as the values of these parameters from the past parametrisation. It should be noted that while I have plotted the values of $a(s)$ and $b(s)$ from Gora's parametrisation for all ages, the initial parametrisation only extends to 1.2 and makes no claims to extend to larger shower ages.

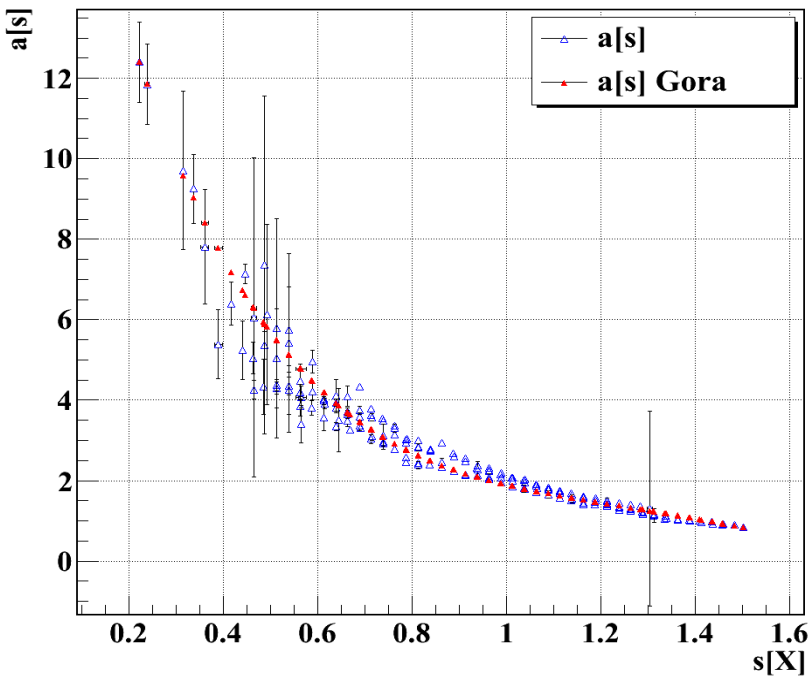

Figure 8.14.: The parameter a as a function of shower age. The blue data points represent the results of my fits to the integral energy deposit, and the red markers represent the corresponding value obtained from Gora's parametrisation.

While the fit parameters are slightly different to those determined by Gora at the highest ages, the lateral width corrections that they yield are approximately the same. This means

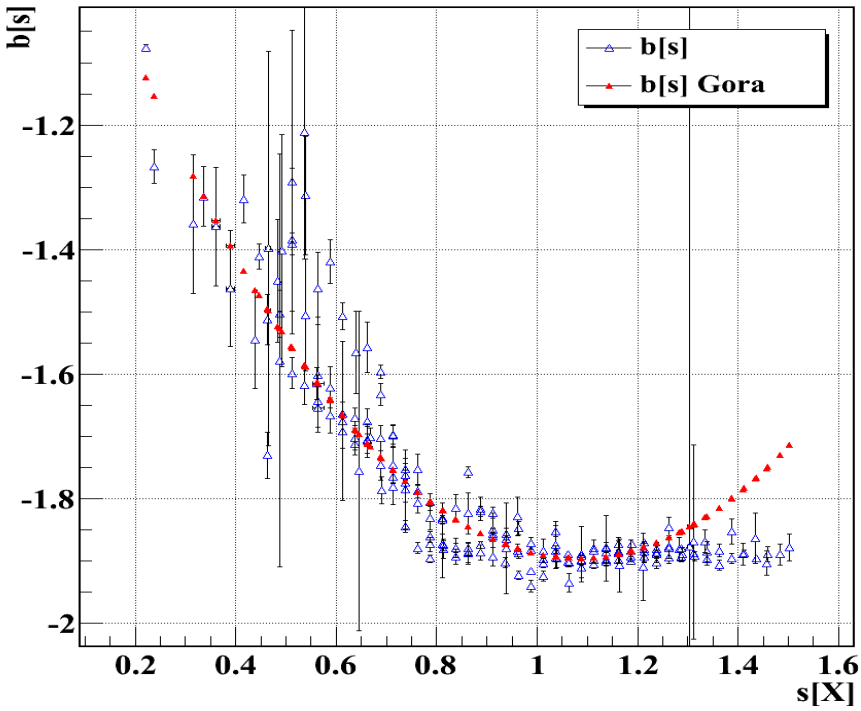

Figure 8.15.: The parameter b as a function of shower age. The blue data points represent the results of my fits to the fraction energy deposit, and the red markers represent the corresponding value obtained from Gora's parametrisation.

that the initial parameterisation is valid down to energies of 10^{17}eV, and up to ages of 1.5.

8.8. Conclusions

While there was no difference found between the parametrisation determined from this work and the current parametrisation implemented in the $\overline{Offline}$, the parametrisation can now be used with confidence for shower energies ranging from 10^{17}eV to 10^{20}eV, and for shower ages up to 1.5. This is important as it verifies that the current lateral width correction can continue to be used for large shower ages and lower shower energies. It also shows that the disagreement between the two main construction methods is not due to the fluorescence lateral width. In the spot model, the Gora correction can now be applied for shower ages greater than 1.2. This should remove the age and distance dependence in the

disagreement between the two methods, as the disagreement was due to the spot method applying the lateral width correction at shower ages larger than 1.2 with the value of the correction at 1.2. This then caused the halo to be underestimated at the larger ages, and as a result of ensuring that on average their model fit the data, they overestimated the halo at the lower ages.

9. Conclusion

In this thesis I have investigated several systematic uncertainties in the energy reconstruction of extensive air showers induced by ultra high energy cosmic rays. I have presented solutions and ideas for reducing these uncertainties, that are applicable to both the Pierre Auger Southern Observatories fluorescence detectors, and will be relevant to the Auger North fluorescence detectors in the future.

I initially investigated the effect of atmospheric vapour pressure on the fluorescence yield, and developed monthly vapour pressure profiles that reduced the uncertainty associated with the previous seasonal profiles. I classified data taken from radiosonde launches based on the cloud conditions at the time of launch and subtracted those conducted during overcast conditions. This had the effect of reducing the magnitude of the correction as well as reducing the uncertainty in the vapour pressure profiles. I then determined methods for reducing the uncertainty further by using data from weather stations and IR monitors in conjunction with the monthly models.

Secondly I studied the process of light collection at the Fluorescence Detectors and the interpretation of that light. I identified a halo of light around shower tracks on the FD cameras and determined the source of this light to be scattered Cherenkov light as well as light from an undetermined source. Finally, I parameterised the halo and accounted for it in the reconstruction process. The overall effect on the reconstructed shower energies was 4 % and the change in energy was energy dependent. Another outcome of this work has been the shift in the calculated depth of shower maximum as a function of energy. This has reduced the elongation rate below $10^{18.5}$ eV. This parametrisation is an important

check for any theoretical models of the Cherenkov lateral distribution.

My last chapter addressed the disagreement between two FD reconstruction methods on the shape and magnitude of the undetermined halo around the shower track. Early in my investigation I discovered that the current lateral width parameterisation only extended up to shower ages of 1.2. It was constructed using simulated showers at energies of 10^{19}eV, and it's universality was only checked at 10^{19}eV and 10^{20}eV. Despite this, the standard reconstruction method was applying the parameterisation for all shower ages and energies. I followed the same method as this previous work and showed that the fluorescence lateral width parameterisation is valid for shower energies ranging from $10^{17} - 10^{20}$eV, and up to shower ages of 1.5. The extension to lower energies and larger shower ages will be important when reconstructing showers detected by Auger's low energy flluorescence detectors, HEAT. It also shows that the disagreement between the two main construction methods is not due to the fluorescence lateral width. Recently, advances have been made in determining the source of the halo. It has been found that light reflections from the PMT surfaces are contributing to the halo. This work is continuing, and it is an important uncertainty to understand for the reconstruction process.

A. Monthly vapour pressure profiles

These are the individual monthly box car vapour pressure models. The error bars represent one standard deviation around the mean. These are calculated from the spread of the individual launch data used for each model. The number of launches used to create each monthly profile are listed in table 6.7.

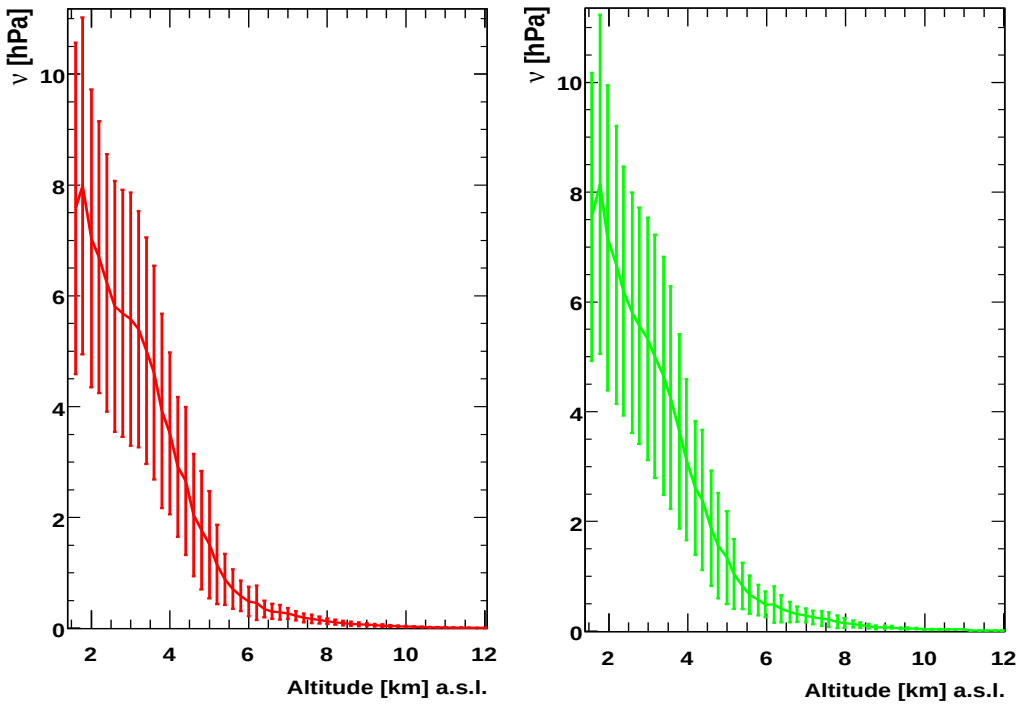

Figure A.1.: Monthly vapour pressure profiles for January and February. The error bars represent one standard deviation around the mean.

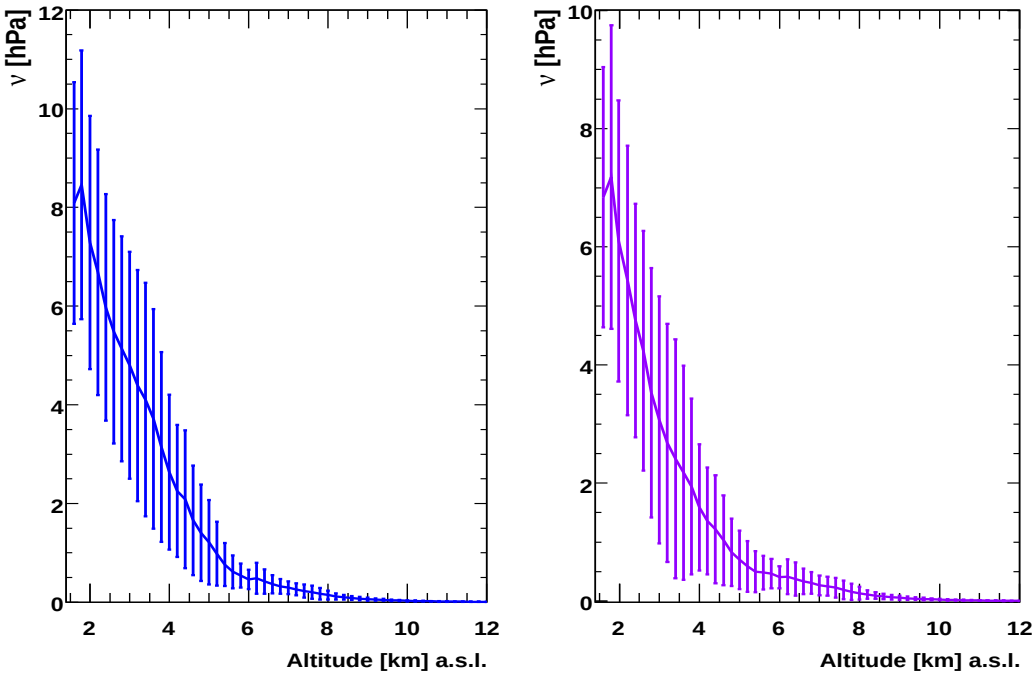

Figure A.2.: Monthly vapour pressure profiles for March and April. The error bars represent one standard deviation around the mean.

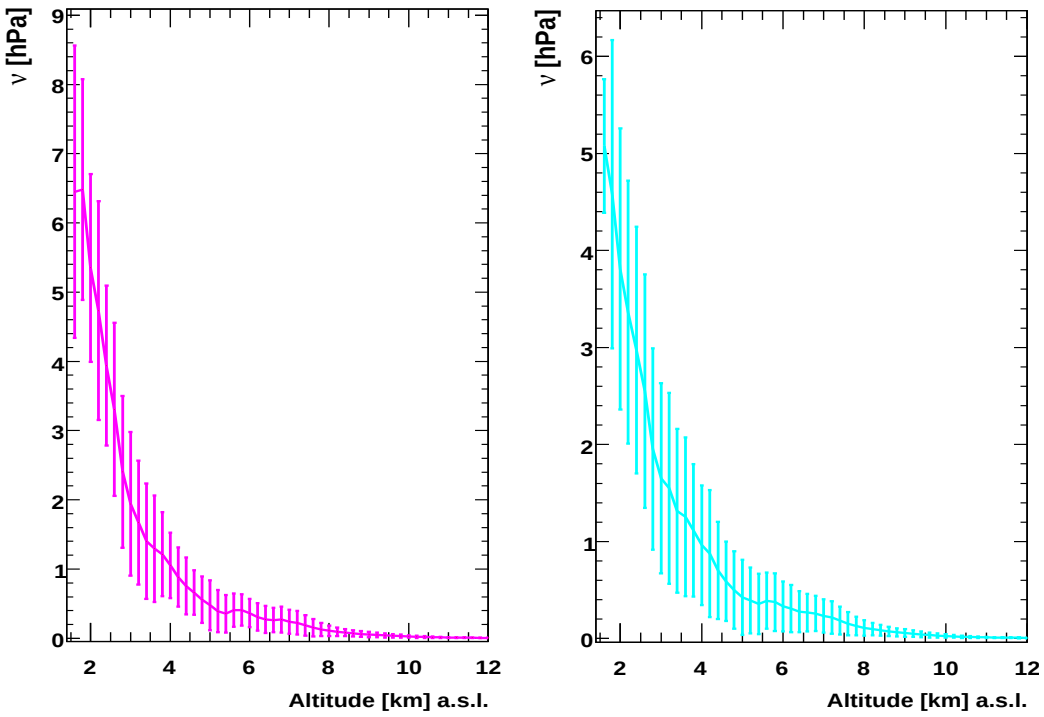

Figure A.3.: Monthly vapour pressure profiles for May and June. The error bars represent one standard deviation around the mean.

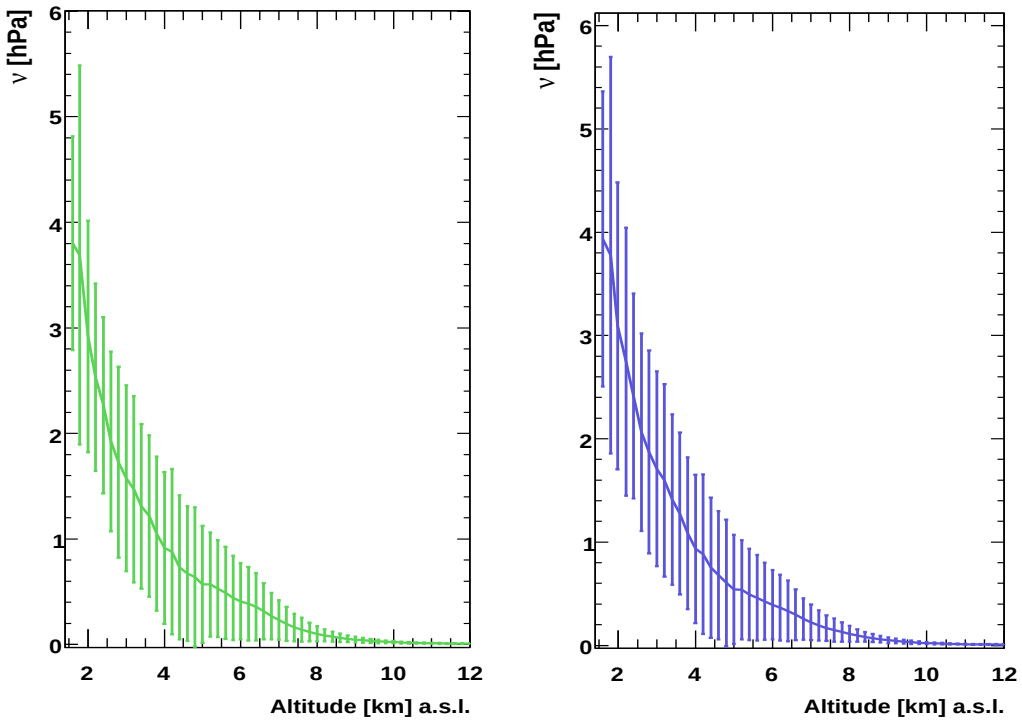

Figure A.4.: Monthly vapour pressure profiles for July and August. The error bars represent one standard deviation around the mean.

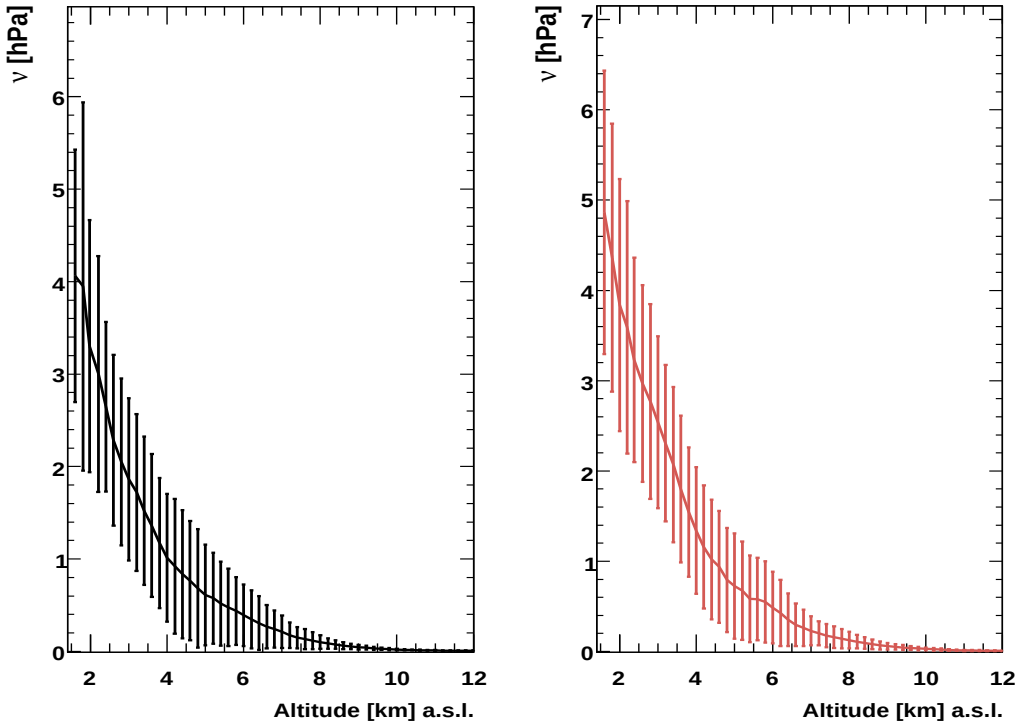

Figure A.5.: Monthly vapour pressure profiles for September and October. The error bars represent one standard deviation around the mean.

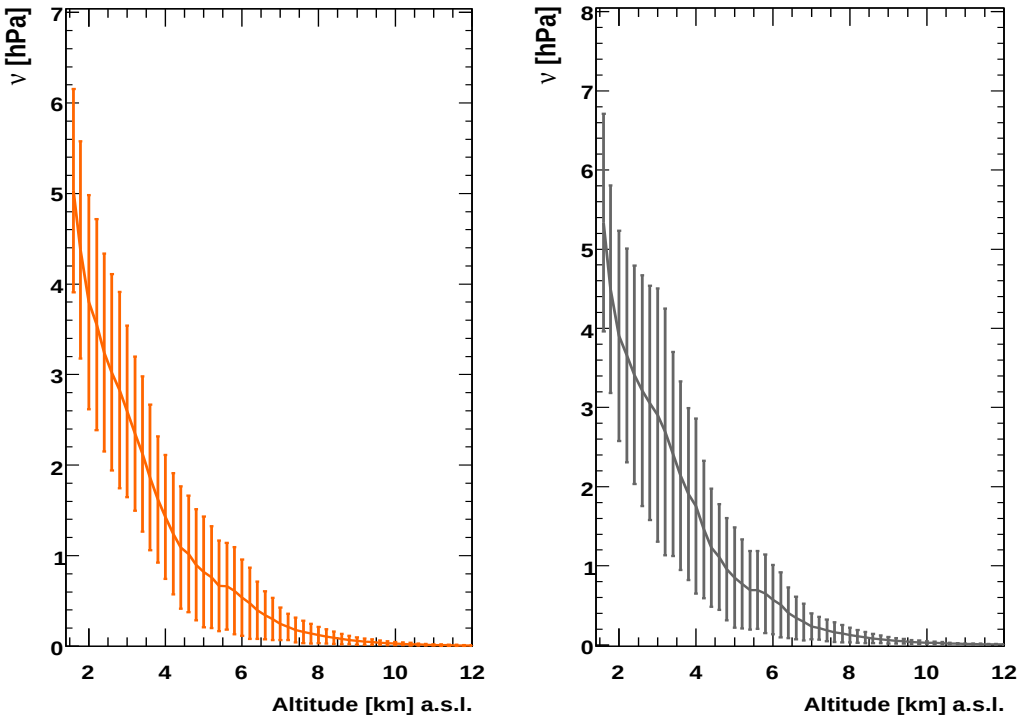

Figure A.6.: Monthly vapour pressure profiles for November and December. The error bars represent one standard deviation around the mean.

Bibliography

[1] T. Stanev, *High energy cosmic rays*, Springer 2004.

[2] V. Hess, Phys. Z., **13** (1912) 1084.

[3] P. Auger et al., Rev. Mod. Phys.,1 **11** (1939) 288.

[4] J. Linsley, Phys. Rev., **10** (1963) 146.

[5] J. Cronin, T.K. Gaisser, and S.P. Swordy, Sci. Amer., **276** (1997) 44.

[6] C. Amsler et al. Physics Letters B, **667** (2008) 1.

[7] G. Kulikov, G. Khristiansen, Sov. Phys. JETP, **35** (1959) 441.

[8] A. D. Erlykin, A. W. Wolfendale, J. Phys., G**23** (1997) 979.

[9] T. Antoni et al., Astropart. Phys., **24** (2005) 1.

[10] L.J. Gleeson, W.I Axford, Astrophys. J., **154** (1968) 1011.

[11] K. Greisen, Phys. Rev. Lett., **16** (1966) 748.

[12] Z. T. Zatsepin, V. A. Kuzmin, Zh. Eksp. Teor. Fiz. Pisma Red., **4** (1966) 144.

[13] D. De Marco, P. Blasi, A. V. Olinto, Astropart. Phys., **20** (2003) 53.

[14] The HiRes Collaboration, arXiv:astro-ph/0703099v2 (2008).

[15] KASCADE Collaboration, D. Heck et al., Proceedings of the 27^{th} International

Cosmic Ray Conference, Hamburg, **1** (2001) 233.

[16] N. N. Kalmykov, S. S. Ostapchenko, A. I. Pavlov, Nucl. Phys. B(Proc. Suppl.), **52** (1997) 17.

[17] D. Allard, E. Parizot, A. V. Olinto, Astropart. Phys., **27** (2007) 61.

[18] E. Fermi, Phys. Rev., **75** (1949) 1169.

[19] R. J. Protheroe, arXiv:astro-ph/9812055v1 (1998).

[20] M. Nagano, A.A. Watson, Rev. Mod. Phys., **72** (2000) 689.

[21] L. Drury, Contemp. Phys., **35** (1994) 232.

[22] A. M. Hillas, Ann. Rev. Astron. Astrophys., **22** (1984) 425.

[23] J. Bluemer, K. H. Kampert, Phys. Blatter, **56** (2000) 39.

[24] A. A. Penzias, R. W. Wilson, Astrophys. J., **142** (1965) 419.

[25] S. Yoshida, M. Teshima, Prog. Theor. Phys., **89** (1993) 833.

[26] R. J. Protheroe, P. Johnson, Astropart. Phys., **4** (1996) 253.

[27] J. P. Rachen, P. L. Biermann, Astron. Astrophys., **272** (1993) 161.

[28] V. S. Berezinsky, S. I. Grigoreva, Astron. Astrophys., **199** (1988) 1.

[29] F. W. Stecker, M. H. Salamon, Astrophys. J., **512** (1999) 521.

[30] P. Bhattacharjee, G. Sigl, Phys. Rep., **327** (2000) 110.

[31] J. L. Puget, F. W. Stecker, J. H. Bredekamp, Astrophys. J., **205** (1976) 638.

[32] G. R. Blumenthal, Phys. Rev. D, **1** (1970) 1596.

[33] N. Hayashida et al., Proceedings of the 26^{th} International Cosmic Ray Conference, Salt Lake City, **3** (1999) 256.

[34] P. P. Kronberg, Rep. Prog. Phys., **57** (1994) 325.

[35] AGASA Collaboration, Astropart Phys., **10** (1999) 303.

[36] W. Heitler, *Quantum Theory of Radiation*, Oxford University Press, 2nd edition, 1944.

[37] T. K. Gaisser, *Cosmic Rays and Particle Physics*, Cambridge University Press, 1990.

[38] J. Matthews, Astropart. Phys., **22** (2005) 387.

[39] K. Kamata et al., Suppl. Progr. Theor. Phys., **6** (1958) 93.

[40] J. A. J. Matthews, Pierre Auger Project Note GAP−1998−002.

[41] M. Takeda et al., Astropart. Phys., **19** (2003) 447.

[42] K. Greisen, Ann. Rev. Nucl. Part. Sci., **10** (1960) 63.

[43] T.K. Gaisser, A.M. Hillas, Proceedings of the 15^{th} International Cosmic Ray Conference, **8** (1977) 353.

[44] D. J. Bird et al. for the The HiRes Collaboration, Ap. J., **441** (1995) 144.

[45] AIRFLY Collaboration, Astropart. Phys., **28** (2007) 41.

[46] D.J. Eckstrom et al., J. Chem. Phys., **82** (1985) 1792.

[47] A.N. Bunner, PhD thesis, Cornell University, 1967.

[48] M. Ave et al. for the AIRFLY Collaboration, Nucl. Instr. and Meth. in Physics Research A, **597** (2008) 41.

[49] F. Arqueros et al., Astropart. Phys., **26** (2006) 231.

[50] F. Blanco, F. Arqueros, Phys. Lett. A, **345** (2005) 355.

[51] M. Ave et al. for the AIRFLY Collaboration, Nucl. Instr. and Meth. in Physics Research A, **597** (2008) 46.

[52] http://rd11.web.cern.ch/rd11/rkb/ph14pp/node26.html.

[53] F. Nerling, J. Blümer. R. Engel, M. Risse, Astropart. Phys., **24** (2006) 421.

[54] M. Mostafa for the Pierre Auger Collaboration, arXiv:astro−ph/0608005v1 (2006).

[55] T. Hara et al., Acta Physica Academiae Hungaricae. 3 (29 Suppl.) (1970) 369.

[56] R.M. Baltrusaitis et al., Nucl. Instr. and Meth. A, **240** (1985) 410; R.M. Baltrusaitis et al., Nucl. Instr. and Meth. A, **264** (1988) 87.

[57] T. Abu-Zayyad et al., Nucl. Instr. and Meth. A, **450** (2000) 253.

[58] M. Fukushima et al., Proceedings of the 30^{th} International Cosmic Ray Conference, Merida, Mexico, (2007) 955.

[59] K. Kasahara, arXiv:astro-ph/0511177v2 (2005).

[60] Y. Aita et al., Proceedings of the 28^{th} International Cosmic Ray Conference, Tsukuba, Japan, **2** (2003) 1061.

[61] F. Kajino for the JEM-EUSO Collaboration, Nucl. Instr. and Meth. A, **623** (2010) 422.

[62] J. Jelley, et al., Nature, **205** (1965) 327.

[63] M. Aglietta et. al. for the Pierre Auger Collaboration, Proceedings of the 29^{th} International Cosmic Ray Conference, Pune, India, **00** (2005) 101.

[64] X. Bertou et. al for the Pierre Auger Collaboration, Nucl. Instr. and Meth. in Phys. Res. A, **523** (2004) 50.

[65] The Pierre Auger Collaboration, Nucl. Instr. and Meth. A, **613** (2010) 29.

[66] A. Etchegoyen, et al., Nucl. Instr. and Meth. A, **545** (2005) 602.

[67] Claudio Di Giulio for the Pierre Auger Collaboration, Proceedings of the 31^{st} International Cosmic Ray Conference, Lodz (2009) 142.

[68] The Pierre Auger Collaboration, Nucl. Instr. and Methods in Physics Research A, **620** (2010) 227.

[69] Schott Glaswerke, Mainz, Germany, http://www.schott.com.

[70] PHOTONIS, http://www.photonis.com.

[71] G. Navarra et. al., Nucl. Inst. Meth. A, **518** (2004) 207.

[72] G. Medina Tanco et al., Proceedings of the 30^{th} International Cosmic Ray Confe-

rence, Merida, Mexico, **5** (2007) 1101.

[73] H. O. Klages et al., Proceedings of the 30^{th} International Cosmic Ray Conference, Merida, Mexico, **5** (2007) 849.

[74] A. Etchegoyen et al., Proceedings of the 30^{th} International Cosmic Ray Conference, Merida, Mexico, **5** (2007) 1191.

[75] Johannes Blumer for the Pierre Auger Collaboration, New J. Phys., Vol. 12, No. 3 (2010)

[76] The Pierre Auger Collaboration, Physics Letters B, **685** (2010) 239.

[77] J. Abraham et al. for the Pierre Auger Collaboration, Physical Review Letters, **101** (2008) 061101.

[78] F. Schussler for the Pierre Auger Collaboration, Proceedings of the 31^{st} International Cosmic Ray Conference, Lodz (2009) 114.

[79] F. Salamida for the Pierre Auger Collaboration, Proceedings of the 31^{st} International Cosmic Ray Conference, Lodz (2009) 109.

[80] J. Rautenberg for the Pierre Auger Collaboration, Proceedings of the 31^{st} International Cosmic Ray Conference, Lodz (2009) 235.

[81] L. Valore for the Pierre Auger Collaboration, Proceedings of the 31^{st} International Cosmic Ray Conference, Lodz (2009) 87.

[82] R. U. Abbasi et al. Physical Review Letters, 100:101101, (2008).

[83] R. U. Abbasi et al. Physical Review Letters, B **619** (2005) 271.

[84] The Pierre Auger Collaboration, Physical Review Letters, **104** (2010) 091101.

[85] The Pierre Auger Collaboration, Phys. Rev. D, **79** (2009) 102001.

[86] The Pierre Auger Collaboration, Astropart. Phys., **31** (2009) 399.

[87] D. Allard et al., J. Cosmol. Astropart. Phys., **9** (2006) 5.

[88] R. J. Protheroe, Nucl. Phys. B, Proc. Suppl. **77** (1999) 465.

[89] R. Engel, D. Seckel, and T. Stanev, Phys. Rev. D, **64** (2001) 093010.

[90] L. A. Anchordoqui et al., Phys. Rev. D, **76** (2007) 123008.

[91] K. Shinozaki et al., Astrophys. J., **571** (2002) L117.

[92] M. Risse et al., Phys. Rev. Lett., **95** (2005) 171102.

[93] G. Rubtsov et al., Phys. Rev. D, **73** (2006); (astro-ph/0601449).

[94] A. V. Glushkov et al., JETP Lett., **85** (2007) 163; (astro-ph/0701245).

[95] M. Ave, J. A. Hinton, R. A. Vazquez, A. A. Watson, E. Zas, Phys. Rev. Lett., **85** (2000) 2244.

[96] M. Ave, J. A. Hinton, R. A. Vazquez, A. A. Watson, E. Zas, Phys. Rev. D, **65** (2002) 063007.

[97] J. Abraham et al. for the Pierre Auger Collaboration, Astropart. Phys., **29** (2008) 243; (arXiv:0712.1147 astro-ph).

[98] The Pierre Auger Collaboration, arXiv:0903.1127v2.

[99] G. Gelmini, O. Kalashev, and D. V. Semikoz, JCAP 11 (2007); (arXiv:0706.2181 astro-ph).

[100] G. Gelmini, O. Kalashev, and D. V. Semikoz, astro-ph/0506128.

[101] J. Ellis, V. E. Mayes, and D. V. Nanopoulos, Phys. Rev. D, **74** (2006) 115003; (astro-ph/0512303).

[102] M. Risse and P. Homola, Mod. Phys. Lett. A, **22** (2007) 749, (astro-ph/0702632).

[103] C. Bonifazi for the Pierre Auger Collaboration, Nucl. Phys B. (Proc. Suppl.), **190** (2000) 20.

[104] J. D. Hague for the Pierre Auger Collaboration, Proceedings of the 31^{st} International Cosmic Ray Conference, Lodz (2009) 143.

[105] AIRFLY Collaboration, 5^{th} Fluorescence Workshop, Madrid (2007); astro-ph arXiv:0711.4583.

[106] Martin Will, Private Communication.

[107] B. Keilhauer et al., Proceedings of the 29^{th} International Cosmic Ray Conference, vol. 7, Pune, India (2005) 123; arXiv:astro-ph/0507275.

[108] Graw Radiosondes GmbH and Co. KG, www.graw.de.

[109] Inc. Campbell Scientific. www.campbellsci.com.

[110] M. Winnick et al., *Status of the cloud camera*, Pierre Auger Collaboration Meeting, November 2007.

[111] M. Winnick, PhD Thesis June 2010, Auger Project Note GAP−2010−111.

[112] R. Mussa, G. Sequeiros, A. Tonachini, Auger Technical Note GAP−2007−038.

[113] L. Valore, Auger Technical Note GAP-2008-020.

[114] A. R. Biral, Auger Technical Note GAP-2003-087.

[115] B. Fick et al., Auger Technical Note GAP−2004−003.

[116] B. Keilhauer, Auger Technical Note GAP−2003−009.

[117] B. Keilhauer, J. Blumer, R. Engel, H.O. Klages, 5^{th} Fluorescence Workshop, Madrid, (2007).

[118] M. Will, Auger Technical Note GAP−2009−081.

[119] S. Argiro, S.L.C. Barroso, J. Gonzalez, L. Nellen, T. Paul, T.A. Porter, L. Prado, Jr., M. Roth, R. Ulrich, D. Veberic, Nucl. Instrum. Meth. **A580** (2007) 1485, arXiv:0707.1652 [astro-ph].

[120] M. Unger for the Pierre Auger Collaboration, Nucl. Phys. Proc. Suppl. 190 (2009), 240 arXiv:0902.3787; J.A. Bellido for the Pierre Auger Collaboration, Proc. XXth Rencontres de Blois (2008), arXiv:0901.3389.

[121] A. H. Maghrabi, *Ground based measurements of atmospheric infrared radiation from clear and cloudy skies*, (2007), PhD Thesis.

[122] B. Keilhauer, Auger Technical Note GAP−2011−015.

[123] D. Gora et. al., Astropart. Phys., **16** (2001) 129.

[124] D. Gora, Pierre Auger Project Note GAP−2004−034.

[125] D. Gora et al., Astropart. Phys., **24** (2006) 484.

[126] D. R. Longtin, (1988), Air Force Geophysical Laboratory AFGL−TR−88−0112.

[127] The Auger Collaboration, *The Pierre Auger Design Report*, 2nd Edition, (1997).

[128] M.D. Roberts, J. Phys. G, **31** (2005) 1291.

[129] M. Unger for the Pierre Auger Collaboration, astro-ph arXiv:0706.1495v1.

[130] B. R. Dawson, Auger Technical Note GAP−2007−121.

[131] J. Parrisius, Auger Project Note GAP−2009−045.

[132] A. Creusot, D. Vberic, Auger Project Note GAP−2009−070.

[133] B. Dawson, Pierre Auger Project Note GAP−2009−129.

[134] D. Mandat, M. Pech, M. Palatka, L. Nozka, M. Hrabovsky, P. Schovanek, Auger Project Note GAP−2009−164.

[135] K. Louedec, M. Urban, S. Dagoret-Campagne, Auger Project Note GAP−2009−173.

[136] M. Unger, R. Engel, F. Schussler, R. Ulrich, Auger Technical Note GAP−2008−052.

[137] M. Giller and G. Wieczorek, *Influence of the scattered Cherenkov light on the width of shower images in FD*, talk at Nov 2007 Auger Collaboration Meeting.

[138] D. Allard et. al., Auger Technical Note GAP−2006−026.

[139] F. Arqueros et al., Proceedings of the 29^{th} International Cosmic Ray Conference, **00** (2005) 101

[140] P. Facal, P.Privitera, Auger Technical Note GAP−2000−010.

[141] R. Caruso et al., Auger Technical Note, GAP−2003−083.

[142] J. Becker, Untersuchung der optischen Eigenschaften der Fluoreszenzteleskope des Pierre Auger Observatoriums, Diploma Thesis, Universitt Karlsruhe, 2005.

[143] M. Radosz, Untersuchung der Abbildungseigenschaften eines Auger Fluoreszenzteleskopes mit einer knstlichen UV-Lichtquelle, Diploma Thesis, Universitt Karlsruhe, 2005.

[144] C. Di Giulio, P. Facal San Luis, G. Rodriguez, M. Tueros and V. Verzi, Auger Project Note GAP−2008−141.

[145] Valerio Verzi, University of Rome, Private Communication.

[146] D. Heck, J. Knapp, J. N. Capdevielle, G. Schatz, T. Thouw, Report FZKA 6019, Forschungszentrum Karlsruhe, 1998. Available from www-ik.fzk.de/heck/corsika.

[147] M. Risse, D. Heck, Astropart. Phys., **20** (2004) 661.

[148] M. Risse et al., Proceedings of the 24^{th} International Cosmic Ray Conference, Hamburg 2001, p522.

[149] A. M. Hillas, Nucl. Phys. B (Proc. Suppl.) **52** (1997) 29.

[150] M. Kobal, A. Filipcic, D. Zavrtanik for the Pierre Auger Collaboration, in Proceedings of the 26^{th} International Cosmic Ray Conference, Salt Lake City, USA, **1** (1999) 490.

[151] R.M. Sternheimer, M.J. Berger, S.M. Seltzer, Atomic Nucl. Data Tables **30** (1984) 261.

[152] R.M. Sternheimer et al., Phys. Rev. B, **26** (1982) 6067.

[153] K. R. Kase, W.R. Nelson, *Concepts of Radiation Dosimetry*, Pergamon Press, New York, (1979).

[154] K. Shinozaki, Proceedings of Quarks 2006, 14^{th} International Seminar on High Energy Physics, St Petersburg, Russia, 2006, http://quarks.inr.ac.ru/2006/proceedings/.

[155] R. Ulrich, R. Engel, S. Muller, F. Schussler, M. Unger, Proceedings of the 15^{th} International Symposium on Very High Energy Cosmic Ray Interactions, Paris 2008.

[156] H. Allan, Progress in Elementary Particles and Cosmic Ray Physics, **10** (1971) 171.

[157] D. Ardouin, et al., Nucl. Instr. Meth. A, **555** (2005) 148.

[158] D. Ardouin, et al., Astropart. Phys., **26** (2006) 341.

[159] N. Hayashida and T. Kifune, Nucl. Instr. Meth, **173** (1980) 431.

[160] M. Nagano et al., J. Phys G, **10** (1984) 1295.

[161] B. Keilhauer, J. Blumer, R. Engel, H.O. Klages, Astropart. Phys., **25** (2006) 259; astro-ph/0511153 (2005).

[162] R. Engel et al., Phys. Rev. D 64, 093010 (2001); D. Allard et al., JCAP 9, 5 (2006); L. Anchordoqui et al., Phys. Rev. D **76** (2007) 123008.

[163] W.R. Nelson, H. Hirayama, D.W.O. Rogers, Report SLAC 265, Stanford Linear Accelerator Center, 1985.

[164] D. Heck, J. Knapp, report FZKA 6097, Forschungszentrum Karlsruhe, 1998.

[165] L.D. Landau, I. Ya. Pomeranchuk, Dolk. Akad. Nauk. SSSSR 92 (1953) 535 (in Russian); A.B. Migdal, Phys. Rev, **103** (1956) 1811.

[166] D. Heck et al., Proceedings of the 27^{th} International Cosmic Ray Conference, Hamburg (Germany), **1** (2001) 233.

[167] H. Fesefeldt, Report PITHA-85/02, RWTH Aachen, 1985.

[168] D. Kuempel, K. H. Kampert, M. Risse, Astropart. Phys., **30** (2008) 167.

[169] The Pierre Auger Collaboration, Astropart. Phys., **33** (2010) 108.